

NPS-OC-95-002

# NAVAL POSTGRADUATE SCHOOL

## Monterey, California



## THESIS

### ESTIMATION OF BOTTOM SCATTERING STRENGTH FROM MEASURED AND MODELED AN/SQS-53C REVERBERATION LEVELS

by

19960116 049

Gary Alexander Scanlon

June 1995

Thesis Advisors:

James H. Wilson  
Robert H. Bourke

Approved for public release; distribution is unlimited

Prepared for:

Program Executive Office (PMO411)  
Surface Ship ASW Systems  
Washington, D.C. 20362-51004

Naval Undersea Warfare Center Detachment-NL  
Code 3122  
New London, CT. 06320-5594

**NAVAL POSTGRADUATE SCHOOL  
Monterey, California 93943**

Rear Admiral Mercer  
Superintendent

This thesis was prepared in conjunction with research sponsored in part by the Program Executive Office, Surface Ship ASW Systems (PMO411F4) under Program Element Number 0205620N.

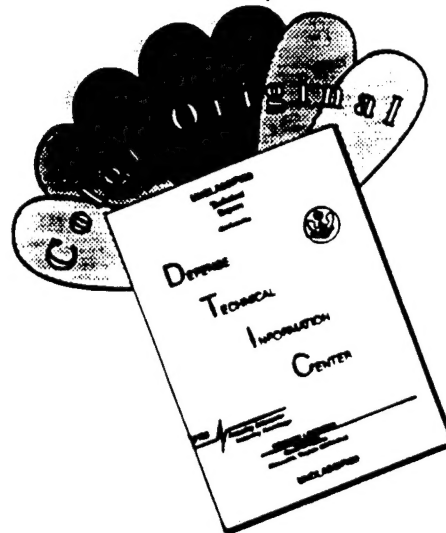
Reproduction of all or part of this report is authorized.

Released by:



P.J. MARTO, Dean of Research

# **DISCLAIMER NOTICE**



**THIS DOCUMENT IS BEST  
QUALITY AVAILABLE. THE COPY  
FURNISHED TO DTIC CONTAINED  
A SIGNIFICANT NUMBER OF  
COLOR PAGES WHICH DO NOT  
REPRODUCE LEGIBLY ON BLACK  
AND WHITE MICROFICHE.**

REPORT DOCUMENTATION PAGE			Form Approved OMB No. 0704-0188
<p>Public reporting burden for this collection of information is estimated to average 1 hour per response, including the time for reviewing instruction, searching existing data sources, gathering and maintaining the data needed, and completing and reviewing the collection of information. Send comments regarding this burden estimate or any other aspect of this collection of information, including suggestions for reducing this burden, to Washington Headquarters Services, Directorate for Information Operations and Reports, 1215 Jefferson Davis Highway, Suite 1204, Arlington, VA 22202-4302, and to the Office of Management and Budget, Paperwork Reduction Project (0704-0188) Washington DC 20503.</p>			
1. AGENCY USE ONLY	2. REPORT DATE June 1995	3. REPORT TYPE AND DATES COVERED Master's Thesis	
4. TITLE AND SUBTITLE  <b>ESTIMATION OF BOTTOM SCATTERING STRENGTH FROM MEASURED AND MODELED AN/SQS-53C REVERBERATION LEVELS</b>			5. FUNDING NUMBERS  PMO411 Reference Number N0002494AFEC4JP
6. AUTHOR  Scanlon, Gary A. in conjunction with Wilson, J. H. and Bourke, R. H.			
7. PERFORMING ORGANIZATION NAME(S) AND ADDRESS(ES) Naval Postgraduate School Monterey CA 93943-5000			8. PERFORMING ORGANIZATION REPORT NUMBER NPS-OC-95-002
9. SPONSORING/MONITORING AGENCY NAME(S) AND ADDRESS(ES)  Program Executive Office, Surface Ship ASW Systems (PMO411) Washington, D.C., 20362-5104			10. SPONSORING/MONITORING AGENCY REPORT NUMBER
11. SUPPLEMENTARY NOTES  The views expressed in this thesis are those of the author and do not reflect the official policy or position of the Department of Defense or the U.S. Government.			
12a. DISTRIBUTION/AVAILABILITY STATEMENT  Approved for public release; distribution is unlimited		12b. DISTRIBUTION CODE	
13. ABSTRACT Hamilton-type geoacoustic models were developed for Area Foxtrot, a NUWC test bed for emerging active sonar systems where the surface sediment type is highly spatially variable. Reverberation levels (RL) were modeled using the FEPE propagation model to augment the GSM propagation model because the bottom loss model in GSM did not estimate transmission loss (TL) accurately in shallow water. FEPE estimates reveal there is over a 15 dB difference between TL for sand and silt-clay sediments in Area Foxtrot. The comparison between modeled RL and measured RL (from a 1991 ASW exercise conducted by NUWC) enabled bottom scattering strength kernels to be developed for Area Foxtrot. Bottom scattering strength was found to be a function of sediment type. Hard sand sediment has a bottom scattering strength which obeys Lambert's law ( $\sin^2(\theta)$ ) while that of silt-clay sediment is consistent with volume scattering ( $\sin(\theta)$ ). The RLs in Area Foxtrot are azimuth-dependent and are a function of TL and bottom scattering strength (and hence bottom sediment type). Sonar beams steered towards the hard sand show higher RLs than for silt-clay.			
14. SUBJECT TERMS  Acoustics, Bottom Scattering Strength, Finite Element Parabolic Equation, FEPE, Generic Sonar Model, GSM, Geology, Geophysics, Reverberation, Transmission Loss, AN/SQS-53C Active Sonar Performance		15. NUMBER OF PAGES  204	
16. PRICE CODE			
17. SECURITY CLASSIFICATION OF REPORT Unclassified	18. SECURITY CLASSIFICATION OF THIS PAGE Unclassified	19. SECURITY CLASSIFICATION OF ABSTRACT Unclassified	20. LIMITATION OF ABSTRACT UL



Approved for public release; distribution is unlimited

**ESTIMATION OF BOTTOM BACKSCATTERING STRENGTH FROM  
MEASURED AND MODELED AN/SQS-53C  
REVERBERATION LEVELS**

Gary Alexander Scanlon  
Lieutenant, United States Navy  
B.S., Wilkes College, 1982  
M.A., State University of New York - Binghamton, 1986

Submitted in partial fulfillment of the  
requirements for the degree of

**MASTER OF SCIENCE IN METEOROLOGY AND  
PHYSICAL OCEANOGRAPHY**

from the

**NAVAL POSTGRADUATE SCHOOL**

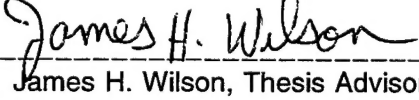
June, 1995

\*Original contains color  
plates: All DTIC reproductions will be in black and white\*

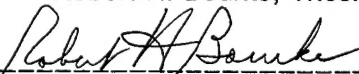
Author:

  
Gary A. Scanlon

Approved by:

  
James H. Wilson, Thesis Advisor

  
Robert H. Bourke, Thesis Advisor

  
Robert H. Bourke, Chairman  
Oceanography Department

Accesion For	
NTIS CRA&I	<input checked="" type="checkbox"/>
DTIC TAB	<input type="checkbox"/>
Unannounced	<input type="checkbox"/>
Justification _____	
By _____	
Distribution / _____	
Availability Codes	
Dist	Avail and / or Special
A-1	



## **ABSTRACT**

Hamilton-type geoacoustic models were developed for Area Foxtrot, a NUWC test bed for emerging active sonar systems where the surface sediment type is highly spatially variable.

Reverberation levels (RL) were modeled using the FEPE propagation model to augment the GSM propagation model because the bottom loss model in GSM did not estimate transmission loss (TL) accurately in shallow water. FEPE estimates reveal there is over a 15 dB difference between TL for sand and that for silt-clay sediments in Area Foxtrot. The comparison between modeled RL and measured RL (from a 1991 ASW exercise conducted by NUWC) enabled bottom scattering strength kernels to be developed for Area Foxtrot. Bottom scattering strength was found to be a function of sediment type. Hard sand sediment has a bottom scattering strength which obeys Lambert's law ( $\sin^2(\theta)$ ) while that of silt-clay sediment is consistent with volume scattering ( $\sin(\theta)$ ). The RLs in Area Foxtrot are azimuth-dependent and are a function of TL and bottom scattering strength (and hence bottom sediment type). Sonar beams steered towards the hard sand show higher RLs than for silt-clay.



## TABLE OF CONTENTS

I.	INTRODUCTION .....	1
	A. REVERBERATION DATA BASE .....	4
	B. OBJECTIVES OF THIS THESIS .....	5
II.	THEORY AND BACKGROUND OF HAMILTON-TYPE GEOACOUSTIC MODELS .....	7
III.	PRELIMINARY GEOACOUSTIC MODEL DEVELOPED BY NPS AND ENVIRONMENTAL SUMMARY .....	25
	A. BACKGROUND OF NUWC'S CURRENT GEOACOUSTIC / BOTTOM LOSS MODEL .....	26
	B. RECOMMENDED CHANGES TO NUWC'S CURRENT GEOACOUSTIC MODEL .....	30
	C. CONSTRUCTION OF A HAMILTON GEOACOUSTIC MODEL FOR AREA FOXTROT .....	33
	D. LAMBERT'S LAW OF BOTTOM BACKSCATTERING .....	46
IV.	TRANSMISSION LOSS MODEL SENSITIVITY to INPUT GEOACOUSTIC PARAMETERS .....	51
	A. THE GSM/MPE PROPAGATION MODEL .....	51
	B. THE FEPE PROPAGATION MODEL .....	55
	C. COMPARISON OF GSM AND FEPE TL CALCULATIONS FOR THE SAME GEOACOUSTIC MODEL .....	58
V.	BOTTOM BACKSCATTER .....	63
	A. THE SAIC METHOD OF ANALYSIS TO DETERMINE BOTTOM SCATTERING STRENGTH (AND THE DOMINANT BOTTOM SCATTERING MECHANISM) .....	63

B. DETERMINATION OF SEAFLOOR SCATTERING STRENGTH AND BACKSCATTER .....	64
C. USING THE SAIC ANALYSIS METHOD TO DETERMINE BOTTOM SCATTERING STRENGTH (S <sub>b</sub> ) FROM AREA FOXTROT DATA .....	71
D. CURVE FITTING OF BOTTOM SCATTERING STRENGTH ..	87
VI. CONCLUSIONS .....	91
VII. RECOMMENDATIONS .....	97
A. RECOMMENDATIONS REGARDING AREA FOXTROT .....	97
B. RECOMMENDATION REGARDING BOTTOM SCATTERING STRENGTH .....	98
C. RECOMMENDATION REGARDING GSM .....	99
D. RECOMMENDATION REGARDING THE TACTICAL APPLICATION OF THIS THESIS .....	99
APPENDIX. FIGURES .....	101
REFERENCES .....	175
INITIAL DISTRIBUTION LIST .....	189

## **ACKNOWLEDGEMENTS**

I would like to acknowledge the financial support of the Program Executive Office, Surface Ship ASW Systems (PMO411).

This work was conducted under PMO411 reference number N0002494AFEC4JP. I thank Capt. G. Nifontoff (PMO411) for his insight in funding research at NPS.

I also thank Mr. Ed. Jensen, at the Naval Undersea Warfare Center (NUWC), New London, for his kind assistance and establishing cooperation between NUWC and NPS for this research effort. Thanks also to Dr. Judith Bishop and Mr. Steve Trudell of NUWC for supplying and maintaining the GSM program used in this study and to Mr. M. Mazzi for ensuring the smooth transfer of data from NUWC to NPS.

I thank Linda, Jackie, and CDR. Lage in the Air-Sea Curricular Office and Hoda and Sue in the Oceanography Department Office for their valued support.

And special thanks my thesis advisors Prof. Wilson and Prof. Bourke for their guidance and instruction in conducting this investigation.

## I. INTRODUCTION

The submarine threat to Naval forces has moved from deep water environments to shallow water. Understanding and exploiting the unique acoustic characteristics of coastal waters is paramount to our national security and the success of Naval forces operating in shallow water.

Shallow water environments are the most difficult environments to model geoacoustically because of the variability of the bottom sediment type. Not only are the surface sediments laterally inhomogeneous, but they are vertically inhomogeneous as well. A detailed geologic study of an area is necessary before a good geoacoustic model can be developed. Geoacoustic models based on sparse geologic data are of little value. The variability of the ocean bottom must be recognized and incorporated into the Navy's performance prediction models to accurately estimate transmission loss and reverberation levels. Failure to understand the variability of ocean bottom sediments means inaccuracy in modeling acoustic propagation in shallow water regimes. This in turn means

inaccuracy in modeling sonar performance locally and in potential conflict areas.

"The littoral (coastal) region is frequently characterized by confined and congested water and air space occupied by friends, adversaries, and neutrals--making identification profoundly difficult. This environment poses varying technical and tactical challenges to naval forces. It is an area where our adversaries can concentrate and layer their defenses. In an era when arms proliferation means some Third World countries possess sophisticated weaponry, there is a wide range of potential challenges. For example, an adversary's submarines operating in shallow waters poses a particular challenge to naval forces...Mastery of the littoral should not be presumed. It does not derive directly from command of the high seas. It is an objective which requires our focused skills and resources." ----excerpts from the Navy and Marine Corps White Paper, ...**From the Sea** (O'Keefe et al.,1992).

Many potential advisarial nations are rapidly acquiring /expanding their submarine fleets. Russia has agreed to sell to Iran three (possibly four) Kilo-class diesel submarines, the first of which was formally commissioned as the Taregh (named after a famous Muslim warrior) in late 1992. Recently China has purchased a Russian Kilo-class submarine. Since 1985, other countries which have imported Russian Kilo-class submarines include Algeria (two),

Poland (one), Romania (one), and India (eight). This world-wide proliferation of stealthy undersea platforms truly supports the need for continued research in the field of shallow water geoacoustics.

Much work has been completed in geoacoustics as it relates to USW (undersea warfare) in deep water. In contrast, much remains to be done in shallow water environments especially when using the active sonar systems needed to prosecute the silent diesel submarine. Because of the likelihood of multiple bottom interactions from active sonars, operations in shallow water forces us to better understand the influence that the ocean bottom exerts on acoustic propagation. If the geoacoustics and geophysics of the bottom are not modeled correctly, each bottom interaction will "amplify" the modeling error throughout the path of the acoustic signal. Even small errors in modeling the bottom can translate into signal excess mis-calculations of many decibels in magnitude. Better detailed geoacoustic models are required to completely understand an acoustic environment and to quantify and qualify the geophysics involved to accurately predict the performance of current and emerging sonars in shallow water.

## A. REVERBERATION DATA BASE

Reverberation data used in this study are part of a data base collected during a series of shallow water ASW tests conducted 3-13 September 1991 (Fisch et al., 1991) and were supplied by the Naval Undersea Warfare Center (NUWC), New London, CT. The data supplied to the Naval Postgraduate School (NPS) consisted of 88 pings of measured reverberation levels. Half of the pings were continuous wave (CW), 500 millisecond duration waveforms and the other half were coded pulse (CP), 500 millisecond duration waveforms. Each ping consisted of 24 beams with a total beamwidth of 120 degrees. The depression angle of the sonar was 3 degrees. This study only used the CW (500) waveform data.

The reverberation data were collected using the AN/SQS-53C sonar onboard USS STUMP (DD-978) in accordance with an established test plan (NUSC, 1991). The data used in this study were collected on 7 September 1991 during Run 18 of the ASW tests. Run 18 was conducted in 64 m of water with a negative (downward) refracting sound speed profile. For a complete environmental report of the conditions during the ASW tests see Gallagher (1991).

The 1991 ASW tests and reverberation data collection efforts were conducted in Area Foxtrot, NUWC's test bed for emerging sonars. Area Foxtrot is an area on the continental shelf of the U.S. eastern seaboard and lies approximately 50 nmi south of Montauk Point, Long Island, NY.

## **B. OBJECTIVES OF THIS THESIS**

The objectives of this thesis are:

1. Examine the current geoacoustic model for Area Foxtrot and, if necessary, develop a new Hamilton-type geoacoustic model for the area.
2. Use the Generic Sonar Model Multi-Path Expansion System propagation model, currently used by NUWC for transmission loss (TL) and reverberation level (RL) modeling, and evaluate the model's usefulness in a shallow water environment.
3. Compare measured RL and modeled RL to develop a bottom scattering strength kernel for Area Foxtrot.

This page intentionally left blank.

## **II. THEORY AND BACKGROUND OF HAMILTON-TYPE GEOACOUSTIC MODELS**

A geoacoustic model of the seafloor defines the thickness and geophysical properties of the unconsolidated sediment and rock strata of the ocean bottom. Geoacoustic models are used in modeling the interaction of acoustic energy with the sea bottom. Parameters of a geoacoustic model consist of measured, extrapolated, and calculated values of those geophysical properties important in estimating the propagation of acoustic energy (sound) when it interacts with the seafloor. Geoacoustic models guide theoretical underwater acoustic studies, help reconcile acoustic experiments at sea with theory, and aid in predicting the effects of the seafloor on acoustic energy (Hamilton, 1987). The general subject of geoacoustic modeling has been summarized by Hamilton (1980).

Data used to construct a geoacoustic model include bathymetric charts, echo-sounding records e.g., side-scan sonars, analyses from seismic reflection and refraction records, acoustic

reflection records, geologic data derived from sediment or rock grabs and cores, and water mass sound speed data. A wealth of such information can be found in the geologic and geophysical literature and through today's Internet resources.

A geoacoustic model should contain at least six geoacoustic properties for each sediment or rock layer to be of value to a geophysicist or acoustician. These properties are 1) the thickness of the layer and locations of any reflectors within the layer, 2) the compressional wave speed at the top of the layer and the gradient within the layer, 3) the compressional wave attenuation at the top of the layer and the gradient within the layer, 4) the shear wave speed at the top of the layer and the gradient within the layer, 5) the shear wave attenuation at the top of the layer and the gradient within the layer, and 6) the density at the top of the layer and the gradient within the layer. Shear wave speed and shear attenuation may or may not be required based on the acoustic model used and relative magnitudes of compressional and shear wave speeds. Geoacoustic properties must be quantified as accurately as possible down to the depth of the acoustic basement.

It is rare that all six properties have been measured for any given location. Therefore, the missing properties must be estimated by extrapolation or calculation from similar sediments in the same type of depositional environment but often at distant locations.

Geoacoustic modeling in shallow water environments poses some unique challenges and difficult problems. Paramount among these are the vertical and horizontal variability of sediment and rock types and the consequent variability of geoacoustic properties. Surface sediment type charts based on a few bottom samples are insufficient to adequately model a geoacoustic environment because the uppermost sediment layer may be relatively thin and show lateral pinch-outs or feathering to expose underlying strata. Many seafloor areas were originally thought to be spatially homogeneous, and thus, acoustically benign based on some wide-spread surface sediment data. Seismic reflection profiling with sufficient resolution would enable researchers to chart the lateral extent and thickness of reflectors. Note that most, if not all, environments once considered acoustically benign are actually quite spatially variable.

The bottom composition in shallow water environments can be highly spatially variable within one general local and throughout the shallow water regime. In some areas the bottom sediment may be sand, silt, clay, shell fragments, or biogenic ooze, or some combination of these. In other areas the bottom may be exposed rock. This rock may be sedimentary, igneous (intrusive or extrusive), and of course, metamorphic. Some rocky seafloors are so rough due to lava flows, large-scale faults or small-scale fractures, that acoustic energy is scattered, reflected, refracted, and diffracted to such a great extent that it is not possible to construct a useful geoacoustic model. In this case, the bottom reflectivity or bottom loss at the frequency of interest must be measured in situ.

The geoacoustic models developed in this study were constructed using a method put forth by Hamilton (1980) and Hamilton and Bachman (1982). This method uses a series of regression equations derived from measurements of sediment and rock geophysical parameters as they relate to the geoacoustic properties (sound speed, attenuation, etc.). The geophysical parameters include porosity, grain size, density, bulk modulus, and

others. Hamilton (1987) showed that the geophysical properties of a sediment type obtained at a site from one ocean are about the same as those for a sediment in another ocean given that the two sediments were deposited in the same environment and under similar depositional conditions. These regression equations can therefore be used world-wide as long as they are applied to the appropriate geophysical environment.

Note that the geoacoustician must have a good understanding of the geologic principles governing depositional environments and temporal evolution of environments in order to temper Hamilton's equations and apply them appropriately. These equations should not be used without an understanding of the geological sciences and geologic history of a study area. For instance, the Barents Sea is a shallow arctic sea environment. But direct application of Hamilton's equations for a shallow water environment to the Barents Sea would not be appropriate considering the geologic history of the area. The Barents Sea was recently (geologically speaking) scoured clean of its bottom unconsolidated sediments by glaciation. The enormous mass of the glaciers produced a great deal

of overburden pressure on the underlying strata increasing the densities of the strata more than would have been expected in the shallow water environment. Geology must be considered in the construction of geoacoustic models.

Acoustic wave speeds (compressional and shear) in sediments are functions of the elastic properties of the two-phase sediment mass (pore water and mineral structure). Hamilton (1971, 1972) concluded that the elastic properties of water-saturated sediments could be expressed through the Hookean elastic equations unless attenuation is considered. In this latter case, linear viscoelastic models and equations are recommended. Sediment porosity and grain size effect sound speeds only through their effect on the elastic properties of the sediment.

The compressional wave speed is inversely proportional to porosity and is directly proportional to density. The compressional wave speeds in a low porosity, coarse-grained sand can exceed 1800 m/s whereas in a high porosity silt-clay it can be less than 1500 m/s (sometimes less than the sound speed in the bottom water) (Figure 1). The relationship between compressional wave speed and

porosity has received much attention because porosity is an easily-measured sediment property and the relationship usually permits a reasonable prediction of sediment acoustic wave speeds (Hamilton, 1987). The high correlation between porosity and compressional wave speed occurs because it is the volume of interstitial pore water that largely determines the compressional wave speed in the sediment. This is a result of the relatively high compressibility of water compared to that of the composite mineral grains of the sediment. The net effect of the varying volumes of the water and mineral grains (and hence density) results in many continental terrace silt-clays and most abyssal hill and plain high porosity sediments having compressional wave speeds less than that of the overlying bottom water (Hamilton, 1987). Note that from in situ measurements, compressional wave speeds in the higher porosity sediments are usually no more than three percent less than in the bottom sea water at the same temperature and pressure.

The laboratory-derived compressional wave speed ratios between the sediment and water, summarized by Hamilton (1980) and Hamilton and Bachman (1982), can be used to predict the in situ

sediment surface compressional wave speed because the ratio is the same in the laboratory or at any bottom depth in the ocean.

However, these laboratory values must be corrected for depth to the seafloor. To make the correction, the laboratory compressional wave speed ratio is multiplied by the bottom water sound speed. This has the same effect as making full temperature and pressure corrections to the laboratory measurements.

The relationship between sediment density and compressional sound speed is similar to that for porosity because of the linear relationship between density and porosity.

The sediment mean grain size from all types of bottom environments and the percent clay-sized grains from deep sea environments were determined in early works to be important indices to compressional wave speeds (Hamilton, 1970; Schreiber, 1968; Horn et al., 1968; Sutton et al., 1957; Hamilton et al., 1956). Hamilton and Bachman (1982) verified these earlier studies and showed that the acoustic wave speed is directly proportional to grain size. The relationship between grain size and acoustic wave speed (Figure 2) is especially important because grain size analyses

can be made from dried sediment samples for which density (in situ), porosity, and sound speed can not be made. Grain size can also be measured from simple sediment grabs or cores. Additionally, much data exist on grain size in the geologic literature which can be used as indices to acoustic properties.

Grain size affects the acoustic wave speed through the properties of density and porosity. However, other factors such as grain shape, mineralogy and the presence of microcrystalline fractures may influence the structural rigidity and therefore the acoustic wave speed of the sediment in minor ways.

The calculation of compressional wave speed can be performed using the porosity (or density) or grain size of a sediment. Hamilton (1980) and Hamilton and Bachman (1982) have compiled a series of regression equations developed from in situ and laboratory measurements which relate these properties to compressional wave speed. This study used the grain size regression equations to calculate the compressional wave speed at the surface of the sediment layer since these data were most available. Verification of the calculated compressional sound speeds was made using

available sediment density data. The sediment data were provided by the University of Rhode Island (Shoukimas, 1995).

It is important to note that Hamilton's (1980) and Hamilton and Bachman's (1982) regression equations were forced to fit through the acoustic wave speed at the sediment surface. Acoustic wave speed equations derived from sonobuoy data are based on the mid-point interval velocity from the first layer of sediment. No information is usually available from sonobuoy data for sound speed at or near the surface of the layer. In this case, the intercepts of regression equations for the top of the sediment layer and the sound speed gradient from the surface are apt to be statistical artifacts (Hamilton, 1987). A specific example is found in the vast amount of published equations from Lamont-Doherty sources. These equations are mostly presented as linear equations and the intercepts at the seafloor are usually statistical artifacts. The equations usually can not be used as presented to calculate instantaneous layer acoustic wave speeds, but must be re-computed with realistic seafloor acoustic wave speeds. This problem is documented by Lamont-Doherty scientists (Houtz, 1974; Houtz et al., 1968) who designed

their equations for primarily computing true sediment and rock layer thicknesses.

Extrapolation of the compressional wave speed at the surface of the sediment to any depth within the layer is also accomplished with regression equations provided by Hamilton (1979, 1985). He used laboratory measurements of the Shell Development Company to compute acoustic wave speed-depth functions in sand sediments. Hamilton found that acoustic wave speed gradients in sands could be very high relative to that for silt-clays. For example, sands could have acoustic wave speed gradients twenty times that for silt-clays in the uppermost 1 - 3 m of the sediment. However, the acoustic wave speed gradient for silt-clay is variable and is directly related to the sedimentation rate and diagenesis of the sediment (Hamilton, 1987). Diagenesis refers to the process involving physical and chemical changes in sediment after deposition that converts it to consolidated rock. For silt-clays, minimum acoustic wave speed gradients are expected in and near areas of the continental terrace where the deposition rate is rapid (Hamilton et al., 1974; Houtz, 1974; Hamilton et al., 1977; Houtz, 1977; Houtz, 1978; Hamilton,

1979; Houtz, 1980; Bachman et al., 1983). Here again geology and geologic history of a study area is required to accurately estimate acoustic wave speed gradients in sediments. Note that the greatest range in sediment acoustic wave speeds is in continental terrace (and hence shallow water) environments.

Once the compressional wave speed has been determined throughout the depth of the entire sediment layer, the compressional attenuation for the layer must be determined. When acoustic energy is refracted through a sediment layer or reflected from impedance contrasts from within a sediment or rock layer, some energy is returned back into the water column. The amount of returned energy is a function of the distance the energy has traveled through the layer and the attenuation of acoustic energy within the layer. Therefore, the compressional wave attenuation at the surface of the layer and the attenuation gradient within the layer are required parameters of a geoacoustic model.

Hamilton (1972, 1987) determined the compressional wave attenuation in sediments as a function of acoustic frequency. It is important to differentiate between intrinsic attenuation and

effective attenuation. Intrinsic attenuation is the loss of acoustic energy through conversion to heat and reduction by friction between adjacent sediment grains. Intrinsic attenuation is the type usually measured in the laboratory. Effective attenuation includes intrinsic attenuation plus attenuation due to gas bubbles, animal burrows, cobbles and large stones, and large shell fragments in the sediment. Other important energy loss mechanisms considered part of effective attenuation include 1) losses at reflectors and refractors including conversion between body wave types (compressional to shear) and conversion of body waves to interface or surface waves, 2) diffraction and scatter due to reflector roughness and curvature, 3) scattering from inhomogeneities within the strata, and 4) apparent loss due to inter-bed multiples which add destructively (Schoenberger et al., 1974, 1975; Scanlon 1985). The total of all energy loss mechanisms (excluding spreading loss) is called 'effective attenuation'. It is effective attenuation which the geoacoustician must use to fully describe the energy loss within a sediment or rock layer. Hamilton (1972, 1987) provides measured attenuation data for sediments from various depositional

environments. Note that Hamilton's measured data include effective attenuation (of which intrinsic attenuation is a part).

Sediment type and its physical properties greatly effect the degree of attenuation in a layer. Sands can attenuate acoustic energy more than ten times that of silt-clays (Figure 3). It is therefore difficult to predict attenuation in a sediment layer without a detailed knowledge of the sediment composition at the surface and with depth. Although the compressional attenuation for sand sediments is greater than that for silt-clay sediments, per unit distance traveled, the overall total attenuation for a sand layer is generally much less than that for silt-clay layers because less total distance is traveled by acoustic energy in sand. This is due to the greater compressional wave speed gradient for sand than for silt-clay. Sand is therefore a more efficient refractor of acoustic energy and returns acoustic energy back to the water column with less internal travel distance than for silt-clay.

A compilation of attenuation data by Hamilton (1972) and Hamilton and Bachman (1982) suggest that attenuation is related to frequency through a constant as in the equation

$$\alpha_p = k_p f \quad (1)$$

where  $\alpha_p$  is the compressional wave attenuation in dB/m

$k_p$  is an attenuation constant (dB/m-kHz)

$f$  is the acoustic frequency (kHz)

If attenuation is dependent on the first power of frequency as in

Equation 1, the constant  $k_p$  must vary with sediment or rock type and

be a function of porosity and grain size. Given either porosity or

grain size, an estimate of the compressional wave attenuation can

be found using the figures and equations provided by Hamilton

(1972). Hamilton (1987) gives compressional wave attenuation

estimates for finer-grained, higher porosity sediments than those in

Hamilton (1972).

Extrapolating the compressional wave attenuation from the sediment surface to deeper depths in the sediment layer is perhaps the most difficult aspect of geoacoustic modeling. Silt-clay

sediments (fine-grained) show an increase in attenuation with depth down to about 500 m after which the attenuation decreases with increased depth (Figure 3). Attenuation values for silt-clays can vary with depth from very low attenuation values (Mitchell and Focke, 1980; Frisk et al., 1981, 1986) to much higher values (Neprochnov, 1971; Jacobson et al., 1981, 1984) which are associated with clay-sands and shales. It is likely that lithification of the silt-clays into shale is responsible for the increased attenuation values.

The differences in attenuation with depth from the sources above are probably due to differences in sediment composition, consolidation and lithification, diagenesis, and stratigraphy. These are many of the same factors which cause variations in sound speed.

For sands, the attenuation changes with depth are a bit more predictable. Sands show a decrease in attenuation with increasing depth at all depths. Hamilton (1976, 1987) suggested that attenuation in sands decreases with about -1/6 the power of the overburden pressure. He further suggested that to predict the value of attenuation in sand, one selects a value of  $k_p$  (see Equation 1) at

the surface and then decrease this value at a rate of  $(\text{depth})^{-1/6}$ . A constant attenuation with depth certainly can not be assumed (Mitchell and Focke, 1983).

As with sound speeds, attenuation values in each sediment and rock layer is apt to be unique. The best that can be done for prediction of effective attenuation and its gradient is to gather data from similar sediment types and geomorphic areas, examine the data statistically, and relate this information between study areas. No theory or theoretical approach (e.g., Biot-Stoll) can be used to accurately compute the effective attenuation with depth because of the variability of energy loss mechanisms beneath the surface.

Currently, the geoacoustician can begin with an estimate of attenuation at the sediment surface and then vary the attenuation value with depth according to an estimate of the amount of sand and silt-clay in the geologic section. For guidance, the data of Hamilton (1976) can be followed if there are many sand-silt layers. If much less (or no) amounts of sand-silt are expected, the data of Mitchell and Focke (1980) can be used.

Hamilton (1987) agrees with Stoll (1983, 1985) that it is not possible to compute, with any theory, the effective attenuation as a function of depth in thick strata. Theories can relate frequency and burial depth of sediments to intrinsic attenuation but not to effective attenuation.

### **III. PRELIMINARY GEOACOUSTIC MODEL DEVELOPED BY NPS AND ENVIRONMENTAL SUMMARY**

NUWC's test bed for emerging sonar systems is Area Foxtrot.

NUWC considers Area Foxtrot "significant in that it has been shown to have bottom composition and seasonal sound speed characteristics similar to several potential regional conflict areas" (Christian and Capizzano, 1994). For this reason the historically accepted geoacoustic model for Area Foxtrot (Cole et al., 1994) was examined by NPS to seek areas of possible model improvement. This current geoacoustic model for Area Foxtrot (discussed below) has been used for both past and recent acoustic studies. An improved geoacoustic model developed in this study is based on Hamilton's (1970, 1971, 1972, 1976, 1979, 1980, 1985, 1987) and Hamilton and Bachman's (1982) geoacoustic modeling techniques that are now well-established. These models will incorporate Hamilton's geoacoustic parameters derived from a variety of geoacoustic and geologic data.

## **A. BACKGROUND OF NUWC'S CURRENT GEOACOUSTIC / BOTTOM LOSS MODEL**

In May 1965 TL measurements at 3.5 kHz were made in Area Foxtrot by the Naval Underwater Sound Laboratory (Fisch et al., 1992). Analyses at that time indicated that the measured bottom loss was 1.3 dB per bounce at a grazing angle of 11 degrees. An early ray-tracing program was used to estimate the spreading loss, and with questionable assumptions made about volume attenuation, a bottom loss of 1.3 dB per bounce was determined. This value was found to be in good agreement with a bottom loss value extracted from a geoacoustic model which was based on sediment core information from the TL measurement site (Cole et al., 1994). The calculated bottom loss curve (Cole et al., 1994) is based on a half-space mathematical model which includes attenuation. It used a sediment density (from core data) of 2.0 g/cm<sup>3</sup> (Cole, 1956) and a depth-independent compressional wave speed of 1554 m/s using the dispersion method (Barakos, 1962). These values are in stark disagreement with the vast number of geoacoustic measurements made by Hamilton (1976, 1979, 1980). The bottom attenuation,

inferred from the above measurements, was 0.45 dB/ft. Assuming a linear dependence of attenuation with frequency, this corresponds to an attenuation parameter ( $k_p$ ) of 0.422 dB/m-kHz. Table 1 lists the geoacoustic parameters used in the model. The sediment compressional wave speed based on the above values (Cole et al., 1994) is plotted in Figure 4 which also incorporates the water sound speed profile measured for Run 18. The calculated bottom loss curve is frequency independent since the half-space geoacoustic model used a constant attenuation coefficient.

A bottom loss curve, calculated from the geoacoustic model (see Figure 1 of Cole et al., 1994), was used as an input to the GSM model for active sonar performance predictions by NUWC researchers (Cole et al., 1994). That study assumed a Lambert's law of diffuse backscattering at the ocean bottom. The value for the constant "k" used to determine the bottom backscatter strength at 3.5 kHz was derived from a 1965 Area Foxtrot measurement study to be -19.4 dB. The k variable represents the quantity  $10 \log \mu$  in the Lambert's Law relationship,

$$S_b = 10 \log \mu + 10 \log \sin^2 \theta \quad (2)$$

where  $S_b$  is bottom backscattering strength

$\mu$  is a site-specific empirical value and is a function of bottom composition and roughness, and  $\theta$  is the incident angle.

Cole et al. noted that the  $k$  value for Area Foxtrot was about 6 dB greater than the empirical value derived by Mackenzie (Cole and Podeszwa, 1974; Mackenzie, 1961). The value of  $k$  measured in Area Foxtrot is reported to vary between -18 dB and -21 dB (Bishop, 1994). This is in contrast to Mackenzie's world-wide average  $k$  value of -29 dB. A brief examination of Lambert's law will be found later in this text.

Values of  $k$  ranging from -18 to -21 dB is a good initial estimate, but may not be accurate considering the geoacoustic model developed by NPS as part of this thesis. The current backscattering strength ( $k$ ) is based on essentially the same models and procedures

used to calculate the bottom loss curve and uses the assumption that reverberation decay depends directly on bottom loss (Cole et al., 1994). Inaccurate geoacoustic parameters in the current geoacoustic model (Table 1) are expected to degrade the accuracy of the calculated bottom loss curve, reverberation decay rate and estimated value of  $k$ . Because of the influence of the geoacoustic model on these parameters, this study will examine the geoacoustic parameters of part of Area Foxtrot to validate the current geoacoustic model in use at NUWC. Since the reported model estimates of TL are consistently greater than TL measurements in Area Foxtrot (Cole et al., 1994), the potential for an error in the geoacoustic model is considered likely since sediment parameters in the model are inconsistent with Hamilton's geoacoustic models. It will also be shown that the spatial variability of the surface sediment type in Area Foxtrot is highly variable and a single geoacoustic model applied to the entire area is not adequate for performance prediction. This leads to the conclusion that geoacoustic modeling must be based on Hamilton's measurements

and that the geoacoustic model must be spatially varied as surface sediment type varies.

## B. RECOMMENDED CHANGES TO NUWC'S CURRENT GEOACOUSTIC MODEL

The current geoacoustic model uses a surface sediment compressional wave speed of 1554 m/s which was measured in Area Foxtrot from data collected in 1958 and 1959 (Barakos, 1962). This compressional wave speed is much too slow for a sand sediment with a density of 2.0 g/cm<sup>3</sup> (Hamilton, 1980) and an overall mean grain size (i.e., spatially averaged from the mean grain size of each sediment sample) of 2.01 phi units (Brocher and Ewing, 1986) in a continental terrace depositional environment (Hamilton, 1982). Note that phi size is -log<sub>2</sub> of the grain diameter in millimeters. A compressional wave speed of 1554 m/s is more consistent with a clayey-silt sediment on the continental terrace. The associated grain phi size for a clayey-silt is 7.13 phi units. An obvious discrepancy exists since the overall mean phi size was measured as 2.01 phi units (Brocher and Ewing, 1986) and the sediment was reported to be sand (Brocher and Ewing, 1986; Cole, 1956) and not

clayey-silt. The attenuation value of 0.422 dB/m/kHz as measured by NUWC is also applicable to a sand sediment and is much too high for a sediment with a compressional wave speed of 1554 m/s (Hamilton, 1980). Based on these considerations, the sediment compressional wave speed is likely much faster than 1554 m/s. Hamilton's geoacoustic measurements, made in many depositional environments, never show sediments to have such a high density and at the same time be associated with the low compressional wave speed of 1554 m/s.

The dispersion method Barakos used to determine the bottom sediment compressional wave speed may not in fact be a viable method for computing the speed of compressional waves (body waves). Barakos (1962) used a stationary tower, Texas Tower #4, near Area Foxtrot as a stationary receiving station to which information was relayed via cable from hydrophones in the ocean. Ships were deployed from Texas Tower #4 in five radial arms outward and away from the tower to a range of 150 miles (Figure 1 of Barakos, 1962). One pound explosive charges were dropped by the ships at various ranges as they headed away from the tower.

Pressure waves generated by the explosions were received by the hydrophones and data relayed to the tower. Dispersion characteristics of the pressure waves were studied and used to calculate the compressional wave speed in the bottom sediments. The average compressional wave speed along all five radial arms, each of which extends 150 miles in different directions, was reported to be 1554 m/s. However, it is not geologically feasible to use this method over the large surface area in which Barakos employed the technique, about 45,000 square miles, and then take the average of the compressional wave speed of all the surficial sediments and apply this average compressional wave speed to the entire study area. The study area includes continental terrace, continental slope and submarine canyon geologic settings, each with unique sedimentological processes and depositional characteristics. Within any of the above geologic settings, the sediment compressional wave speed will vary significantly. Averaging of sediment compressional wave speed between and throughout depositional environments yields no useful compressional wave speed for any of the environments.

Perhaps of more importance is the fact that Barakos calculated the sediment sound speed based on dispersion of the ground wave. Some surface waves such as Rayleigh and Airy waves undergo dispersion. Love waves, another type of surface wave, do not. Guided waves undergo dispersion as well. In dispersive waves, particle motion is described as an elliptical, retrograde orbit. Therefore, the speed of the wave depends on the elastic constants of material across an interface and not merely on elastic constant values at a given point as for shear and compressional body waves. Barakos' calculated speeds for the sediment are for waves at a given frequency and are not representative of compressional wave speeds within the sediment. Compressional and shear waves show such small dispersion that special investigations to determine body wave dispersion have failed (Richter, 1958).

### **C. CONSTRUCTION OF A HAMILTON GEOACOUSTIC MODEL FOR AREA FOXTROT**

Brocher and Ewing (1986) report that data were collected by the United States Geological Survey in Area Foxtrot in 1982, during which a 12-channel, high-resolution seismic reflection study was

performed. These data were collected in approximately 64 m of water, close to an existing single channel reflection profile. They found the seafloor to be underlain by about 2000 to 3000 m of sediment, the uppermost of which consists of a thin (approximately 30 m) layer of unconsolidated Pleistocene and younger sediment. This thin sediment layer unconformably overlies a middle Tertiary deltaic sequence which thickens toward the continental shelf edge. The 30 m surface sediment layer consists of reworked sediments from older, underlying sediments as well as riverine clastic debris deposited during times of lower sea level. Nine sediment samples were collected within 50 km of the seismic study area. Sediments recovered were coarse-to-fine sand. The sands coarsened toward Long Island; the overall mean grain size was 2.01 phi units. The density of the sediment was found from a core sample to be 2.0 g/cm<sup>3</sup> (Cole, 1956) and is consistent with the density of a fine-to-medium grain sand. The exact location of this core sample is not currently known.

In a continental terrace depositional environment sediment grain size will decrease seaward towards the continental shelf; this

is consistent with the sediment samples from around Area Foxtrot (Brocher and Ewing, 1986). Since Run 18 (Fisch et al., 1992), the subject of our backscattering analysis, took place in the southeastern part of Area Foxtrot and nearest to the continental slope, the grain phi size should be greater than the overall mean phi size of 2.01 phi units reported by Brocher and Ewing (1986) (greater phi size means smaller grain size diameter). The phi size of sediment in the Run 18 area was originally thought to be about 2.4 phi units or that which corresponds to a fine sand. This best-guess for grain size was made with little geologic data and no exact core or sediment sample locations.

However, an in-depth data search for sediment grab and core data has revealed much geologic data exists for the sediments in Area Foxtrot. A compilation of geologic data sets for Area Foxtrot and the surrounding area was obtained through a data search conducted at the University of Rhode Island (Shoukimas, 1995). The locations of where sediment samples were retrieved within Area Foxtrot are seen in Figure 5. The method of calculation of compressional wave speed is discussed below.

The geoacoustic models developed in this study were constructed using Hamilton's (1972, 1976, 1979, 1982) series of equations. One of Hamilton's (1982) regression equations employed here uses the sediment mean phi size to calculate the compressional wave speed for continental terrace unconsolidated sediments:

$$V_p = 1952.5 - 86.26 (\phi) + 4.14 (\phi^2) \quad (3)$$

where  $\phi$  is mean grain size in phi units

$V_p$  is compressional wave speed in m/s

Equation 3 was used to calculate the compressional wave speeds in this study. Figure 6 is a contour plot of the mean grain size in phi units in and around Area Foxtrot. An expected general coarsening of grain size toward the continental coast (northwest) is observed with smaller grain sizes (silt and clay) seen on the continental slope (southeast). Figure 7 is a contour plot of the compressional wave speeds calculated from the mean grain size in

and around Area Foxtrot. The spatial variability in sediment sound speed mirrors that of the mean grain size. From Equation 3 it can be seen that relatively small changes in grain size can translate into significant changes in compressional wave speed.

Figures 3 and 4 show the variability of surface sediment type in Area Foxtrot. Some bottom areas are covered by coarse sand while others are covered by silt-clay. These are only the two extremes of surface sediment type. There are areas of the bottom that are covered with any combination of sand and silt-clay. Therefore, there is no one geoacoustic model which correctly describes all of Area Foxtrot as originally presumed by NUWC.

Figure 8 depicts the tracks and approximate location of the surface ship and target for all runs of the September 1991 study (Cole et al., 1994) plotted with the sediment compressional wave speed in shades of grey. Although the contour interval is fine (50 m/s), it can be seen that the surface ship and target were not in the same acoustic environment. This is most evident for Runs 1-8. Runs 11-18 show the least variability in acoustic environment between the location of the ship and target.

The degree to which the difference in acoustic environment affects the transmission loss and reverberation level between the source and target is in part a function of frequency and will be addressed in future research efforts.

Figure 9 shows some sediment parameters around the surface ship track of Run 18. Notice the variability of the surface sediment even in this relatively small area. Interpolating the data, the sediment directly under Run 18 is likely 100% coarse sand with a first approximation of compressional wave speed of about 1850 m/s. This value is consistent with laboratory values for a coarse sand on the continental terrace (Hamilton, 1982) though it is slightly above Hamilton's mean compressional wave speed of 1836 m/s. The standard error of the mean of the laboratory measurements was not determined.

The associated average in situ sediment/water compressional wave speed ratio for a coarse sand bottom is 1.201 (Hamilton and Bachman, 1982). During Run 18 the water sound speed immediately above the seafloor was 1484 m/s, measured within 1.5 hours of collecting the reverberation data. Based upon the calculated

sediment compressional wave speed of 1850 m/s, a sediment /water sound speed ratio of 1.246 was obtained. This ratio is slightly higher than the above value determined by Hamilton and Bachman (1982) for a continental terrace environment, and is significantly different from the sediment/water sound speed ratio of 1.047 obtained when a sediment compressional sound speed of 1554 m/s is used from the current geoacoustic model. This latter ratio is far too low and out of range for a sandy sediment. Hence, the compressional wave speed of 1554 m/s, used in previous analyses for this area, is inconsistent with the measured geoacoustic parameters in Area Foxtrot.

The relationship between grain size and compressional wave speed is especially important because grain size analyses can be made for dried sediment for which measurements of density, porosity, and velocity can not be made. Additionally, much data on grain sizes exists in the geologic literature which can be readily used as indices of acoustic properties. Hamilton's regression equation for compressional wave speed as a function of grain size is as good or slightly better than the regression equation based on

sediment density. The standard error of estimate for mean grain size versus sound speed in continental terrace sediments is 29 m/s (Hamilton and Bachman, 1982). Hence, the compressional wave speed in the vicinity of Run 18 could range from 1821 m/s to 1879 m/s vice 1554 m/s as used in the current geoacoustic model.

As an additional validity check on our calculated sediment compressional wave speed, the average sediment/water sound speed ratio of 1.201 (Table 2 of Hamilton and Bachman, 1982) can be multiplied by the sound speed of the bottom water in our study area (1484 m/s) which yields an average in situ sediment compressional wave speed 1782 m/s. Multiplying the sediment/water sound speed ratio by sediment compressional wave speed has the effect of correcting laboratory values for full temperature and pressure corrections. Given this rather low in situ speed (1782 m/s) and the low end of the laboratory speed calculation (1821 m/s), it is likely that the true compressional sound speed lies somewhere between the two. However, it would not be a straight average of the two speeds. Since the lithology of the sediment grab nearest to Run 18 is a coarse, well-sorted sand, the true compressional wave speed of

the sediment is likely much closer to 1821 m/s. For modeling purposes, this study will use a compressional wave speed 1817 m/s, similar to the compressional wave speed measured in situ by Hamilton (1972) for a coarse sand in 34 m of water off the coast of San Diego. This, again, gives another check on the validity of the calculations for sediment compressional wave speed. The compressional wave speed given above is in relatively good agreement with the sediment compressional wave speed of 1750 m/s measured during the seismic survey of Area Foxtrot (Brocher and Ewing, 1986). It must be noted that the seismic method used in the 1986 study lends itself to an error of several hundred meters per second in determining sound speed in the sediment. Table 2 gives the elements of the NPS geoacoustic model.

To construct a more complete geoacoustic model, changes in the sediment compressional wave speed (m/s) as a function of depth in the sediment column due to overburden pressure were calculated using Hamilton's (1979) regression equation:

$$V_p = K D^{0.015} \quad (4)$$

where  $K$  is a constant ( $s^{-1}$ ) and

$D$  is depth in the sediment column (m).

To calculate  $K$  for our area of study consisting of a coarse sand bottom the following expression (Hamilton, 1979) is used:

$$K = V_{po} / 0.05 \cdot 0.015 \quad (5)$$

where  $V_{po}$  is the sediment compressional wave speed at the surface and the value 0.05 brings the surface compressional wave speed to a depth of 5 cm in the sediment and helps to correct for laboratory measurements. If speeds calculated in the laboratory only are considered,  $K$  would be  $1901.5 \text{ s}^{-1}$  and  $V_p$  at the bottom of the Pleistocene sediment layer (30 m) would be 2001 m/s. Because the determination of sediment compressional wave speed is in part based on Hamilton's (1972) in situ measurements of speed obtained at depths in the sediment between 30 cm and 60 cm, a  $K$  value of  $1817 \text{ s}^{-1}$  is deduced and the initial correction for depth is neglected.

The final equation which relates sound speed to depth is then

$$V_p = 1817 (D^{0.015}) \quad (6)$$

and the resulting compressional wave speed at the bottom of the sand layer (30 m) is 1945 m/s. As seen in Equations 5 and 6, the increase of speed with depth is not linear.

Attenuation at 3.5 kHz was determined using Hamilton's (1972) in situ attenuation measurements for coarse sand. He documented measurements of compressional wave speed and attenuation made by himself as well as from others found in the literature. Of note are three important relationships between frequency and other physical parameters which Hamilton observed from his analyses: (1) compressional wave attenuation in marine sediments is approximately related to the first power of frequency in sands, muds, and sedimentary rocks, (2) attenuation can be estimated from sediment grain size (porosity) data, and (3) attenuation in marine sediments typically increases with depth due to the reduction of sediment porosity to a point where overburden

pressure becomes the dominant effect. Beyond this point attenuation decreases smoothly as a function of depth and increased overburden pressure (Hamilton, 1976). Hamilton (1976) incorporated other attenuation measurements into his study and substantiated observation (1) above.

At 3.5 kHz, the attenuation for a coarse sand with a compressional wave speed of 1817 m/s in 32 m of water off the coast of San Diego was measured in situ by Hamilton to be 0.53 dB/m-kHz ( $k_p$  in Hamilton's notation). This corresponds to an attenuation coefficient,  $\alpha_p$ , of 1.76 dB/m at 3.5 kHz. Since the coarse sand in Area Foxtrot where Run 18 took place is in deeper water (64 m), the attenuation may be slightly less due to a small decrease in sediment porosity. But because the sand is well-sorted and there is only an additional 30 m more water overlying the Area Foxtrot sediments than the sediments off San Diego, the reduction in porosity will be very small. Attenuation may be closer to 0.5 dB/m-kHz. This attenuation value is higher than that of 0.422 dB/m-kHz (1.477 dB/m at 3.5 kHz) used in the current geoacoustic model.

Caution must be taken regarding attenuation coefficients.

Hamilton (1976) defines attenuation as "the energy lost upon transmission of a compressional wave from all causes and is thus 'effective attenuation' in most cases below the top few meters of sediments." Since 3.5 kHz will not penetrate deeply into the sand layer, it may be prudent to use an estimate of attenuation characteristic of the upper few meters of the in situ, saturated sediment. The attenuation for just the top few meters of the sand would be higher due to interstitial sea water. However, this study will use an attenuation value of 0.5 dB/m-kHz. Hamilton's (1980) attenuation ( $k_p$ ) versus depth plot is given in Figure 3 to illustrate the depth dependence of attenuation for sand and silt-clay sediments. Notice that initially the silt-clay attenuation increases with depth and then decreases while the sand sediment shows a consistent decrease in attenuation with depth.

Shear wave speed and shear attenuation were not calculated for this study since shear wave speeds are very low relative to compressional wave speeds and shear attenuation is presumed to be

negligible. Also, the transmission loss models employed do not use these parameters as input variables.

The complete NPS geoacoustic model for the sediment layer is given in Table 3 and the compressional wave speed versus depth is plotted in Figure 10 which incorporates the water sound speed profile measured for Run 18.

#### **D. LAMBERT'S LAW OF BOTTOM BACKSCATTERING**

Lambert's law relationship between backscattering strength and grazing angle has been found to be a good approximation to measured data for many deep water, very rough bottoms at grazing angles below about 45° (Urick, 1983). Moreover, this relationship between backscattering strength and angle appears to be frequency independent. Mackenzie's (1961) optimum value for "k" (i.e.,  $10 \log \mu = k$ ) was about -29 dB which he felt adequately described the scattering strength of clay, mud, silt and fine sand bottoms at frequencies between 0.5 kHz and 100 kHz. However, the predictable behavior given in Lambert's law applies only to what Urick (1983) refers to as a Type III acoustic bottom, i.e., a heavily dissected bottom with underwater ridges for which Lambert's law is invariant

in frequency. However, various data suggest a definite frequency dependency for smoother (mud, clay and sand) bottoms (Urick, 1983). Sand and silt bottoms show a rise in scattering strength with frequency at the rate of about 3 dB/octave (or a variation as the first power of the frequency), whereas little or no frequency dependency appears to exist for rock, sand and rock, or silt and shell bottoms. Urick attributes this difference in frequency dependency as possibly due to the difference in the scale of bottom roughness. Bottoms with roughnesses large compared to a wavelength have a backscattering strength independent of frequency. Bottoms with an appreciable portion of their roughness spectrum at roughnesses less than an acoustic wavelength will have a scattering strength which increases with frequency. Later in this study, measured reverberation data will be compared to modeled reverberation levels using various values for  $10 \log \mu$  to determine if bottom scattering strength follows Lambert's law in Area Foxtrot.

Table 1. The current geoacoustic model parameters for Area Foxtrot.

Compressional Sound Speed of the Sediment	Density of the Sediment	Attenuation of the Sediment
1554 m/s	2.0 g/cm <sup>3</sup>	0.422 dB/m-kHz

Table 2. Some NPS geoacoustic model parameters for the sand bottom in Area Foxtrot.

Compressional Sound Speed of the Sediment	Density of the Sediment	Mean Grain Size of the Sediment in Phi Units	Attenuation of the Sediment
1817 m/s	2.6 g/cm <sup>3</sup>	1.33 phi units	0.5 dB/m-kHz

Table 3. Compressional sound speed versus depth in the NPS geoacoustic model - includes water column and sediment layer.

Depth (m)	Speed (m/s)	Depth (m)	Speed (m/s)
0	1519.00	73	1937.78
6.25	1518.00	74	1938.18
12.5	1516.00	75	1938.57
18.75	1512.00	76	1938.95
25	1505.00	77	1939.33
31.25	1506.00	78	1939.71
37.5	1500.00	79	1940.08
43.75	1496.00	80	1940.44
50	1493.00	81	1940.81
56.25	1490.00	81	1940.81
62.5	1488.00	83	1941.52
64	1484.00	84	1941.87
64.0001	1817.00	85	1942.21
65	1934.41	86	1942.55
66	1934.85	87	1942.89
67	1935.29	88	1943.22
68	1935.72	89	1943.55
69	1936.14	90	1943.88
70	1936.56	91	1944.20
71	1936.97	92	1944.52
72	1937.38	93	1944.83
		94	1945.14

#### **IV. TRANSMISSION LOSS MODEL SENSITIVITY to INPUT GEOACOUSTIC PARAMETERS**

Now that a detailed Hamilton geoacoustic model (the NPS model) has been developed for Area Foxtrot, a TL model can be used to accurately calculate TL using the NPS geoacoustic parameters as input. The TL model that we chose to evaluate in this study is the GSM/MPE model provided to NPS by Dr. Judith Bishop of NUWC with permission from Mr. Ed Chaika of AEAS. GSM/MPE is a relatively new model but was chosen because it is very user-friendly and readily calculates TL, RL and other active sonar model parameters.

##### **A. THE GSM/MPE PROPAGATION MODEL**

The GSM/MPE (or GSM) model allows the user to input variables into a variety of sub-models which are used to calculate TL and RL. The model is menu-driven and easy to use. The sub-model categories are: (1) surface reflection, (2) volume attenuation, (3) bottom reflection, (4) bottom phase (5) transmit beam pattern, and (6) receive beam pattern. Each of the six sub-model categories consists of one or more sub-models or a user-defined function which

is selected by the user. User inputs include minimum and maximum ranges, range increments, minimum and maximum frequency, frequency increment (if a frequency range is used), surface and bottom depths, source and target depths, eigenray tolerance, sediment attenuation, ocean/sediment sound speed ratio, sediment/ocean density ratio, wind speed, beam patterns and ocean sound speed profile. Other inputs may be required depending on the sub-models selected.

GSM defaults to the Rayleigh reflection coefficient for bottom loss but a bottom loss versus grazing angle curve may be inserted by the user. GSM does not include a complete geoacoustic model of the sub-bottom (sediment) in its TL calculations. Only geoacoustic parameters at the surface of the sediment are used and the change in these parameters with depth is not addressed. This may be a significant weakness in using GSM in shallow water since it will be shown later in this study that the sediment layer can refract a significant amount of energy back into the water column. In deep water the erroneous concept of "negative bottom loss" was introduced because the impact of sub-bottom energy returned to the

water column was not addressed. In shallow water the impact of sub-bottom returned energy should be greater than in deep water. Therefore, this returned energy must be modeled accurately.

Two TL calculations were performed, one for the current geoacoustic model (essentially a silt-clay bottom) (Table 1) and one for the NPS geoacoustic model (sand bottom) (Table 2) based on geologic data acquired near Run 18. Only the geoacoustic parameters of sediment attenuation, ocean/sediment sound speed ratio and sediment/ocean density ratio in the bottom reflection (Rayleigh reflection) sub-model were varied between the two TL runs. The variables and sub-models used for each TL run are given with each TL plot. Note that a source depth of 7.3 m and a receiver depth of 64 m (same as bottom depth) was used because we are primarily concerned with bottom backscattering in this study. The placement of the receiver on the ocean floor will give TL calculated from the source to the bottom where bottom backscatter occurs (Figure 11).

Figures 12 and 13 are the GSM TL plots for the NPS and the current (NUWC) geoacoustic models, respectively. Dr. Henry Weinberg of NUWC also ran these TL cases to verify the results.

Close comparison of Figures 12 and 13 shows that, as expected, poorer propagation occurs for the current geoacoustic model. At 15 km the NPS model shows about 75 dB loss where the current geoacoustic model shows about 81 dB loss, a difference of about 6 dB. At 20 km the current geoacoustic model shows about 8 dB more loss than the NPS model. These plots are presented to demonstrate the high sensitivity of TL between the two geoacoustic models and shows that the silt-clay sediment yields significantly more loss than the sand sediment. Recall, Area Foxtrot sediments are spatially variable and no one geoacoustic model can be applied to the entire area.

The above calculations were performed using an eigenray tolerance of 0.10. Eigenray tolerance reduces (increases) the running time of the multipath eigenray model by increasing (decreasing) the convergence tolerance. Convergence is assumed when the difference in random addition between consecutive ray cycles is less than the eigenray tolerance indicated (Weinberg, 1985). The TL calculations were performed again but with an eigenray tolerance of 0.0010 to try and increase the accuracy of the

TL by including more eigenrays in the calculations. Figures 14 and 15 are the GSM TL plots with the lower eigenray tolerance for the NPS and current geoacoustic models, respectively. Comparison of Figures 12 and 14 (NPS model) and of Figures 13 and 15 (current model) shows very little difference in TL between the two eigenray tolerance settings. However, since the calculation time is only a few seconds greater for the smaller eigenray tolerance, it was used for all subsequent TL calculations in this thesis.

The TL was then calculated for both the NPS and current geoacoustic models using the Finite Element Parabolic Equation (FEPE) model to illustrate the sensitivity of TL to bottom geoacoustic properties. The results are discussed in the next section.

## B. THE FEPE PROPAGATION MODEL

The FEPE model has been used at NPS and elsewhere for several years and has been found to be very accurate by a large number of scientists (Chin-Bing et al., 1993). It is less user-friendly than the GSM model and takes much longer to run but has the advantage of including a full Hamilton-type geoacoustic model of the sub-bottom

as input. That is, where the GSM model uses only the compressional wave speed and density ratios across the water/sediment interface, and one value of sediment attenuation, FEPE allows the sediment compressional wave speed, density, and attenuation to vary with depth and range. As such, FEPE accounts for modes propagated into and out of the sediment layer. Although FEPE is normally used with lower frequencies, it can be used for our frequency of interest, 3.5 kHz (Campbell, 1995). Care must be taken however when selecting the resolution of the calculations. In this study, a range increment of one quarter acoustic wavelength ( $\lambda/4$ ) and a depth resolution of one eighth acoustic wavelength ( $\lambda/8$ ) was used (Campbell, 1995). FEPE can also be used in range-dependent seafloor environments. The bottom in Area Foxtrot is range-dependent (Figures 6, 7, 8, and 9). However, since the purpose of these TL estimates is to show the impact of bottom geoacoustic properties on TL (and ultimately RL), a range-independent bottom environment is assumed.

The NPS model input to FEPE (Table 3) incorporated a depth-dependent compressional wave speed, density and attenuation in the

30 m sediment layer according to Hamilton's equations (Hamilton, 1976, 1979). Below the sediment layer is an attenuating half-space. The current geoacoustic model input to FEPE was the same as that input to GSM. For this situation, no depth dependence of geoacoustic parameters were permitted since they were not part of the current model (and are not considered in GSM).

Figure 16 shows the TL results from FEPE for the NPS and current geoacoustic models for a source at 7.3 m and receiver at 64 m. Notice the significant difference in TL as range increases. At 5 km the current model shows about 10 dB more loss than the NPS model, at 10 km and 15 km the difference increases to about 18 dB and 23 dB, respectively. For comparison, TL was calculated using FEPE for both geoacoustic models but with the source and receiver both at 7.3 m (Figure 17). The TL for each geoacoustic model is slightly less than that when the receiver is at the bottom (64 m). However, the relative difference between TL for the two geoacoustic models is the same whether the receiver is at the bottom or at the source depth. Figure 18 is a combination of Figures 14 and 15 and

shows TL for the NPS and current geoacoustic models for each source/receiver geometry.

This dramatic difference in TL with range when modeling a "hard", coarse sand bottom with a sediment compressional wave speed of 1817 m/s (NPS model) and a "soft" bottom with a sediment compressional wave speed of 1554 m/s (current model) shows the importance of knowing the correct geology and geophysics of a study area before constructing geoacoustic models. Figures 6 through 9 show the spatial variability of surface sediment type in Area Foxtrot. The sediment type can also vary with depth although these data were not readily available for this study.

### **C. COMPARISON OF GSM AND FEPE TL CALCULATIONS FOR THE SAME GEOACOUSTIC MODEL**

TL curves calculated using the current geoacoustic model as input to the GSM and FEPE models were plotted together for comparison (Figures 19 and 20) in order to quantify and illustrate the difference, if any, in their TL estimates. The GSM TL energy levels were summed both coherently (phased summation) and incoherently (random summation) while the FEPE levels were

summed coherently. These figures show that the GSM and FEPE TL curves are in agreement out to about 2.5 km in range. Beyond that, the curves diverge and show that the GSM TL curve underestimates the loss relative to FEPE which includes the full geoacoustic model. At a range of 10 km the GSM TL is about 7 dB less than the FEPE TL and at 15 km the difference has increased to about 13 dB less loss.

The difference in the TL calculations and divergence of the TL curves is likely due to how the models handle the physics of reflection at the bottom interface and refraction into and out of the sub-bottom sediments as well as the modeled geology. The soft bottom current model has a critical angle at the sediment interface of 17° which means that more energy from an omnidirectional source will penetrate into the bottom than for a harder bottom which will have a larger critical angle. The two TL curves agree at short ranges (less than 2.5 km), for high grazing angles and for relatively few bottom bounces. But as range and the number of bottom bounces increase, GSM does not account for enough energy loss into the sediment layer. Because GSM underestimates the loss per bottom interaction and overestimates the reflection coefficient

at the sediment interface, the GSM and FEPE curves diverge. The term "bottom interaction" is applied instead of "bounce" because with a soft, mud bottom energy will penetrate the sediment and be scattered and attenuated within the sediment during refraction back up toward the water column. Hence, not all the energy incident on the bottom is truly "bounced" from the interface. Therefore, as the number of bottom interactions increases, the separation between the TL curves increases. Because the GSM model only considers bottom loss from the water / sediment interface as a function of grazing angle and does not include the entire geoacoustic model (i.e., within the sediment layer), it fails to account for the additional TL due to attenuation and refraction within the sediment. FEPE does account for the entire geoacoustic model of the sub-bottom and attenuation of energy refracted through the sediment and back into the water column.

TL estimates calculated for the NPS geoacoustic model (hard sand bottom) using GSM (phased and random TL) and FEPE (phased TL only) are compared in Figures 21 and 22. Here, the TL curves show a nearly constant difference of about 5 dB out to 15 km range. The

GSM TL estimates show more loss than the FEPE TL estimates for the NPS geoacoustic model (hard bottom). Also, the two TL curves do not diverge with range due to the harder bottom modeled where much less energy is refracted through the sediment layer and back into the water column. Therefore, attenuation within the sediment is not as significant a factor for the hard bottom and bottom interactions can be treated as "bottom bounces".

Since the sub-models within GSM can not accurately estimate TL in shallow water, the TL curves from GSM will be corrected by adding in TL corrections determined from the FEPE estimates. This will allow us to still use GSM to estimate reverberation levels from the corrected TL estimates.

NUWC has addressed this problem by calculating bottom loss using the Seismo-Acoustic Fast Field Algorithm for Range Independent Environments (SAFARI) model and importing these curves into GSM to estimate TL (Jensen, 1995). This procedure shows some merit as TL estimates from GSM using the SAFARI bottom loss curves do compare well to some measured TL curves for a small part of Run 18. The FEPE TL curves also compare well to the

measured TL. It must be noted that the TL measurements were collected between the surface ship and the target submarine (Figure 8). Energy propagation through this path is over both sand and silt-clay bottoms (Figure 7). Therefore, more than one geoacoustic model is required to properly estimate TL.

NPS has chosen to use FEPE (instead of SAFARI) to augment GSM because it accounts for energy that is refracted within the sediment and returned to the water column. FEPE is also likely to become the Navy standard Oceanographic and Atmospheric Master Library (OAML) approved shallow water TL model. However, the main point stressed by Figures 16 through 20 is that GSM requires an additional model (whether it be SAFARI or FEPE) to correctly account for the sub-bottom interacting energy, even at 3.5 kHz. FEPE correctly addresses the propagation of the sub-bottom refracted energy that is returned to the water column. This avoids the need to incorporate the "negative bottom loss" energy concept introduced in the mid-1980's to overcome the fact that energy refracted back into the water column by sediments was neglected in deep water bottom loss models.

## V. BOTTOM BACKSCATTER

### A. THE SAIC METHOD OF ANALYSIS TO DETERMINE BOTTOM SCATTERING STRENGTH (AND THE DOMINANT BOTTOM SCATTERING MECHANISM)

Estimation of bottom scattering strength is normally conducted by direct measurement methods (Urick, 1983; McCammon, 1993). Direct measurements of bottom backscattering strength can yield misleading results if the acoustic / geologic environment of the study area is not well known (this point is addressed in detail later in this study). SAIC has developed a method by which bottom scattering strength may be deduced through comparison of measured and modeled RL. This method has the advantage of including full Hamilton-type geoacoustic models in the analysis.

The following reverberation data analysis technique was conducted by SAIC (Hanna et al., 1994) as part of the Harsh Environments Program (HEP) of the Office of Naval Research. Their methods and results are described below.

## B. DETERMINATION OF SEAFLOOR SCATTERING STRENGTH AND BACKSCATTER

The first point to establish in the analysis of the data is to determine which bottom scattering mechanism controls bottom reverberation in Area Foxtrot, realizing that more than one mechanism may be present. Scattering may be either at the water-bottom interface or within the bottom sediments. Further, if the dominant scattering mechanism is found to be within the bottom sediments, the bulk of the scatter could then be due to either inhomogeneities within the sediment or from layering (macro or micro) within the sediment column. For clarity, scattering from the water-bottom interface will be referred to as bottom interface scatter. Scattering from within the bottom sediments will be referred to as bottom volume scatter. The bottom scattering strength equation can then be written as

$$S_b = A(S_{bi}) + B(S_{bv}) \quad (6)$$

where  $S_b$  is the total bottom scattering strength,

A and B are relative percentages,

$S_{bi}$  is the scattering strength at the ocean-sediment interface, and

$S_{bv}$  is the scattering strength within the sediment volume.

Due to the nature of this study, we assume the reverberation-limited case of the active sonar equation to be:

$$SE = (SL - TL_{st} + TS - TL_{tr}) - RL - DT \quad (7)$$

$$RL = (SL - TL_{sb} + S_b + 10 \log(A) - TL_{br}) \quad (8)$$

where SE is the signal excess,

SL is the source level,

$TL_{st}$  is the transmission loss along source to target path,

TS is the target strength,

$TL_{tr}$  is the transmission loss along target to receiver path,

RL is the reverberation level,

$TL_{sb}$  is the transmission loss from source to bottom path,

$S_b$  is the scattering strength,

$A$  is the reverberating bottom area

$TL_{br}$  is the transmission loss from the bottom scattering

area along the path to receiver, and

$DT$  is the detection threshold.

Equation 7 is often written in a specialized form for shallow water cases. In this case, it is assumed that the reverberation originates from the bottom interface and that the propagation path to that bottom area is the same as the path to the target at equal range. Using this assumption, all the propagation terms in Equations 7 and 8 cancel leaving signal excess a function of target strength, detection threshold, scattering strength and the area term. Equation 7 then becomes:

$$SE \approx TS - DT - S_b - 10 \log(A) \quad (9)$$

and the reverberation equation is then

$$RL = SL - 2TL + S_b - 10 \log(A) \quad (10)$$

where  $2TL$  is the 2-way transmission loss.

Here, we assumed that  $TL_{st} \approx TL_{sb}$ , and  $TL_{tr} \approx TL_{br}$ . Implicit in these approximations is that the scattering mechanism is of the bottom interface type. Earlier studies used these same assumptions in attempting to estimate the bottom scattering strength (Urick, 1983). Note that since the direction of scatter is back to the source for monostatic sonars, scattering strength can be more specifically referred to as backscattering strength.

The SAIC method starts by fitting the measured propagation loss from the source to the receiver to a curve. The reverberation level  $s$  is then calculated using existing models under the assumption of zero scattering strength ( $S_b = 0$ , or  $SS=0$  in Hanna et al., 1994 terminology). The measured propagation curve (data) is then subtracted from the modeled reverberation curve ( $S_b = 0$ ). The

difference between the two curves (Modeled - Data) is assumed to be the backscattering strength if all other reflection and scattering mechanisms are properly accounted for in the model. As seen in Figure 23, the resulting backscattering strength curve is range dependent because the modeled and measured decay rates are obviously different. However, this implies that the scattering strength is not only a function of backscattering at the bottom interface, but also may include sub-bottom volume scattering geoacoustics (Mourad and Jackson, 1993; Stephen, 1993; Ellis et al., 1993; Jackson, 1992). Scattering strength should not have a position dependence that varies monotonically with distance to the receiver assuming a homogeneous bottom. The reverberation data in Figure 23 are for the octave band centered at 100 Hz and are for the Nile Fan, but similar results have been found to hold for the Korean shallow water areas (Hanna et al., 1994).

Figure 24 shows the same analysis as the previous figure but for 800 Hz. This implies that the scattering strength anomaly is seen across the frequency band from 100 Hz to 800 Hz.

For sediment volume scattering to be important in the scattering strength term, energy must penetrate into the ocean bottom. In ray theory terminology, this implies that acoustic energy must penetrate the bottom interface with an angle greater than the critical angle. In shallow water regions, the sediment is often composed of at least some fractional portion of sand which causes the sound speed ratio at the ocean-sediment interface ( $C_{\text{water}}/C_{\text{sediment}} = n$ ) to be less than unity and the ratio of densities ( $\rho_{\text{sediment}} / \rho_{\text{water}} = m$ ) to be greater than  $n$ . This case is most commonly found in naturally deposited bottom sediments and results in complete reflection from the interface for grazing angles less than the critical angle (Urick, 1983 p. 137). In the case of a bottom comprised of a soft mud or saturated ooze, the  $C_{\text{water}}/C_{\text{sediment}}$  ratio may be greater than unity and little reflection takes place; most of the energy is transmitted into the sediment until an angle of intromission is reached when all of the energy is transmitted into the bottom.

Thus, while bottom interface scattering can effect all rays impinging on the bottom, bottom volume scatter can only effect

those rays which have bottom grazing angles greater than the critical angle. Figure 25 shows that for bottom interacting rays, energy loss associated with angles below the critical angle will decay with range less rapidly than that for rays greater than the critical angle. This difference results because acoustic energy that penetrates into the sediment layer will be attenuated at a faster rate due to the higher attenuation coefficient of the sediment compared to the water.

Consequently, we will take measured reverberation levels and subtract out modeled reverberation levels for which the scattering strength ( $S_b$ ) is assumed to be zero. What remains should be the actual bottom scattering strength ( $S_{bi} + S_{bv}$ ). By inspection of the energy loss decay as a function of range in the bottom scatter curves, we will be able to determine whether bottom interface or bottom volume scatter is the dominant scattering mechanism.

Having determined the dominant scattering mechanism at the bottom, we can better evaluate the bottom scattering kernel and physics involved in backscatter from the bottom.

### C. USING THE SAIC ANALYSIS METHOD TO DETERMINE BOTTOM SCATTERING STRENGTH ( $S_b$ ) FROM AREA FOXTROT DATA

The GSM model was run to calculate the reverberation level using the NPS geoacoustic model with the bottom scattering strength set to zero as described above. The model results were then subtracted from the measured RL data. Theoretically, the remaining curve should describe the bottom scattering strength as a function of time. Figures 26, 27 and 28 compare the modeled RL ( $S_b = 0$ ) with the measured RL data (upper panels) and the difference between the two curves for beams 1, 12 and 24, respectively, for ping 2 of Run 18 (lower panels). Also shown is a 3rd-order polynomial fit to the reverberation level difference. This curve can be used as a measure of the bottom scattering strength. Note the difference between the modeled and measured reverberation levels for each beam. The plots for beams 1 and 24 show about a 65 dB difference at 20 seconds whereas beam 12 shows about a 70 dB difference. Also, the bottom scattering strength curve for beam 12 has a greater slope than the curves for beams 1 and 24. This indicates that the bottom scattering strength for beam 12 more

closely approximates that given by Lambert's law than the scattering strength for the other two beams. Recall that beams 1 and 24 propagate mostly over a silt-clay bottom whereas beam 12 was mostly over a coarse sand bottom (Figures 6 through 9). This difference in sediment properties causes an azimuthal dependence of bottom scattering strength which in turn causes an azimuthal dependence in the reverberation level.

The RL was next calculated using the NPS sand bottom model as input with the bottom scattering strength described by a Lambert's law formulation:

$$S_b = -19.5 + 10 \log \sin^2 \theta. \quad (11)$$

These RL values were compared with measured RL data for the odd-numbered beams for pings 2, 30 and 60 (Figures 29 (a-d), 30 (a-d) and 31 (a-d), respectively), to see if the azimuthal dependence of reverberation was a consistent feature. As seen in these figures, azimuthal dependence of reverberation is evident from ping 2 through to ping 60. Note that the GSM modeled RL is not very

accurate due to the inherent limitation of the model in estimating TL as discussed earlier.

To further examine the dependence of reverberation level on azimuth angle, the measured reverberation level was plotted as a reverberation surface (ignoring beam angle in the display) for all beams for pings 2, 20, 40, 60 and 88 (Figures 32, 33, 34, 35 and 36, respectively). This essentially shows how RL changed as a function of distance, i.e., as the acoustic source moved eastward during Run 18. Figure 37 is a three-dimensional surface plot of the reverberation field for ping 88, approximately 5 km distance from ping 2. These reverberation surfaces show the azimuthal dependence of reverberation very well. It is easily seen in Figures 32 through 37 that as time increases, reverberation levels for the beams steered ahead towards the harder, sand bottom (beams 6-19) maintain higher levels than the peripheral beams (beams 1-5 and 20-24) steered toward the softer, mud bottom. Beams to the right of center (beams 1-5) show the greatest reduction in reverberation with time and also that the degree of change across the beam spectrum changes from ping to ping. This implies an inhomogeneous

bottom in the area of Run 18 which is consistent with the NPS geoacoustic contours in Figure 7.

The azimuthal dependence of reverberation can be explained by the local geology. Referring back to the surface sediment compressional wave speed plots (Figures 7 and 8) it is seen that for Run 18 the more central beams of the sonar interact with a higher speed bottom for a much longer time than the peripheral beams. The peripheral beams interact with a slower, silt-to-clay bottom which lies to the left and right of the high speed sediment. This high speed bottom forms essentially a strip which lies somewhat along the track of the surface ship. The slowest speed bottom is found to the right of the surface ship track where the lower number beams (1-5) interact with the bottom. This increased bottom penetration for the peripheral beams explains the reduction in reverberation level with time and also explains why the reverberation trend for the peripheral beams does not follow Lambert's law. Energy which impinges the soft bottom will enter the sediment and be attenuated within the sediment. Bottom scatter in this case will not obey Lambert's law and is assumed to be a function of  $\sin \theta$  (Mourad and

Jackson, 1993; Jackson and Briggs, 1992) vice  $\sin^2 \theta$ . The value of  $10 \log \mu$  may also vary and is in part a function of the interface roughness.

To quantify the bottom scattering strength, reverberation levels from GSM need to be adjusted to account for the inherent errors in the GSM TL estimates (when bottom loss is calculated from Rayleigh reflection coefficients). This is most easily done by measuring the difference in TL between the GSM and FEPE estimates, then multiplying this difference by two (to account for two-way travel time) and adding this quantity to the GSM reverberation levels. This method of correcting the GSM reverberation levels is consistent with Equation 10. However, due to the lateral inhomogeneity of the surface sediment (and thus compressional speed), a second Hamilton-type geoacoustic model was developed in addition to the NPS sand bottom. This model is for a silt-clay bottom with a surface sediment compressional wave speed of 1580 m/s. The FEPE model was also run to estimate the TL for the NPS silt-clay bottom which included the full Hamilton geoacoustic model.

GSM reverberation levels were corrected (for TL) for beams 1, 12, and 24 of pings 2, 40, 60, and 88. These beams were chosen because they were likely to be steered in the least range-dependent azimuths (Figure 7). Different bottom scattering strength kernels were incorporated into the NPS sand (beam 12) and NPS silt-clay (beams 1 and 24) geoacoustic models. TL was corrected as described earlier. Beams 1 and 24 were modeled for propagation over the NPS silt-clay bottom while beam 12 was propagated over the NPS sand bottom. Figures 38 (a-e), 39 (a-e), and 40 (a-e) show measured reverberation levels plotted with uncorrected GSM RL in the upper panel, and measured reverberation levels plotted with GSM RL with corrected TL errors, for three different bottom scattering strength kernels (bottom panel). On initial inspection of the ping 2 plots, for beam 1 (Figure 38a) (NPS silt-clay bottom) the "best fit" bottom scattering strength kernel appears to be  $S_b = -35 + 10 \log \sin(\theta)$ . For ping 2, beam 12 (Figure 39a) (NPS sand bottom) it appears that none of the proposed bottom scattering strength kernels fits the measured data throughout the entire 20 second reverberation time series. For ping 2, beam 24 (Figure 40a) (NPS silt-clay

bottom) the "best fit" bottom scattering strength kernel appears to be  $S_b = -33 + 10 \log \sin (\theta)$ . Similar observations are made for pings 60 and 88. However, close examination of Figures 38a, 39a, and 40a in conjunction with the best geologic and geoacoustic data available (Figures 5 and 6) show some very interesting results.

For instance, beams 1 and 24 (Figures 38a through 38e and 40a through 40e) show that modeled RL for a silt-clay bottom with a bottom scattering strength kernel employing  $10 \log \sin (\theta)$  generally fits the measured RL very well throughout the entire time series. This kernel is consistent with a bottom volume scattering mechanism proposed by Jackson and Briggs (1992) and Mourad and Jackson (1993). But Figures 6 and 7 show the bottom in the immediate vicinity of the surface ship to be the NPS sand type bottom. The bottom type does change with increased range becoming more like the NPS silt-clay bottom along the azimuths of beams 1 and 24. The bottom scattering kernel for a silt-clay bottom is not expected to fit the entire measured RL time series accurately when the initial propagation of ping 2 is over hard sand.

To further investigate this range-dependence in  $S_b$ , the GSM RL, using the NPS sand bottom as input, was compared with the GSM RL for the silt-clay bottom and with the measured RL for beam 1 of ping 2 (Figure 41). Figure 39 shows that for beam 1 of ping 2, GSM RL (with corrected TL) for the NPS sand bottom using a bottom scattering strength kernel of  $-33 + 10 \log \sin^2(\theta)$  fits the measured RL as well as the  $-35 + 10 \log \sin(\theta)$  kernel out to about 7.5 seconds. From 7.5 seconds to 20 seconds the  $-35 + 10 \log \sin(\theta)$  kernel fits the measured RL whereas the  $-33 + 10 \log \sin^2(\theta)$  kernel overestimates RL. For beam 1 of ping 2, it appears that at least two different geoacoustic models (sand and silt-clay) are required to describe the bottom over which the beam propagates. And each geoacoustic model requires a different bottom scattering strength kernel to estimate RL. For the sand bottom in the vicinity of the ping origin (out to 7.5 sec)  $-33 + 10 \log \sin^2(\theta)$  appears to be the appropriate bottom scattering strength kernel. However, for the silt-clay bottom (beyond 7.5 sec)  $-35 + 10 \log \sin(\theta)$  better describes bottom scattering strength. Using these two geoacoustic

models is consistent with the geology of Area Foxtrot (Figures 6 and 7).

There are three variables which account for the shape of the RL curve (RL as a function of time or range) in Figure 41: 1) the TL as a function of range, 2) Mackenzie's coefficient ( $10 \log \mu$ ), and 3) whether the angular dependence is  $\sin(\theta)$  or  $\sin^2(\theta)$ . Factors 1 and 3 above may be linked to a specific sediment type (Jackson and Briggs, 1992; Mourad and Jackson, 1993). A silt-clay bottom should exhibit a TL trend that increases more rapidly with range (poorer propagation) than a hard sand sediment (Figures 16 and 17). The silt-clay sediment is also a possible source of volume reverberation (Jackson and Briggs, 1992; Mourad and Jackson, 1993) in which the bottom scattering strength kernel would not obey Lambert's law ( $\sin^2(\theta)$ ) but would be a function of  $\sin(\theta)$ . This is due to the shallow grazing angles and "diffuse" acoustic impedance across the ocean / silt-clay interface which allows increased energy penetration into the sediment. Note that an angular dependence of  $\sin(\theta)$  should yield a higher bottom scattering strength than for

$\sin^2(\theta)$ , but the sediment attenuation effectively offsets this increase and may reduce bottom scattering and RL to levels below those found when the angular dependence is  $\sin^2(\theta)$ . In the case of Figure 41, the difference between the  $10 \log \mu$  values for the sand and silt-clay bottoms is 2 dB and is negligible. This suggests that it is the TL trend and angular dependence that dominates the RL trend.

For comparison, the sand bottom was then assigned a bottom scattering strength kernel of  $-35 + 10 \log \sin(\theta)$  and the silt-clay bottom was assigned a bottom scattering strength kernel of  $-33 + 10 \log \sin^2(\theta)$ , i.e., the bottom scattering strength kernels were switched for the two models. This separates the TL trend and the angular dependence of RL. As seen in Figure 42 neither of the bottom type/bottom scattering strength kernel combinations correctly model the measured RL. Remembering that there are three variables presented here which affect the RL trend (with time or range),  $10 \log \mu$  was varied in the bottom scattering strength kernel for the silt-clay bottom and employed  $\sin^2(\theta)$  (Lambert's law) in the kernel to see how well it could fit GSM RL to the measured RL.

Surprisingly, GSM RLs for the silt-clay bottom using two very different bottom scattering strength kernels ( $-35 +10 \log \sin(\theta)$  and  $-17 +10 \log \sin^2(\theta)$ ) are nearly perfectly coincident (Figure 43).

Figure 44 is an expanded view of Figure 43 to enhance the minor differences in the RL curves. Figure 45 is the same as Figure 43 except the sand bottom is used in modeling RL with the bottom scattering strength kernel of  $-33 +10 \log \sin^2(\theta)$  (GSM RL) curve also included.

To explain the similarity of the RL curves in Figure 43, the two bottom scattering strength kernels were plotted as a function of grazing angle (Figures 46 and 47). Notice that at very low grazing angles (less than about  $3^\circ$ ) the bottom scattering strength from the two very different bottom scattering kernels (and hence mechanisms) are similar. Since the depression angle of the sonar in this study is  $3^\circ$ , the grazing angle in the study site is about  $2.9^\circ$ . Figure 47 suggests that there should be less than a 5 dB difference between the two bottom scattering strength kernels. However, even small variations in the temperature of the water mass for Run 18

could further decrease the bottom grazing angle and reduce the difference between bottom scattering strength kernels (Figure 47). Therefore, the similarity of modeled RL curves using the two different bottom scattering kernels is not surprising. The very good curve fit of the two modeled RLs to the measured RL is also expected. However, the near coincidence of the two modeled RL curves was not expected and is likely due to the water temperature (downward refracting) and hence very shallow grazing angles.

Because of the low depression angle of the sonar, and hence low grazing angle of the acoustic energy, at least two bottom scattering kernels can describe the bottom scattering strength. Each of the kernels represents different scattering mechanisms governed by different physics. But only one mechanism is correct. Wong and Chesterman (1968) concluded that for grazing angles between  $0.5^\circ$  and  $6^\circ$ , bottom scattering strength was consistent for powers of  $\sin(\theta)$  ranging from 0 to 1.5. The National Defense Research Council (1946) and McKinney and Anderson (1964) arrived at the same conclusion. McCammon (1993) suggests that this may be due to volume scattering at such low grazing angles. However,

constancy of bottom scattering strength at low grazing angles seems more likely a remnant of the mathematics (more than two free parameters) used to quantify bottom scattering ( $10 \log \mu$  and the power of  $\sin(\theta)$ ) and the TL characteristic of the bottom (Figures 41, 42, and 43).

There are then four possible bottom scattering strength kernel variations which fit the GSM RL estimates to the measured RL for beam 1 of ping 2 (Table 4). Based again on geology (Figures 6 and 7), kernels 1 and 2 of Table 4 are likely candidates for the one correct bottom scattering strength kernel since beam 1 initially propagates over sand and then propagates over silt-clay. Considering that acoustic energy penetrates the silt-clay sediment and is refracted in the sub-bottom and not simply reflected from the water/sediment interface (Figure 19 and 20), it is not logical to presume a simple Lambert's law scattering mechanism throughout the propagation path since this law is based on scattering at the water/sediment interface. A volume scattering mechanism ( $\sin(\theta)$ ) is more applicable to a silt-clay bottom because of increased penetration of

the acoustic energy. Volume scattering from silt-clays is supported by the works of Jackson and Briggs (1992) and Mourad and Jackson (1993). This supports the conclusion that in the first 7.5 seconds of reverberation for ping 2, beam 1, propagation is over the sand bottom. Beyond 7.5 seconds reverberation propagation is over the silt-clay bottom type. Hence, kernel number 1 of Table 4 is then the correct combination of bottom scattering strength kernels to quantify and describe the bottom scattering along beam 1 of ping 2.

Thus, even for a single beam of a ping, at least two geoacoustic models with different bottom scattering strength kernels are required to model the ocean bottom in this local of Area Foxtrot.

Interestingly, Cole and Podeszwa (1974) published bottom scattering strength measurements in Area Foxtrot over a reportedly sand bottom for grazing angles near  $15^\circ$ . They showed the bottom scattering strength to be  $-29 + 10 \log \sin(\theta)$ . This measurement is comparable to the bottom scattering strength of  $-35 + 10 \log \sin(\theta)$  for the silt-clay bottom as determined in this study.

Hence, without some prior detailed knowledge of the geology of Area Foxtrot, one could have easily used a silt-clay geoacoustic model and applied a bottom scattering strength using  $\sin(\theta)$  to the entire RL time series for beam 1 of ping 2. This would have been wrong in light of the local geology.

Table 4. Four possible bottom scattering strength kernel scenarios that fit GSM/MPE RL to measured RL.

$S_b$ kernel #	Time 0 - 7.5 (sec)	Time 7.5 - 20 (sec)
1	-33 +10 log sin <sup>2</sup> ( $\theta$ )	-35 +10 log sin ( $\theta$ )
2	-33 +10 log sin <sup>2</sup> ( $\theta$ )	-17 +10 log sin <sup>2</sup> ( $\theta$ )
3	-35 +10 log sin ( $\theta$ )	-35 +10 log sin ( $\theta$ )
4	-17 +10 log sin <sup>2</sup> ( $\theta$ )	-17 +10 log sin <sup>2</sup> ( $\theta$ )

#### D. CURVE FITTING OF BOTTOM SCATTERING STRENGTH

Figure 48 shows the two bottom scattering angular dependencies of  $\sin(\theta)$  and  $\sin^2(\theta)$  but neglects the  $10 \log \mu$  and the TL dependence of bottom scattering strength. Volume scattered energy is affected by the TL in the sediment layer since it propagates within the sediment. Normally, one would expect higher RL when the angular dependence is  $\sin(\theta)$  (Figure 48). However, the TL within the sediment can reduce RL to levels comparable, or even less than, when the angular dependence is  $\sin^2(\theta)$ . Figures 46 and 47 include the  $10 \log \mu$  variable ( $10 \log \mu = -35$  and  $-17$ ) factored into the bottom scattering strength angular dependencies of  $\sin(\theta)$  and  $\sin^2(\theta)$ , respectively. These figures show that at very shallow grazing angles the two bottom scattering strength kernels yield bottom scattering strengths within only a few decibels of each other. Figures 49, 50, 51, and 52 also illustrate the similarity of bottom scattering strengths for the two angular dependencies when different values of  $10 \log \mu$  are substituted into the scattering strength equation. Notice that as the difference between the

$10 \log \mu$  values approaches zero, the bottom scattering strength curves increase in similarity over a wider range of grazing angles. Figures 51 and 52 show that for the bottom scattering strength kernels of  $-25 + 10 \log \sin(\theta)$  and  $-17 + 10 \log \sin^2(\theta)$ , the two bottom scattering strength curves are within about 2.5 dB of each other for grazing angles of  $5^\circ$  to  $16^\circ$ . The curves have a crossover point at about  $9^\circ$ . Additionally, as the values of  $10 \log \mu$  in the two bottom scattering strength kernels approach equality, the crossover point for the two curves shifts toward higher grazing angles and the two bottom scattering strength curves show more similarity over a wider range of angles. This implies that selecting the correct angular dependence when curve fitting measured bottom scattering strength data is extremely difficult without detailed geoacoustic models to test the theoretical results. With two free parameters,  $10 \log \mu$  and  $\sin^x(\theta)$ , there are physically meaningless ways to curve fit bottom scattering strength data with "false" accuracy.

Wrong assumptions or assumptions based on little geologic and geoacoustic data can easily lead one to believe the correct bottom

scattering strength kernel has been selected (when it has not been). For example, if TL based on an inaccurate geoacoustic model were underestimated by about 2 dB for grazing angles less than 9° and TL were overestimated by the same amount for grazing angles greater than 9°, the  $-17 + 10 \log \sin^2(\theta)$  curve in Figure 52 could be indistinguishable from the  $-25 + 10 \log \sin(\theta)$  curve. This could easily occur in a range-dependent shallow water environment and re-iterates the necessity of developing accurate geoacoustic models based on detailed geologic surveys when studying bottom scattering strength. The wide-range of  $10 \log \mu$  values applied to sediment types thought to be the same (see McCammon, 1993) is probably due to one or more of the factors discussed above.

Bottom scattering strength and TL are both functions of geology and sediment type. The variability of sediment type (and thus TL) in shallow water is manifested in variability of bottom scattering strength kernels. Hard sand bottoms have bottom scattering kernels that obey Lambert's law while silt-clay bottoms show more volume scattering and do not obey Lambert's law.



## VI. CONCLUSIONS

The current geoacoustic model for Area Foxtrot was found to be inaccurate because the sediment compressional wave speed and density and attenuation values did not conform to the geoacoustic modeling theories given by Hamilton and Bachman (1982). The surface sediments in Area Foxtrot are also much more spatially variable than originally thought. New Hamilton-type geoacoustic models were developed for the area. To calculate RL, the FEPE propagation model was used to augment the GSM propagation model (currently used by NUWC for TL estimation and RL modeling) because the bottom loss model in GSM did not estimate TL accurately in shallow water. The comparison between modeled RL and measured RL (from a 1991 ASW exercise conducted by NUWC) enabled bottom scattering strength kernels to be developed for Area Foxtrot. The conclusions reached in this study are as follows:

- 1) Based on geologic data, it is readily apparent that Area Foxtrot is not a spatially homogeneous, acoustically benign area. The surface sediment was found to range from coarse sand and shell

fragments to silt-clay sediments. Hamilton-type geoacoustic models developed in this study show that compressional wave speeds in Area Foxtrot vary from over 1800 m/s to less than 1600 m/s over ranges of less than 7 km. No one geoacoustic model can describe all of Area Foxtrot.

- 2) The current geoacoustic model for Area Foxtrot is not consistent with either observed geological data or with Hamilton-type geoacoustic modeling theories. The current "sand" bottom model for Area Foxtrot employs a silt-clay compressional sound speed but uses a density and attenuation value consistent with a sand sediment.
- 3) The GSM model does not have a sub-routine to incorporate sub-bottom geoacoustic properties. A second, external TL model must be used to accurately estimate TL in shallow water environments where bottom interaction is of major concern. NUWC currently uses bottom loss curves generated by the SAFARI model to augment GSM. NPS uses FEPE TL estimates to address this problem because FEPE has repeatedly demonstrated an ability to accurately model sub-

bottom refracted energy. Either way, GSM can not model bottom interacting energy accurately without using another TL model.

4) Significant differences were noted in the TL estimates between GSM and SAFARI or FEPE for both the sand and silt-clay geoacoustic models. These differences in turn significantly influenced the shape of the modeled RL curve demonstrating the sensitivity of RL to TL.

5) Because the bottom surface sediments in Area Foxtrot vary from course sand to silt-clay, the bottom scattering strength kernels vary also. The sand bottom was well-modeled using a bottom scattering strength of  $-33 + 10 \log \sin^2(\theta)$  and is consistent with a Lambert's law relationship. The silt-clay bottom demonstrated a bottom scattering strength of  $-35 + 10 \log \sin(\theta)$  and is consistent with the volume scattering mechanism proposed by Jackson and Briggs (1992) and Mourad and Jackson (1993).

6) When the GSM TL model was corrected for bottom loss, i.e., incorporating bottom refraction as modeled by FEPE, the following results were obtained:

a. Excellent agreement was achieved between modeled RL and measured RL for beams steered in the direction of the hard sand bottom using Lambert's law ( $\sin^2(\theta)$  dependence) to characterize the bottom scattering strength.

b. Excellent agreement was achieved between modeled RL and measured RL for beams steered in the direction of the silt-clay bottom using a more "lossy" ( $\sin(\theta)$  dependence) characterization of the bottom scattering strength. This is consistent with volume scattering as described by Jackson and Briggs (1992) and Mourad and Jackson (1993).

c. More than one bottom scattering strength kernel can be used to fit the modeled RL for the same bottom type to the measured RL for very shallow grazing angles (less than  $3^\circ$ ). As the difference in the  $10 \log \mu$  terms approaches zero in two different bottom scattering strength kernels (with angular dependencies of  $\sin(\theta)$  and  $\sin^2(\theta)$ ), the resulting bottom scattering strength curves increase in similarity over a wider range of grazing angles.

7) The performance of the AN/SQS-53C (CW 500 pulse) in shallow water is strongly dependent on the local geology of the bottom in negative (downward) refracting water columns. The RL will fall off more quickly when propagation is over a silt-clay bottom than over a hard sand bottom.

8) The modeling techniques developed in this study can be used to bound RL in active sonar performance in strategic shallow water areas where little is known about the bottom sediment type and its spatial distribution. As shown in the bottom panel of Figure 41, the RL values can be modeled for hard sand and silt-clay sediments based on Hamilton modeling principles and by using the appropriate angular dependence of bottom scattering strength ( $\sin^2(\theta)$  for sand,  $\sin(\theta)$  for silt-clay). Measured RL should then fall between these two extremes for locations where the bottom is sediment covered. A method can easily be developed in which measured RL from a few pings emitted in the area of interest could be used to deduce the azimuthal dependence of RL. By knowing the azimuthal dependence

of RL in the local area, the bottom sediment type can be deduced and more accurate detection ranges can be determined.

9) Bottom scattering strength is a function of grazing angle, Mackenzie's constant, and TL. The TL must be accurately modeled to deduce the bottom scattering strength especially at low grazing angles for which volume reverberation within the sediment layer is important. Incorrect bottom scattering strength kernels can easily be deduced from curve fitting to measured data. This occurs because various combinations of Mackenzie's constant ( $10 \log \mu$ ), first or second power angular dependence ( $\sin(\theta)$  or  $\sin^2(\theta)$ ), and TL trends (due to propagation over different bottom sediments) can produce very similar RL curves.

## VII. RECOMMENDATIONS

The 1992 Navy and Marine Corps White Paper "...From the Sea" authored by the Secretary of the Navy, the Chief of Naval Operations, and the Commandant of the Marine Corps (O'Keefe et al., 1992) states "the shift in strategic landscape means Naval Forces will concentrate on littoral warfare and maneuver from the sea." Maneuvering from the sea "provides a potent war-fighting tool to the Joint Task Force Commander--a tool that is literally the key to success in many likely contingency scenarios."

The following recommendations derived from the results of this thesis are provided in support of the war-fighting concepts envisioned in "...From the Sea." These recommendations are designed to improve the accuracy of performance prediction of current and emerging active sonar systems and put forth ideas for the tactical applications of this thesis.

### A. RECOMMENDATIONS REGARDING AREA FOXTROT

- 1) If NUWC or the Navy plan to use Area Foxtrot as a sonar test bed for active sonar systems, then it is strongly recommended to

conduct a detailed geologic study of at least two 15 km by 15 km sections of Area Foxtrot. One section should have a predominantly hard sand bottom while the other has a silt-clay bottom. The geologic study must include surface sediment samples, sediment cores, and bathymetry. The resolution of the geologic survey will determine the accuracy of any resulting geoacoustic models.

- 2) Construct Hamilton-type geoacoustic models for the sand and silt-clay bottom areas and use these models to improve the accuracy of performance prediction of Navy active sonars in Area Foxtrot.

**B. RECOMMENDATION REGARDING BOTTOM SCATTERING STRENGTH**

- 1) Use a bottom scattering strength kernel with angular dependence of  $\sin^2(\theta)$  for hard sand sediment type bottoms and  $\sin(\theta)$  for silt-clay sediment bottoms. Mackenzie's constant ( $10 \log \mu$ ) is variable in both sand and silt-clay sediments and should be determined by curve fitting modeled RL to measured RL while applying the appropriate angular dependence for the sediment type.

### **C. RECOMMENDATION REGARDING GSM**

1) Integrate FEPE into the GSM model for estimating TL. Since FEPE can take several hours to run, it is not recommended for tactical operational use. For tactical applications, a database of FEPE TL curves can be calculated in the laboratory now for shallow water environments of interest (or potential conflict) based on Hamilton geoacoustic models developed for these areas. The TL curves can be maintained in a library within GSM and accessed by latitude, longitude and ship's heading. This would permit a shipboard METOC (Meteorology / Oceanography) officer to get a first-cut estimate of TL and RL in the operating area based on full Hamilton geoacoustic models. Recall that FEPE is range-dependent so TL curves (and hence RL curves) can be calculated as range-dependent. Development of geoacoustic models by the METOC officer is not recommended.

### **D. RECOMMENDATION REGARDING THE TACTICAL APPLICATION OF THIS THESIS**

1) Develop the method suggested in this study where a few (nominally 12) on-site RL curves can be used to deduce the gross bottom sediment type in an operating area based on the measured RL

curve shapes (see the flow chart in Figure 53). Information on sediment type can be input to GSM to make the laboratory-developed geoacoustic model more accurate. This would certainly improve the accuracy of GSM TL and RL estimates and in turn provide more accurate range predictions in tactical environments where little is known about the local geoacoustic environment.

## **VIII. APPENDIX. FIGURES**



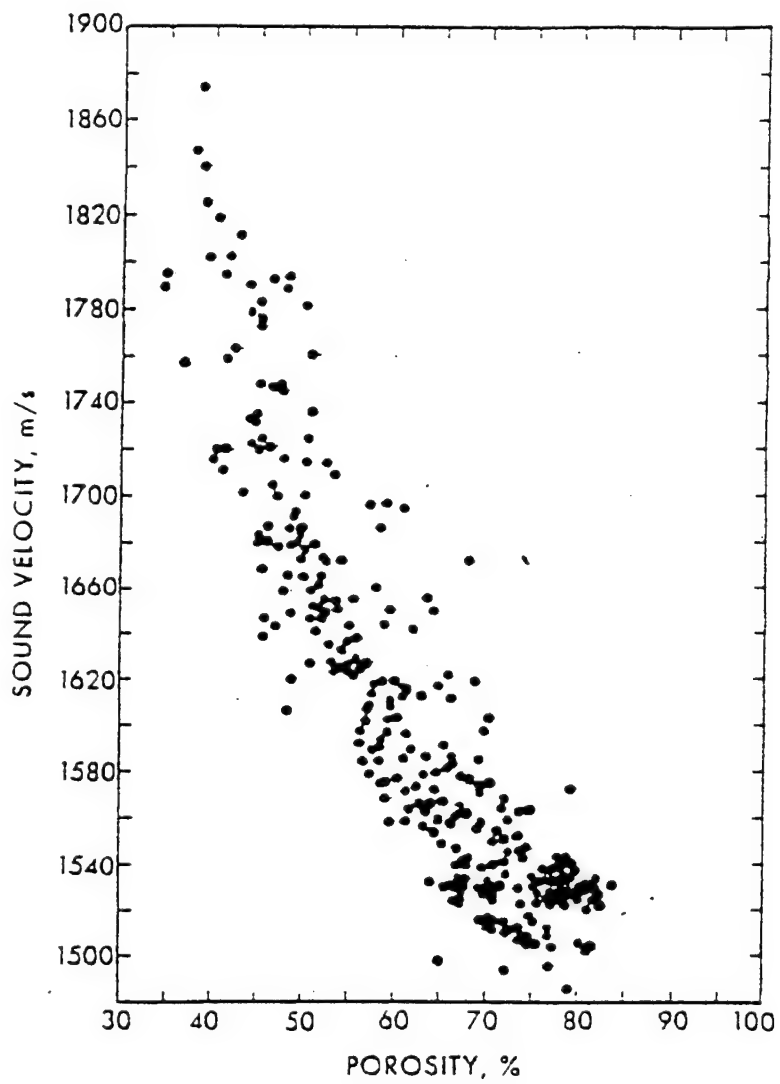


Figure 1. Porosity versus compressional wave speed in samples from the continental terrace (from Hamilton and Bachman, 1982).

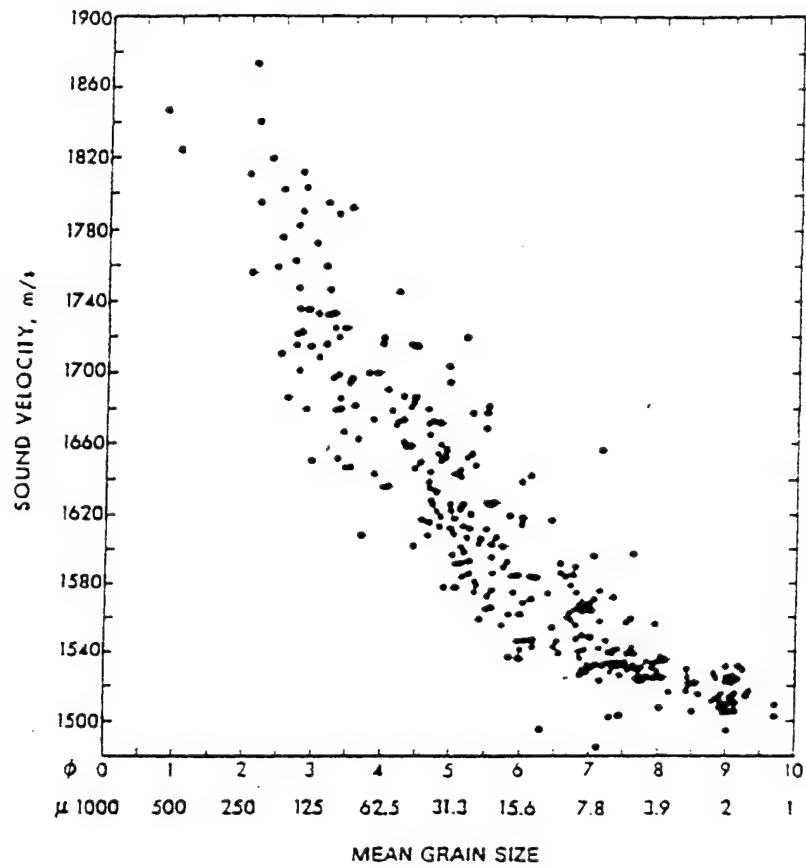


Figure 2. Mean grain size versus compressional wave speed in samples from the continental terrace (from Hamilton and Bachman, 1982).

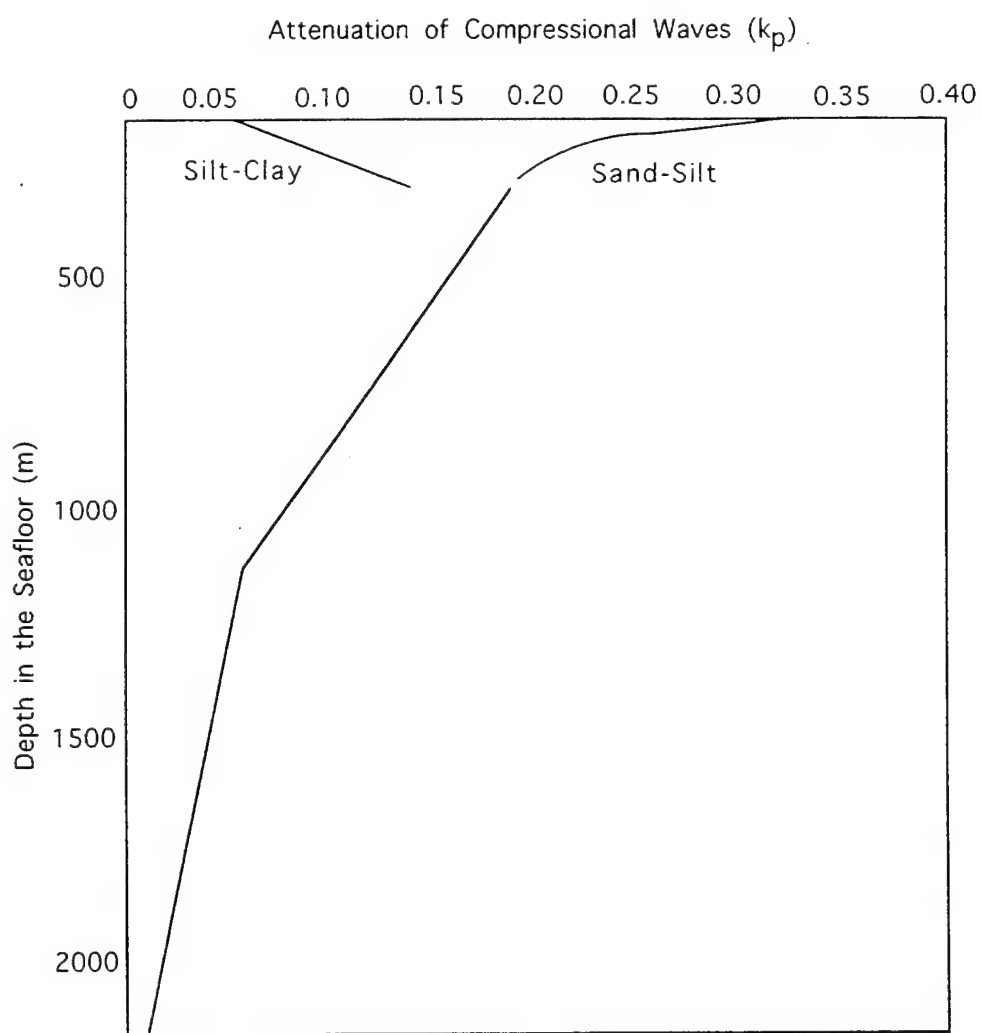


Figure 3. Compressional wave attenuation versus depth for sand and silt-clay sediments on the continental terrace (from Hamilton, 1980).

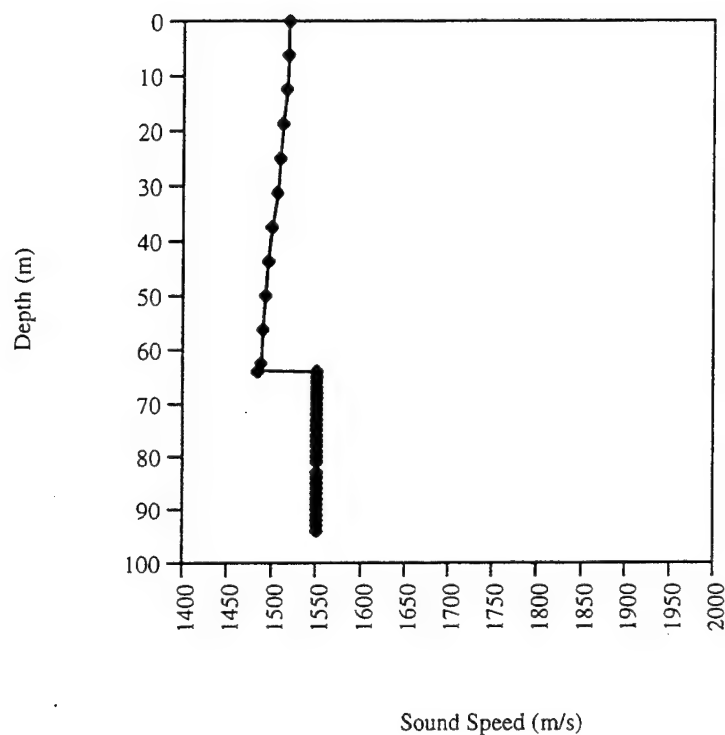


Figure 4. Compressional wave speed versus depth from the water surface to the bottom of the sediment layer - the current geoacoustic model.

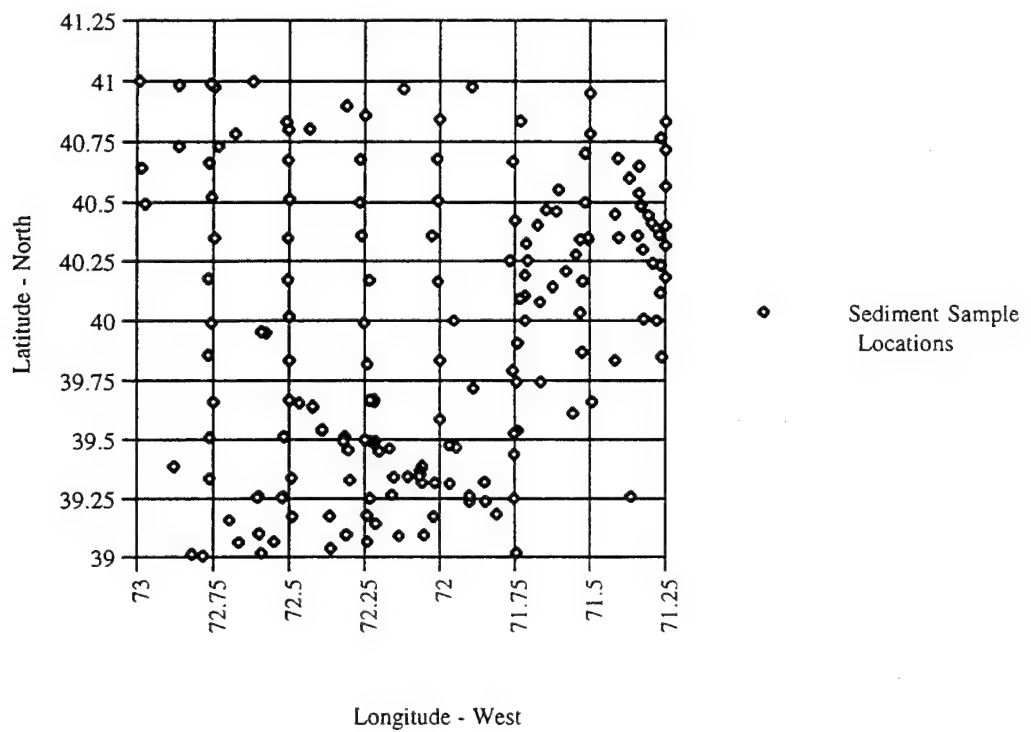


Figure 5. Locations of sediment samples taken in Area Foxtrot.

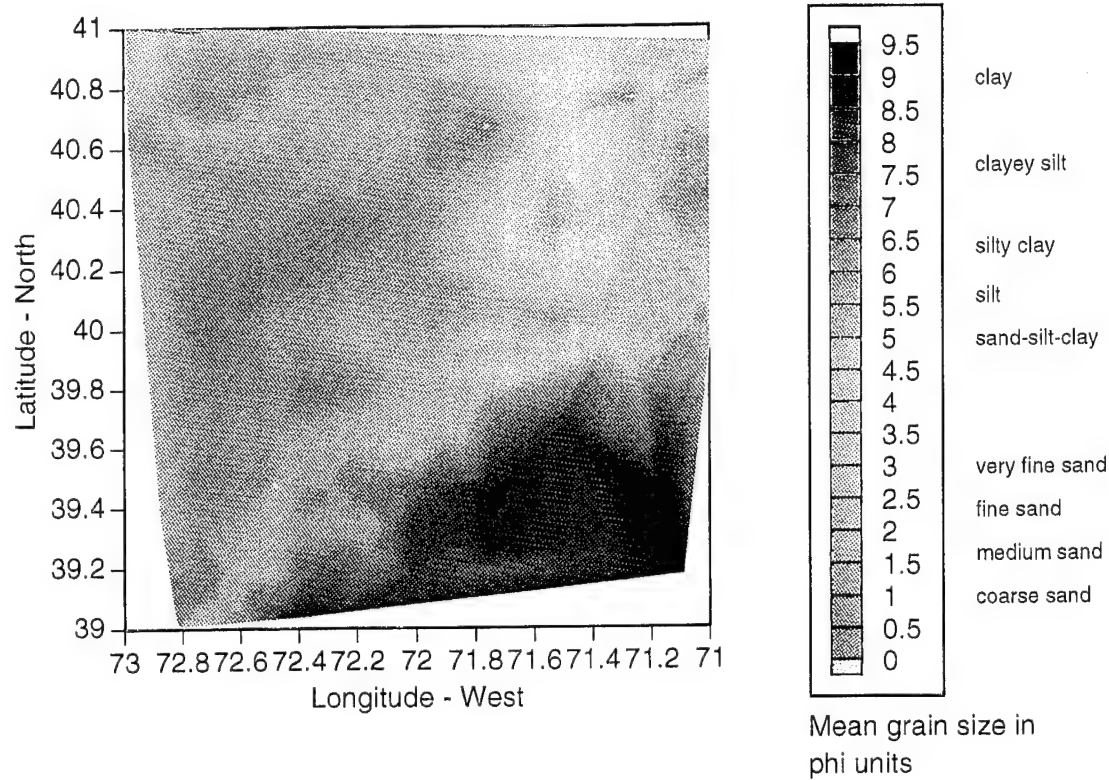


Figure 6. Contour plot of surface sediment mean grain size (phi units) in Area Foxtrot.

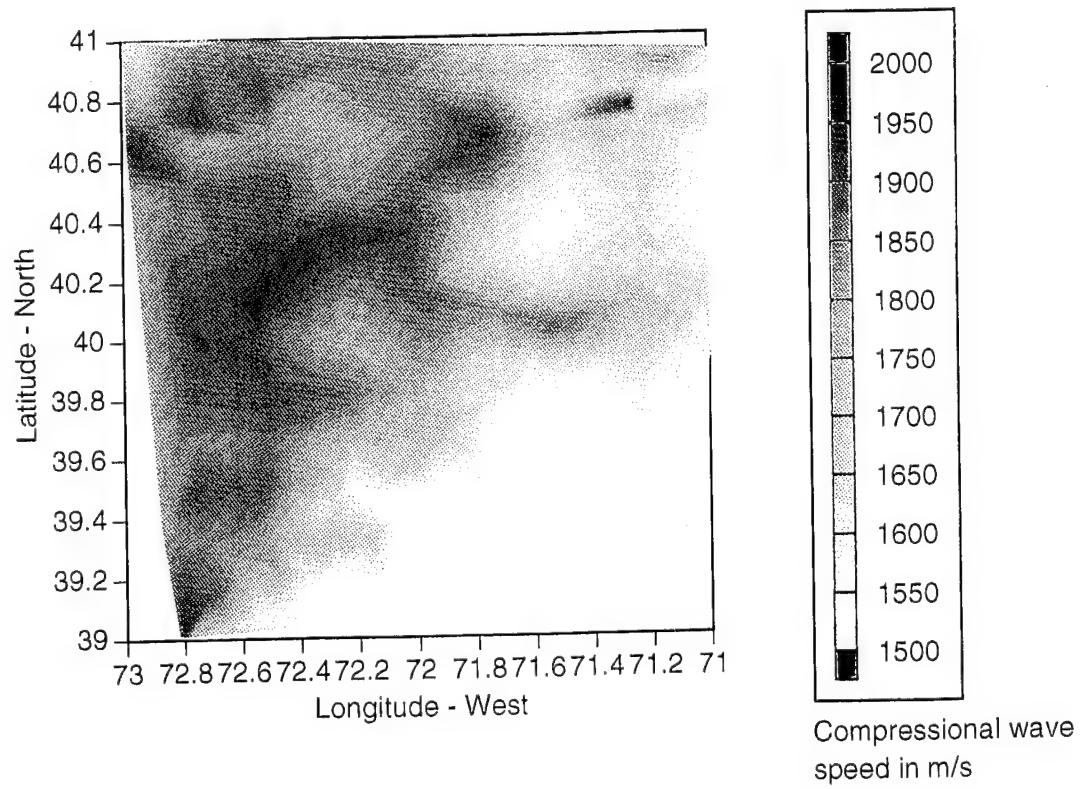


Figure 7. Contour plot of compressional wave speed calculated from Hamilton and Bachman's (1982) regression equation. No correction is made for geology or standard error in the calculation.

Approximate location and track of the surface ship.

Approximate location and track of the target.

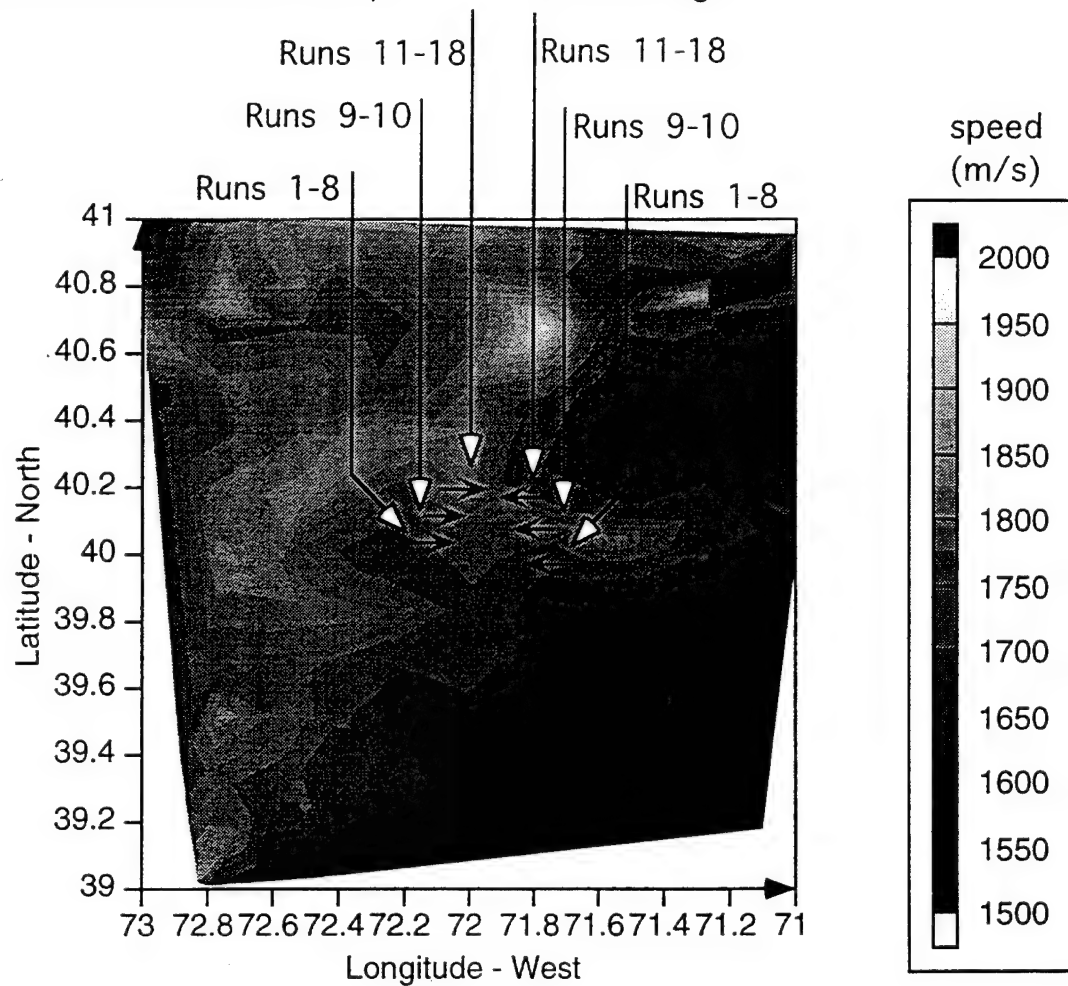


Figure 8. Same as Figure 7 with the approximate locations and tracks of the surface ship and target submarine for the 3-13 September 1991 shallow water ASW test overlain.

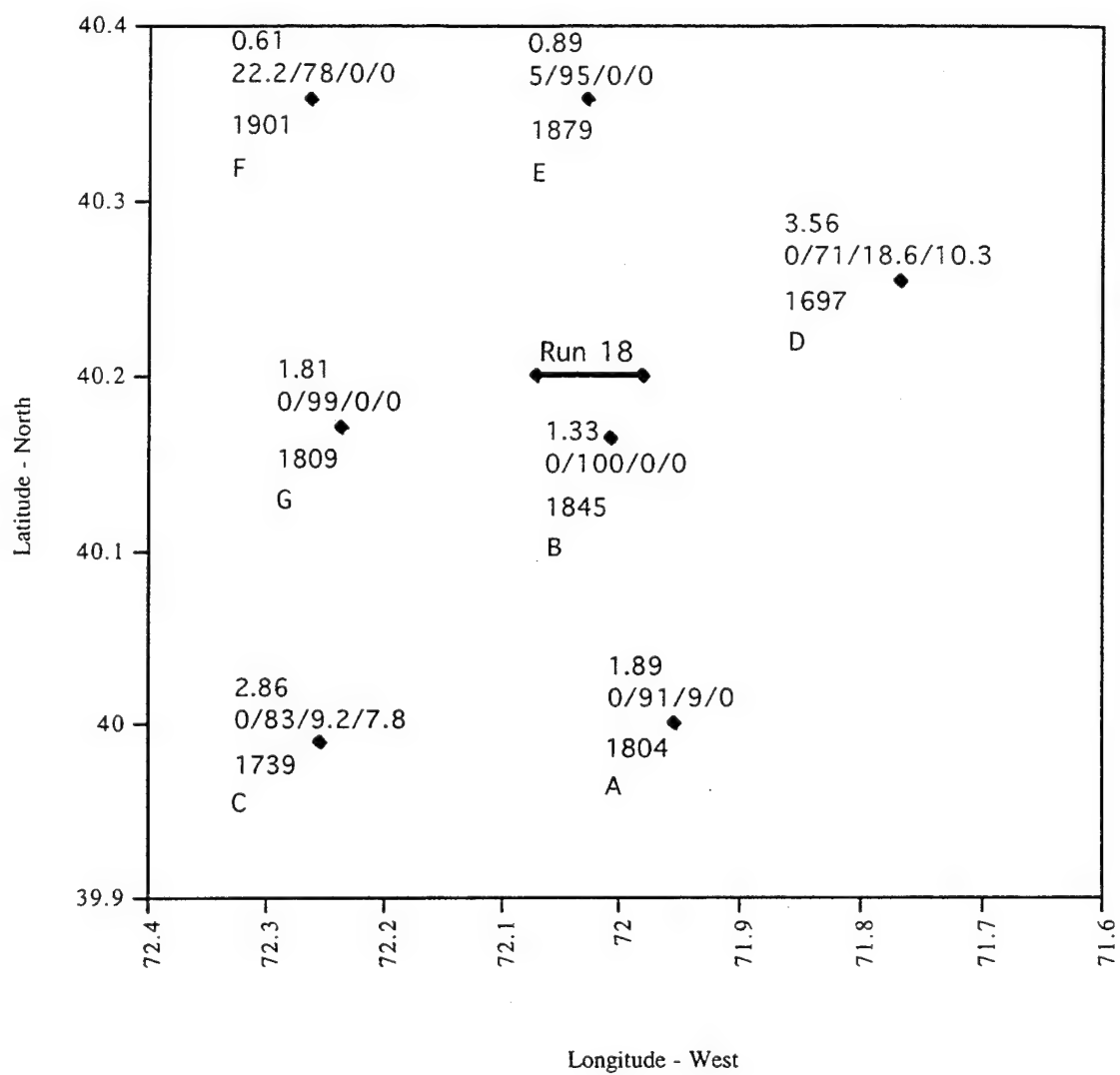


Figure 9. Surface sediment parameters surrounding the Run 18 area. Black diamonds represent the location of a sediment sample.

Legend, for each location:

- mean grain size in phi units
- grain constituents in % as gravel/sand/silt/clay
- compressional wave speed in m/s
- lithology code:
  - A - Green silty sand and shells
  - B - Coarse, brown well-sorted sand
  - C - Green silty sand and shell debris
  - D - Green silt and shell fragments
  - E - Brown to greyish medium to coarse sand
  - F - Coarse brown sand
  - G - Brownish-green very sandy clay

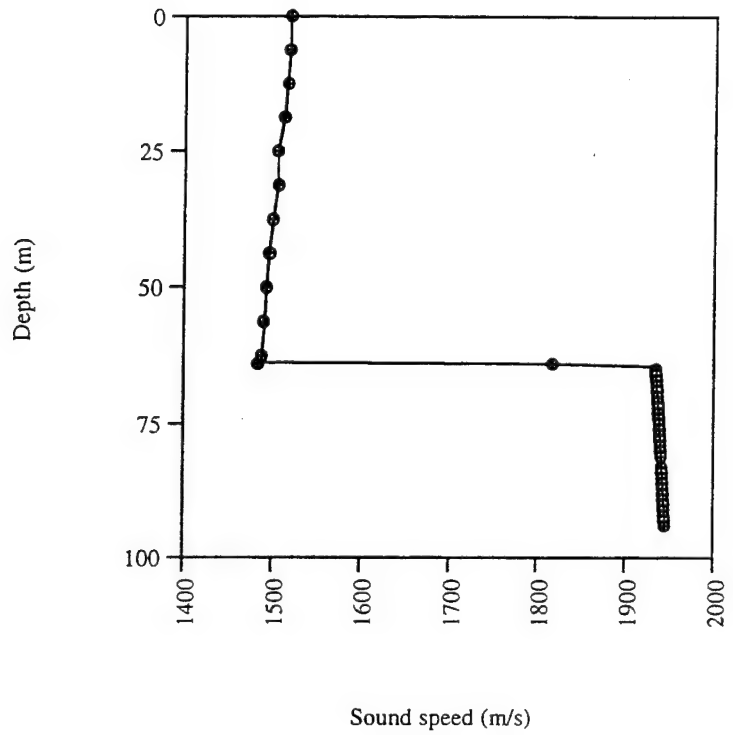


Figure 10. Compressional wave speed versus depth from the water surface to the bottom of the sediment layer - NPS geoacoustic model.

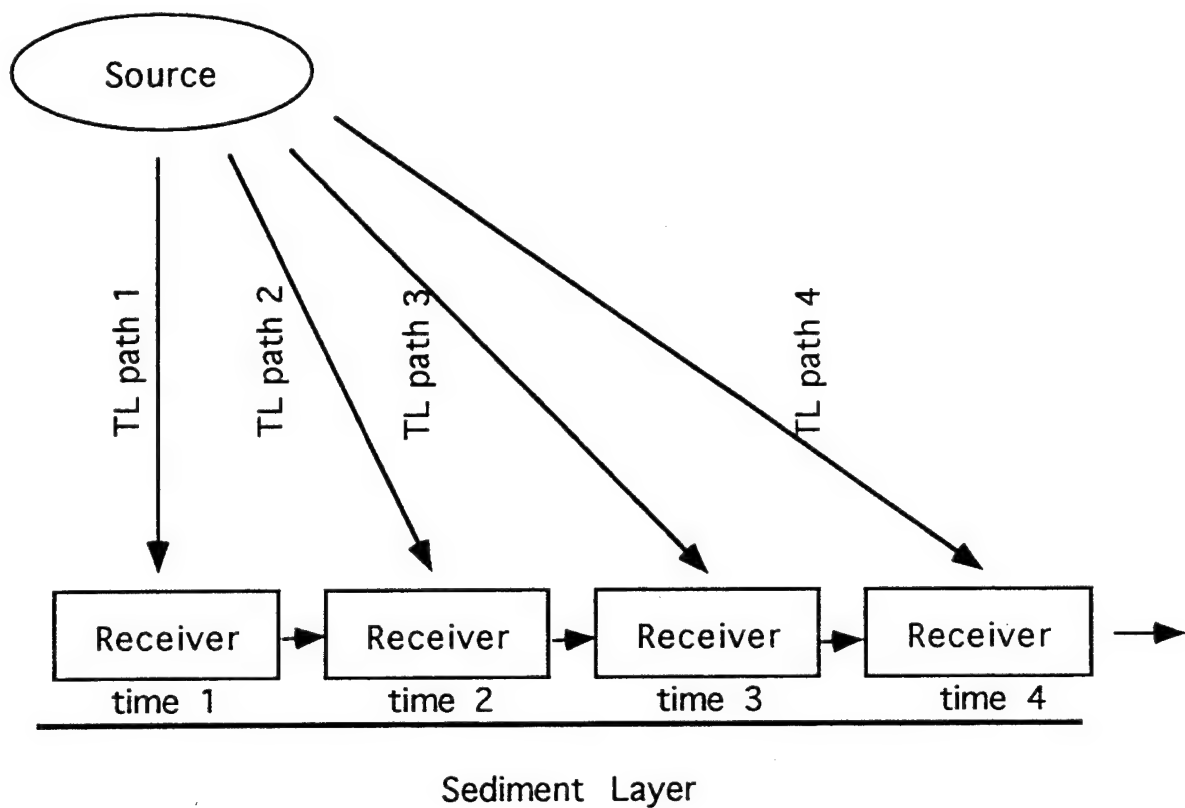


Figure 11. To calculate bottom reverberation TL was calculated from the source to the ocean bottom as the receiver on the bottom was moved out in range.

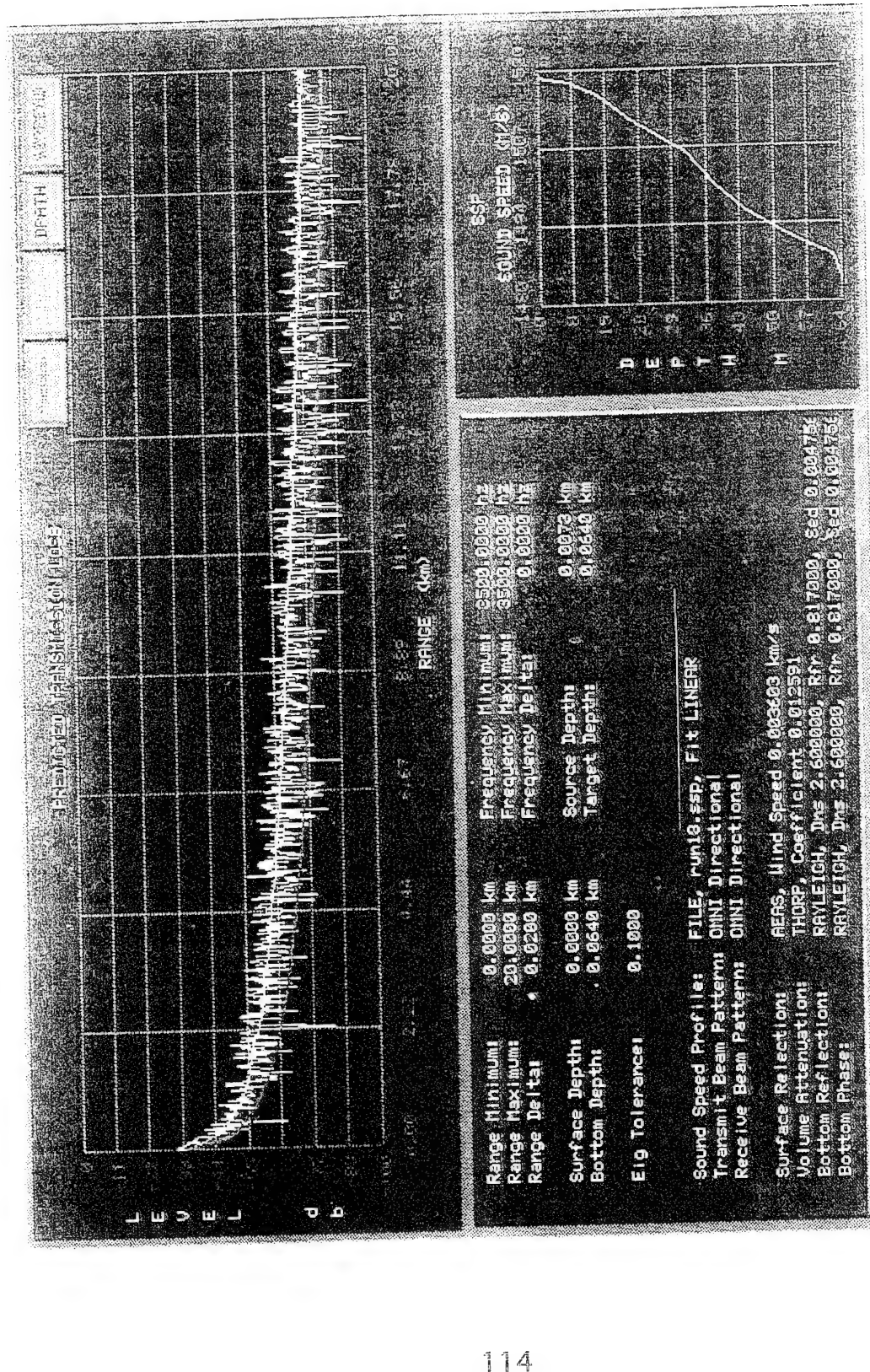


Figure 12. A plot of TL from the GSM/MPE model using the NPS sand bottom model as input. The yellow line is random (incoherent) TL, the white line is phased (coherent) TL, the blue line represents spherical spreading, and the red line is direct path TL. The eigenray tolerance is 0.1. The sediment attenuation in the plot legend is in nepers/wave.

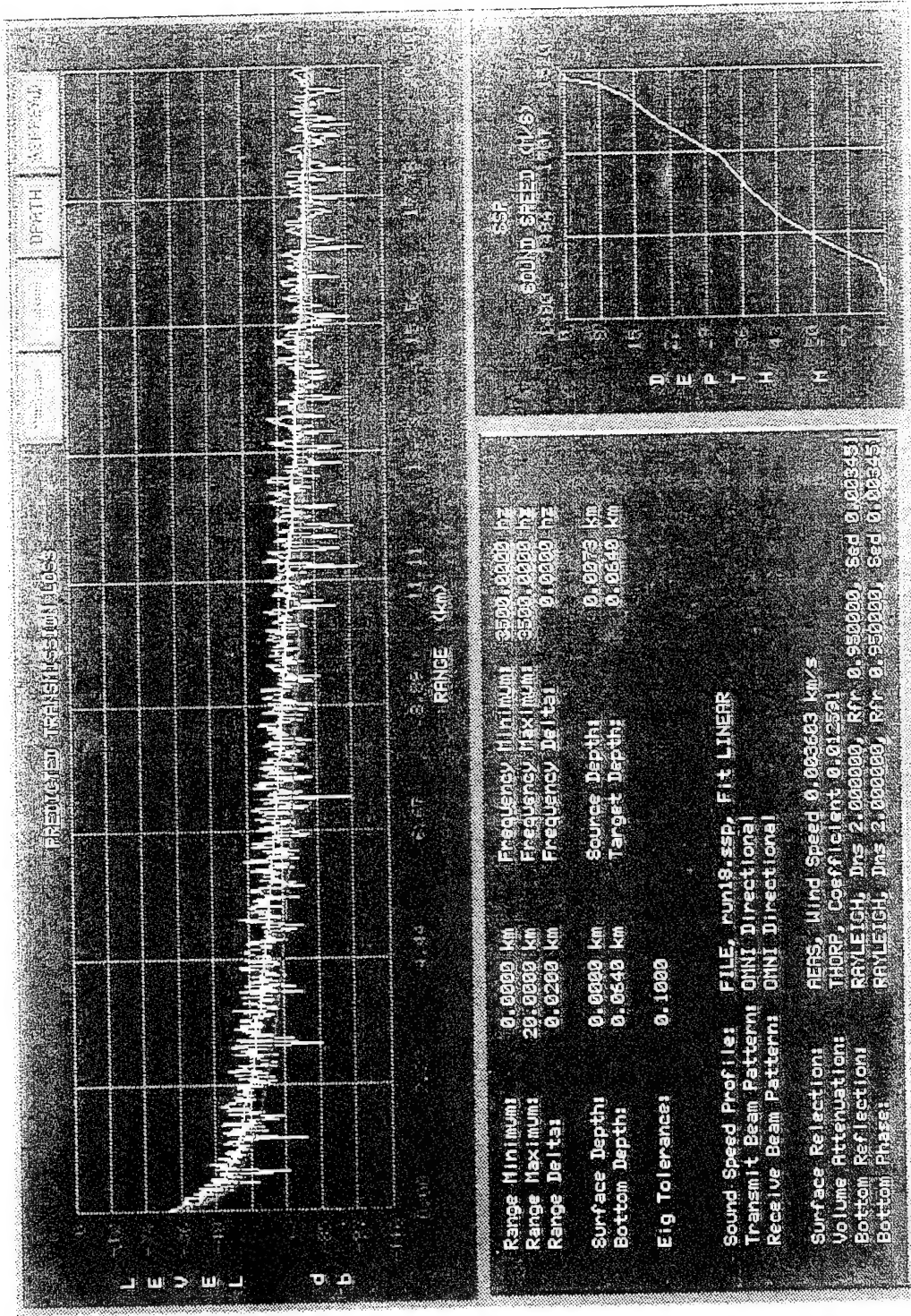


Figure 13. A plot of TL from the GSM/MPE model using the current bottom model as input. The yellow line is random (incoherent) TL, the white line is phased (coherent) TL, the blue line represents spherical spreading, and the red line is direct path TL. The eigenray tolerance is 0.1. The sediment attenuation in the plot legend is in nepers/wave.

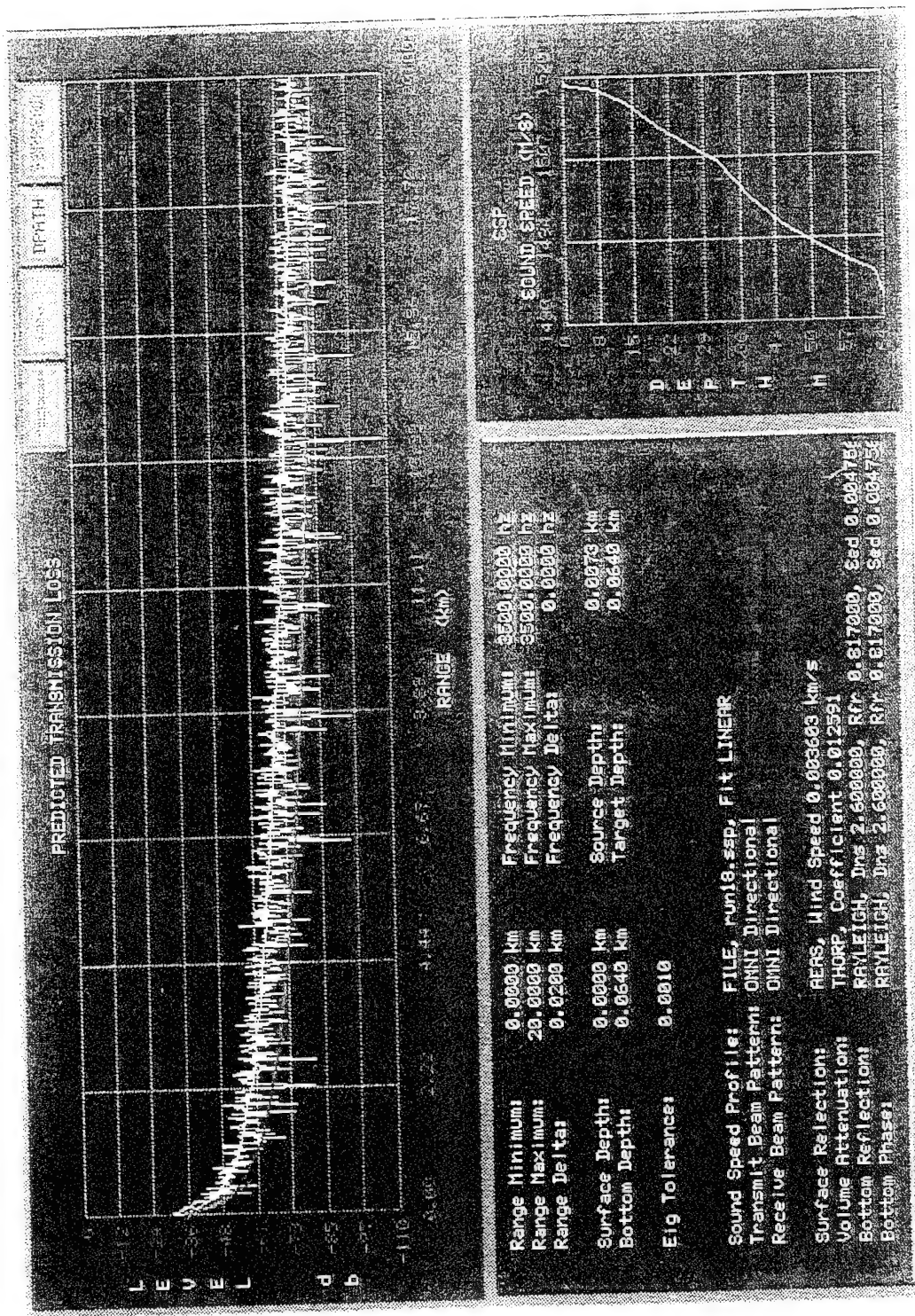


Figure 14. Same as Figure 12 except the eigenray tolerance is 0.001.

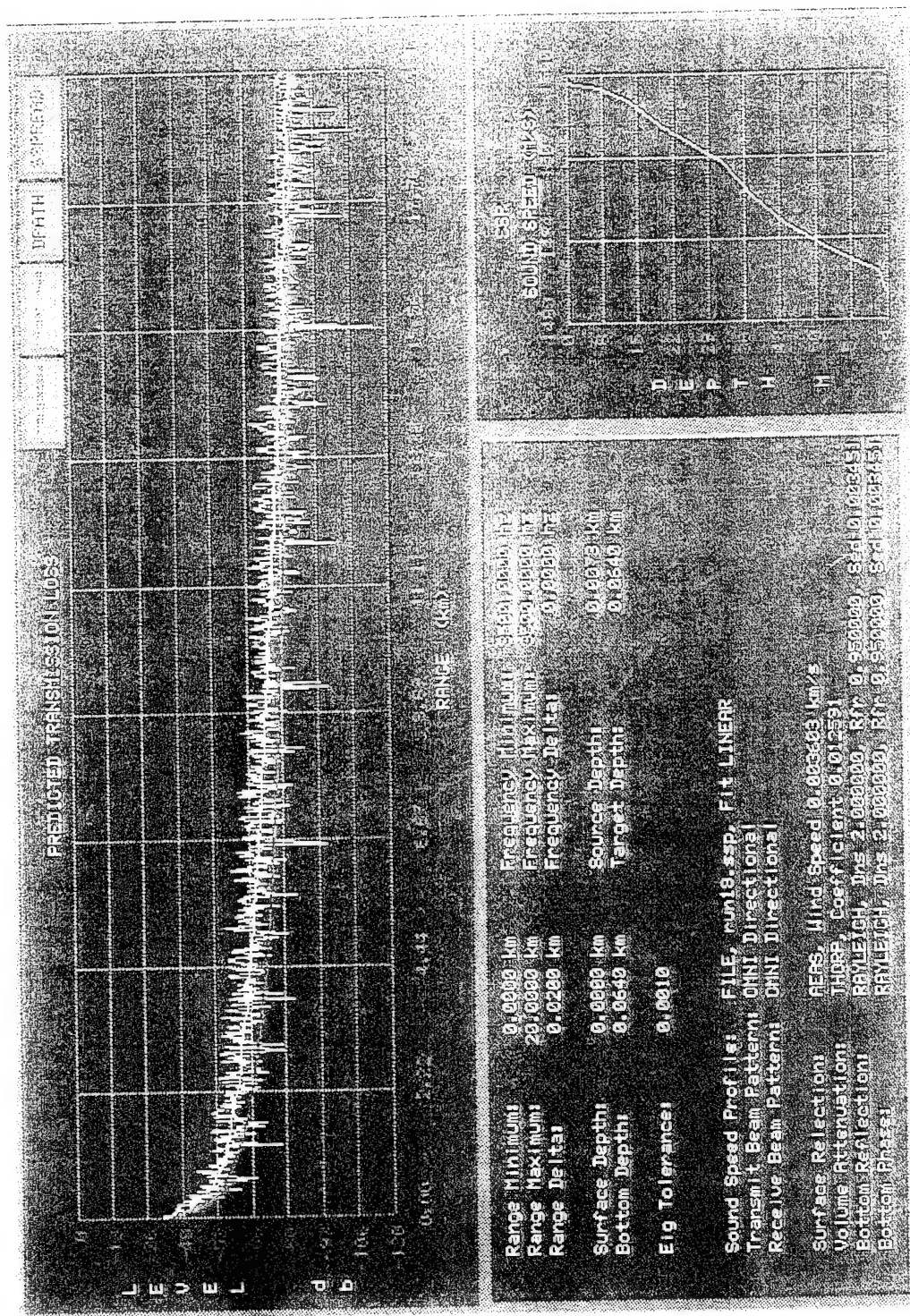


Figure 15. Same as Figure 13 except the eigenray tolerance is 0.001.

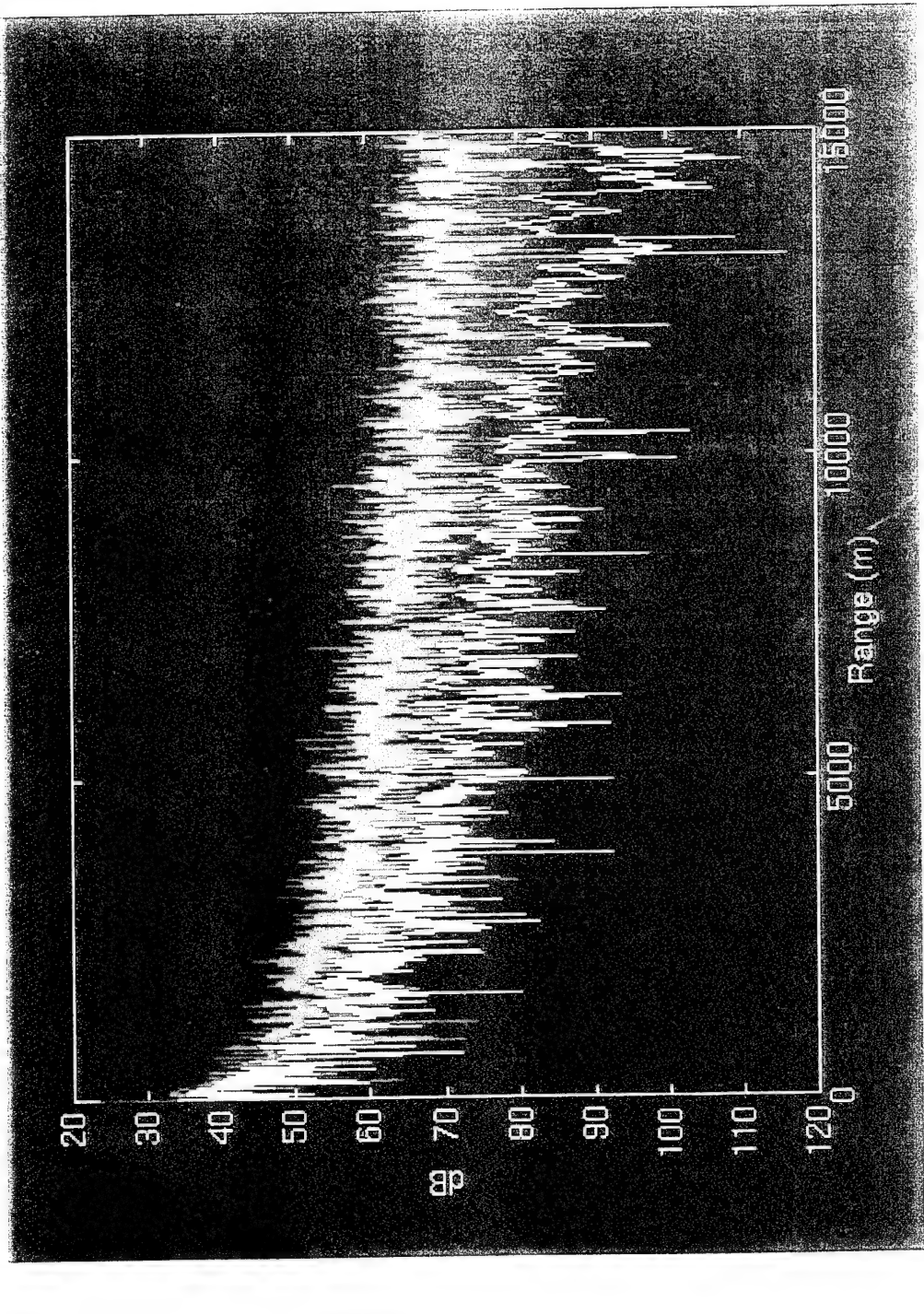


Figure 16. Propagation loss using the FFEPE TL model for the NPS sand bottom model (red curve) and the current bottom model (yellow curve). The source is at 7.3 m and the receiver is at 64 m (on the bottom).

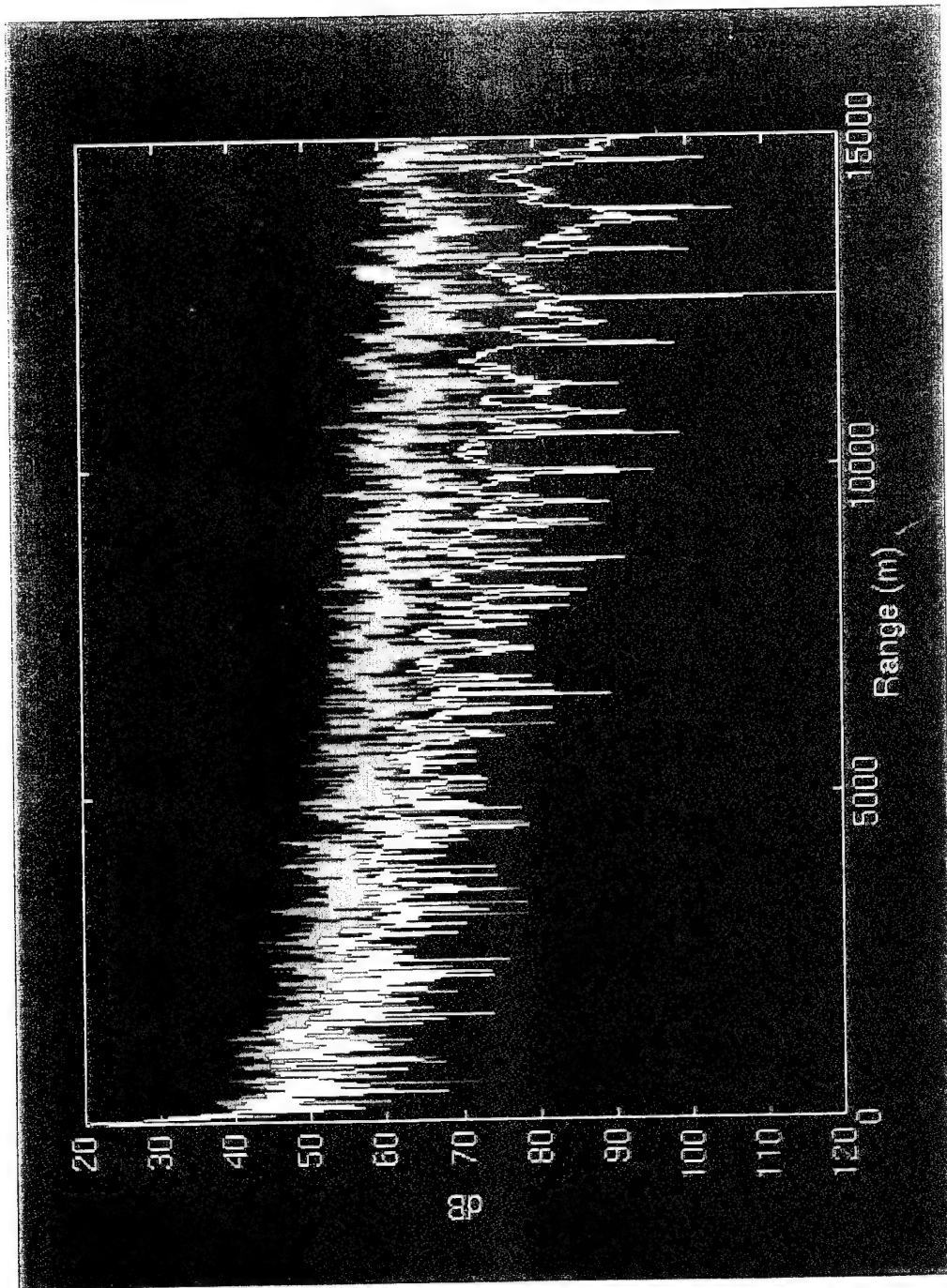


Figure 17. Same as Figure 16 except the source and receiver are both at  
7.3 m.

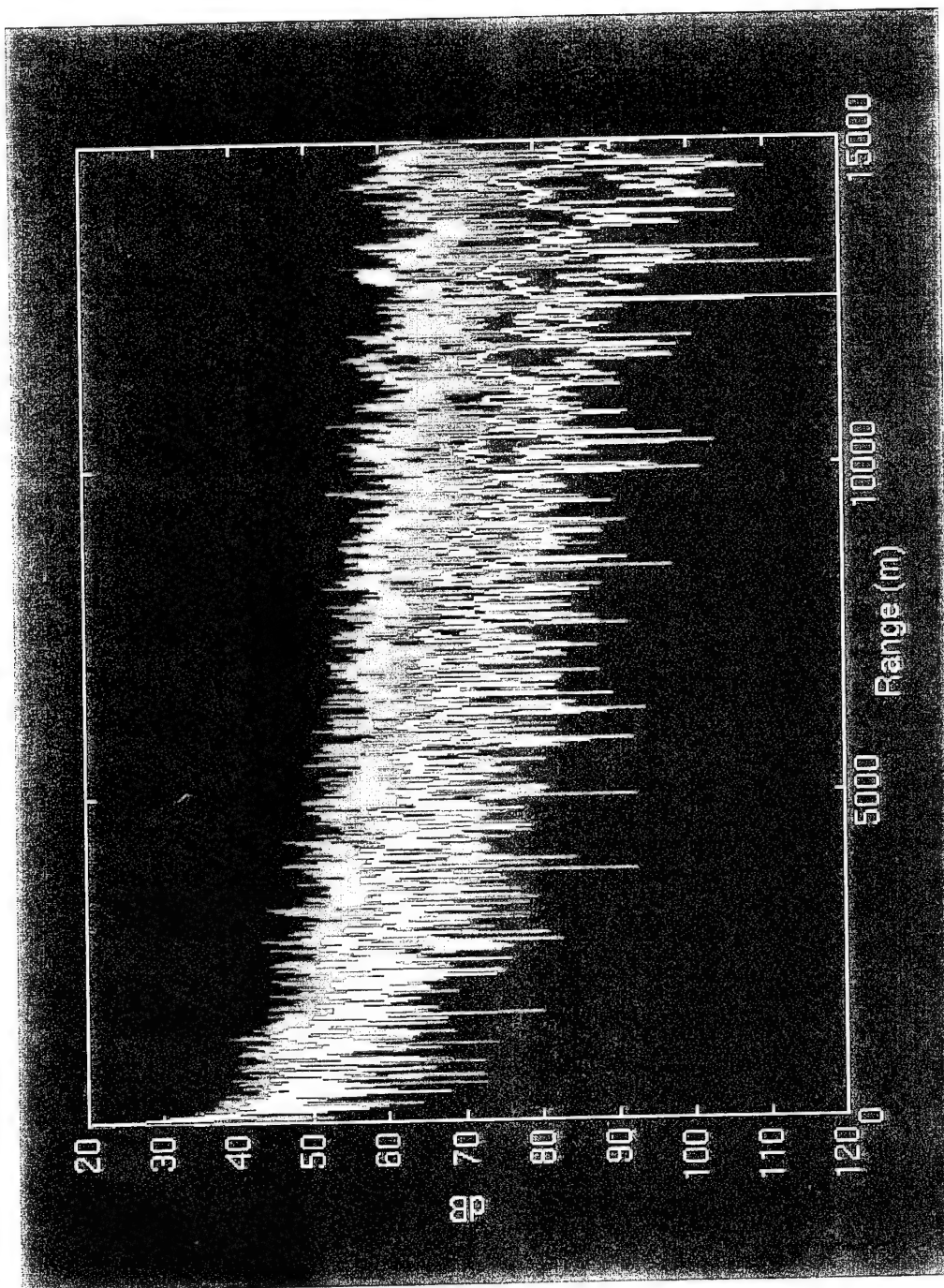


Figure 18. Combination of Figures 16 and 17; NPS sand model with the source and receiver both at 7.3 m (red curve), NPS sand model with the source at 7.3 m and the receiver at 64 m (green curve), the current bottom model with the source and receiver both at 7.3 m (yellow curve), and the current bottom model with the source at 7.3 m and the receiver at 64 m (blue curve).

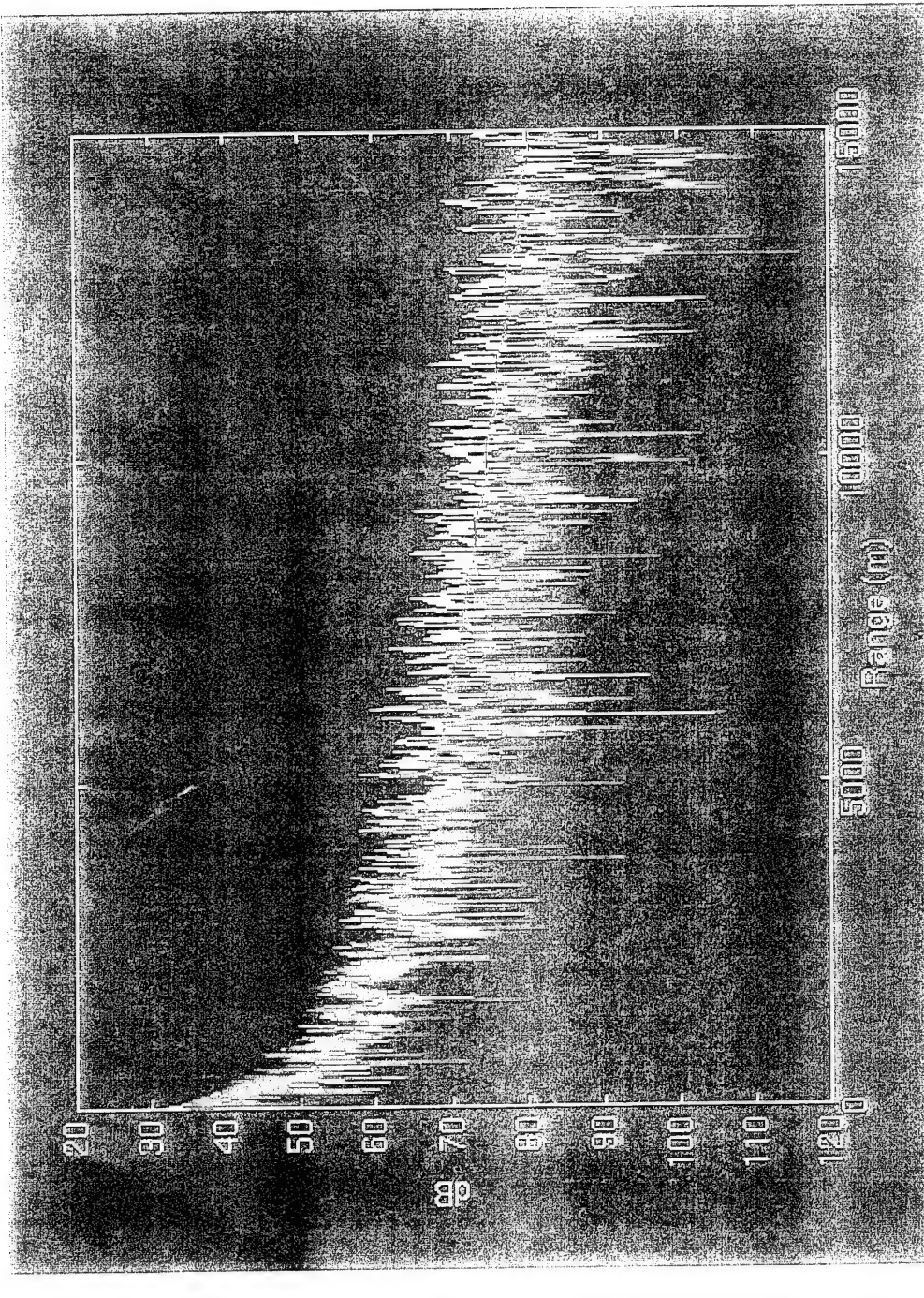


Figure 19. Comparison between the GSM/MPE TL model (the yellow curve is phased TL, the blue curve is random TL) and the FEPE TL model (red curve) using the current geoacoustic model as input. This illustrates that GSM/MPE underestimates the propagation loss compared to the FEPE. GSM/MPE uses the Rayleigh reflection coefficient for bottom loss. FEPE includes a full Hamilton-type geoacoustic model for TL estimation.

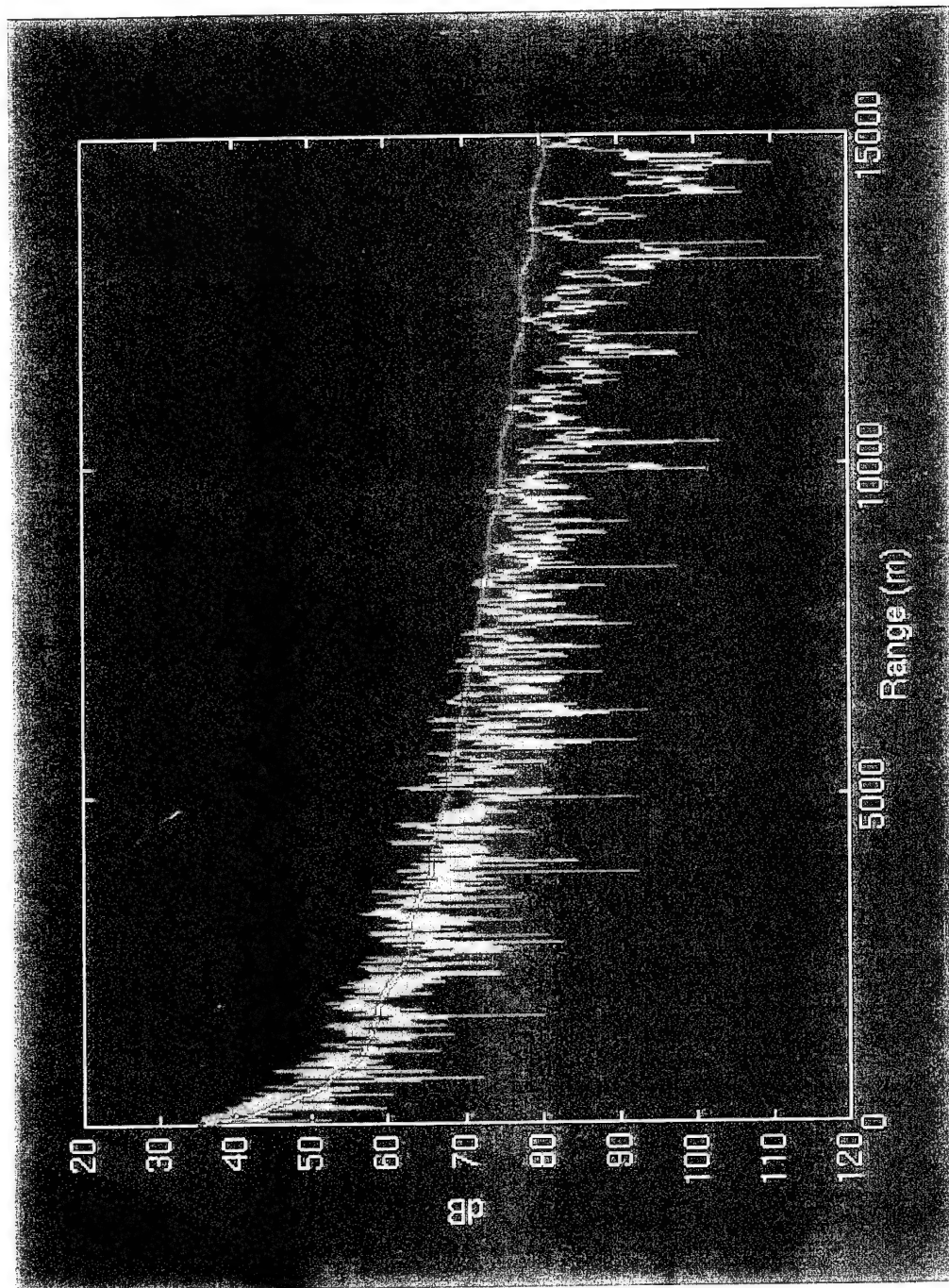


Figure 20. Same as Figure 19 except GSM/MPE phased TL is not included.

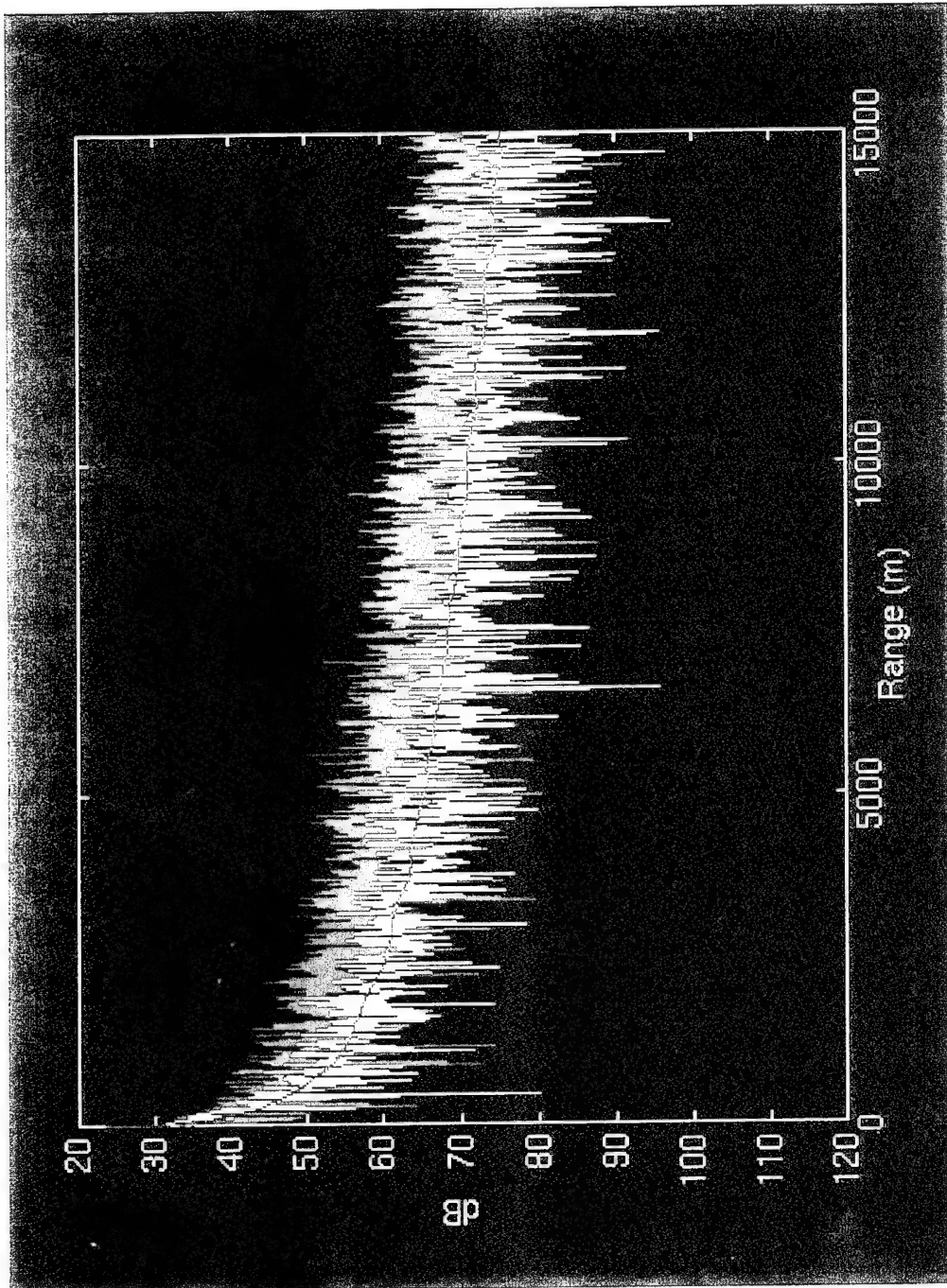


Figure 21. Comparison between the GSM/MPE TL model (the yellow curve is phased TL, the blue curve is random TL) and the FEPE TL model (red curve) using the NPS sand model as input. This illustrates that GSM/MPE overestimates the propagation loss compared to the FEPE. GSM/MPE uses the Rayleigh reflection coefficient for bottom loss. FEPE includes a full Hamilton-type geoacoustic model for TL estimation.

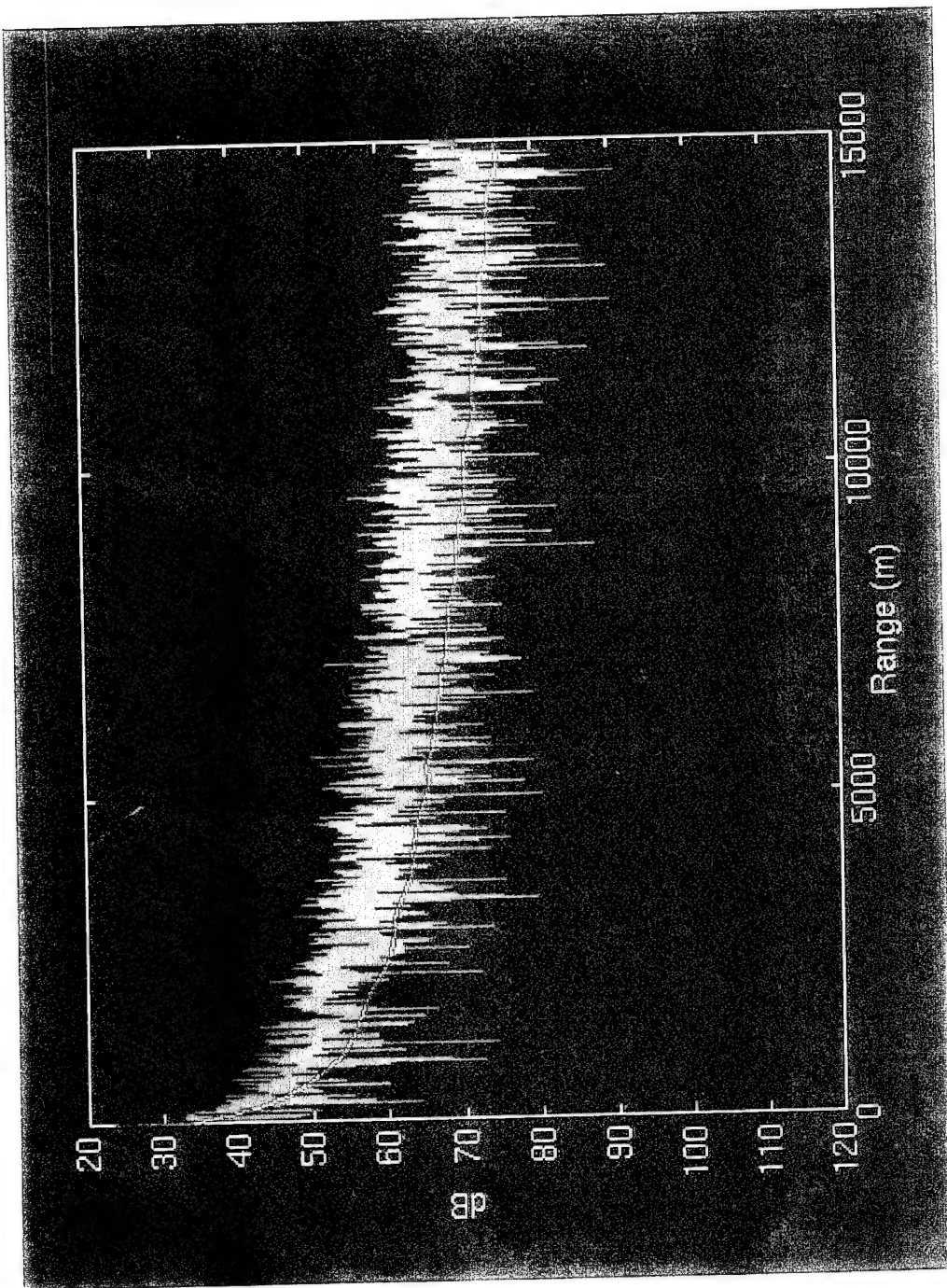


Figure 22. Same as Figure 21 except GSM/MPE phased TL is not included.

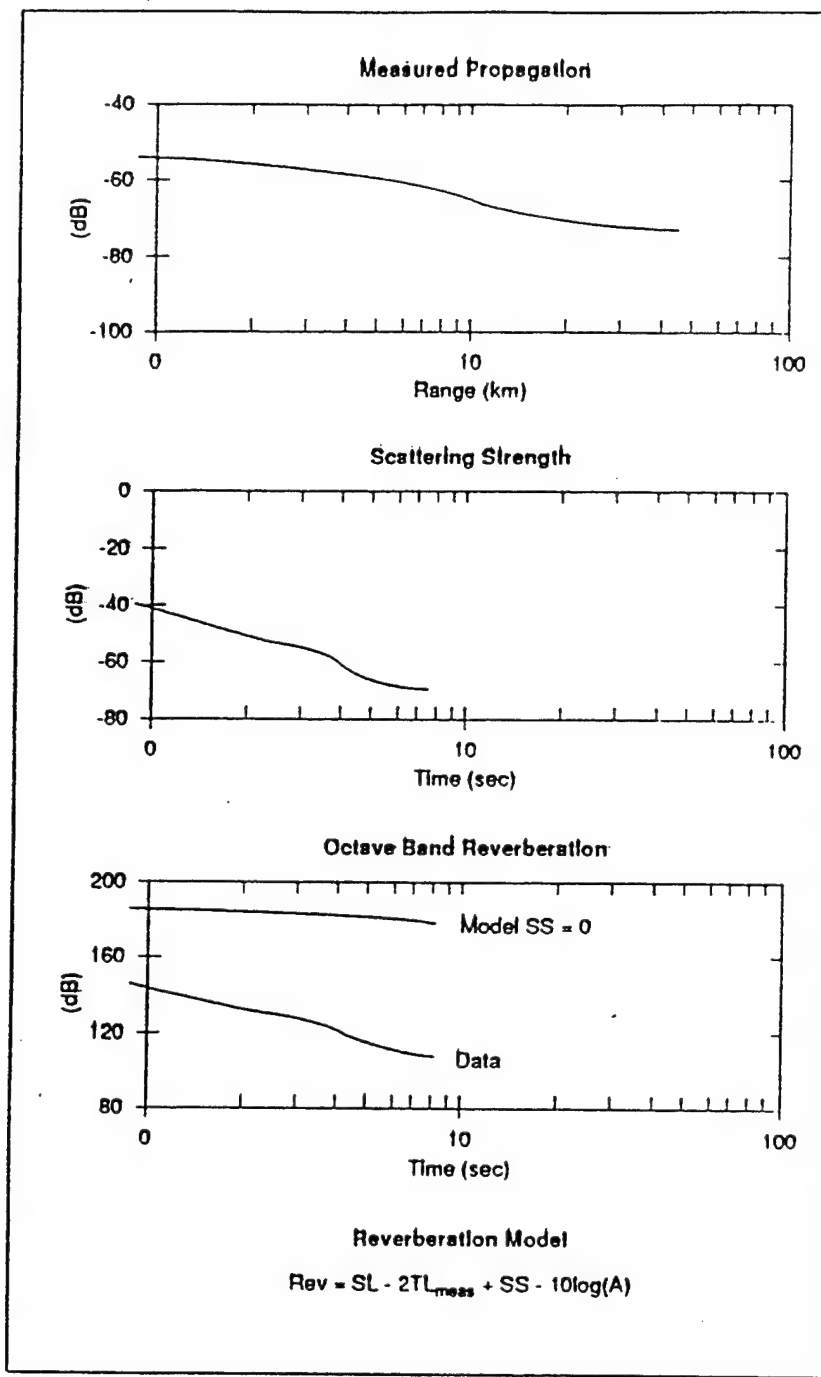


Figure 23. Derived backscattering strength at 100 Hz  
(from Hanna et al., 1994).

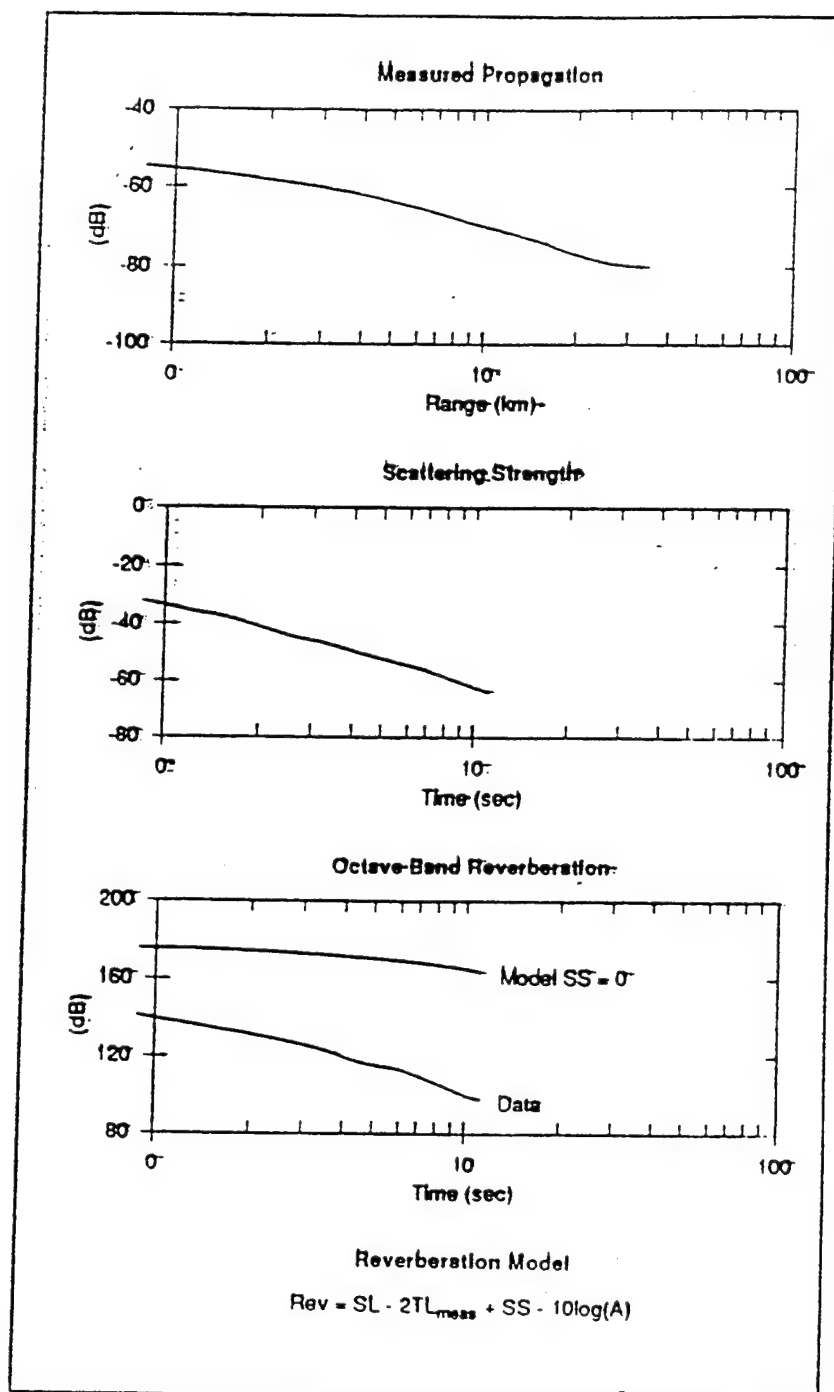


Figure 24. Derived backscattering strength at 800 Hz (from Hanna et al., 1994).

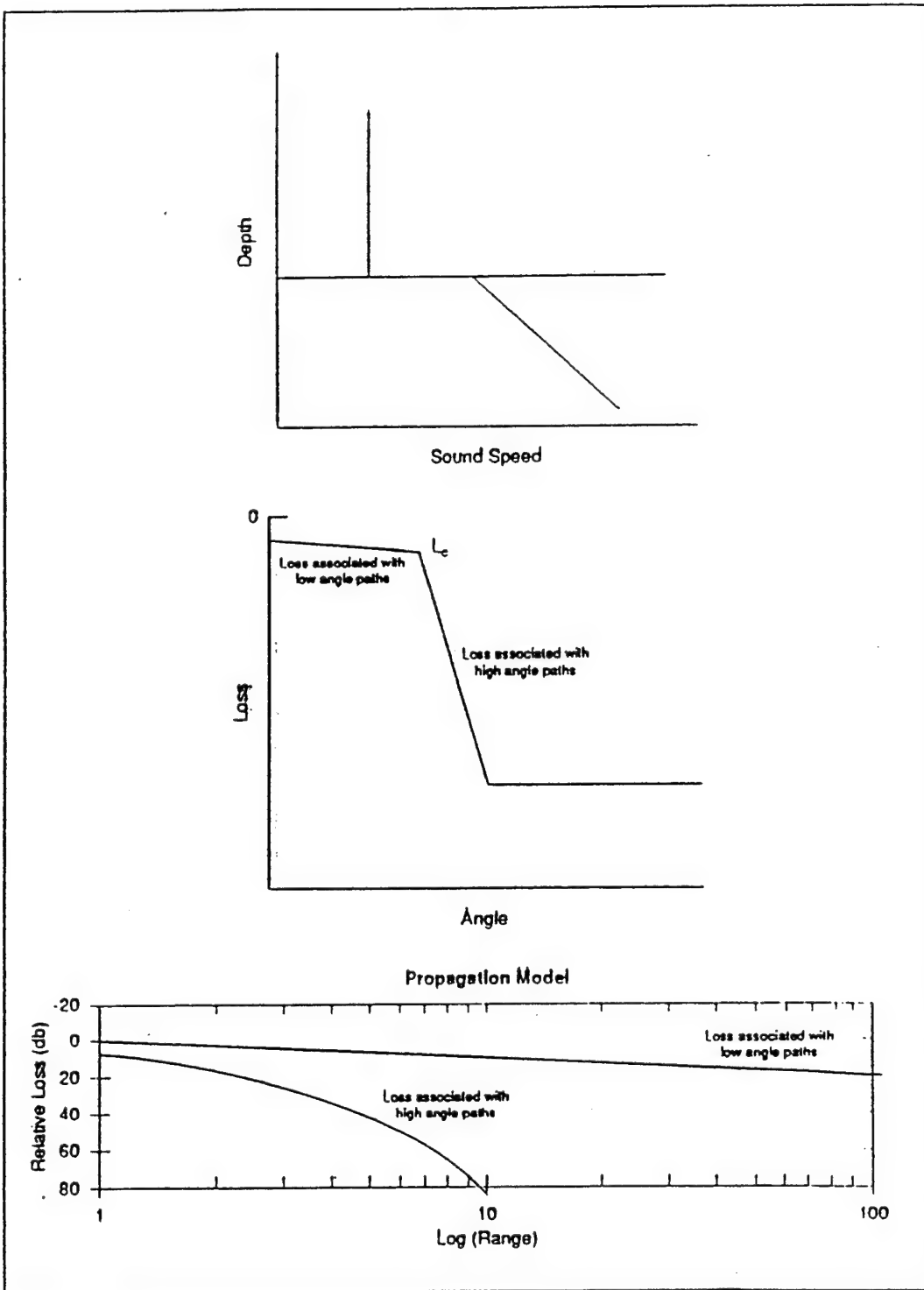


Figure 25. Relative loss associated with low grazing angle paths and high grazing angle paths (from Hanna et al., 1994).

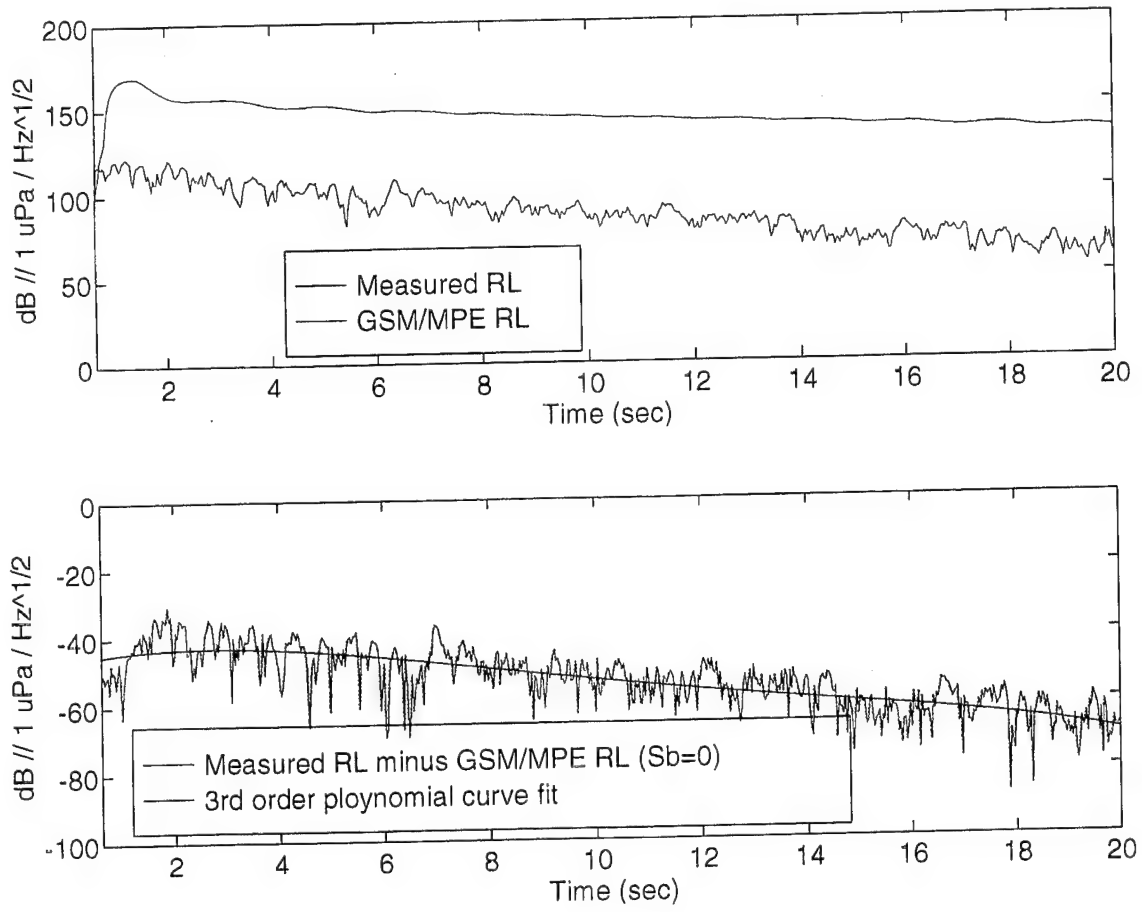


Figure 26. Measured RL and GSM/MPE RL with  $S_b$  set to zero for ping 2, beam 1 (top panel). Measured RL minus GSM/MPE RL with a 3rd-order polynomial cure fit (bottom panel).

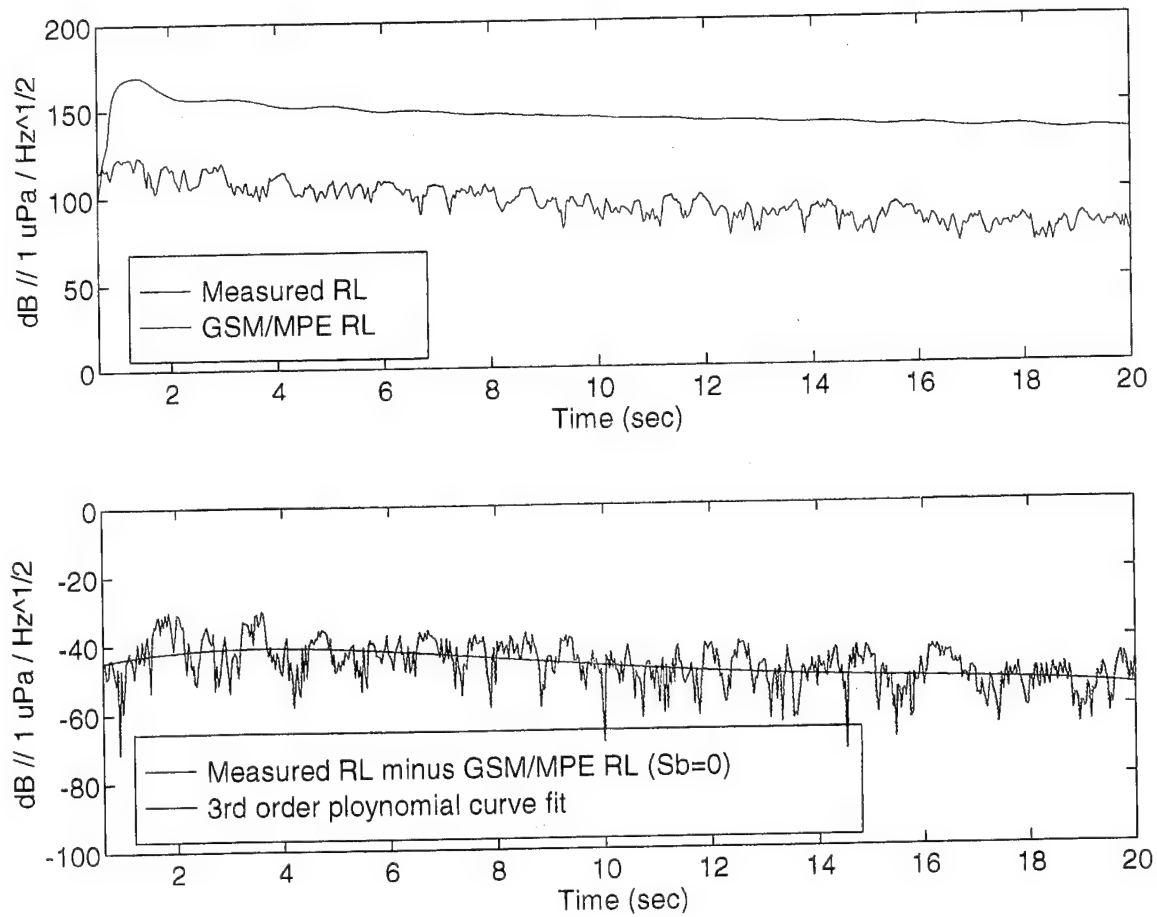


Figure 27. Measured RL and GSM/MPE RL with  $S_b$  set to zero for ping 2, beam 12 (top panel). Measured RL minus GSM/MPE RL with a 3rd-order polynomial cure fit (bottom panel).

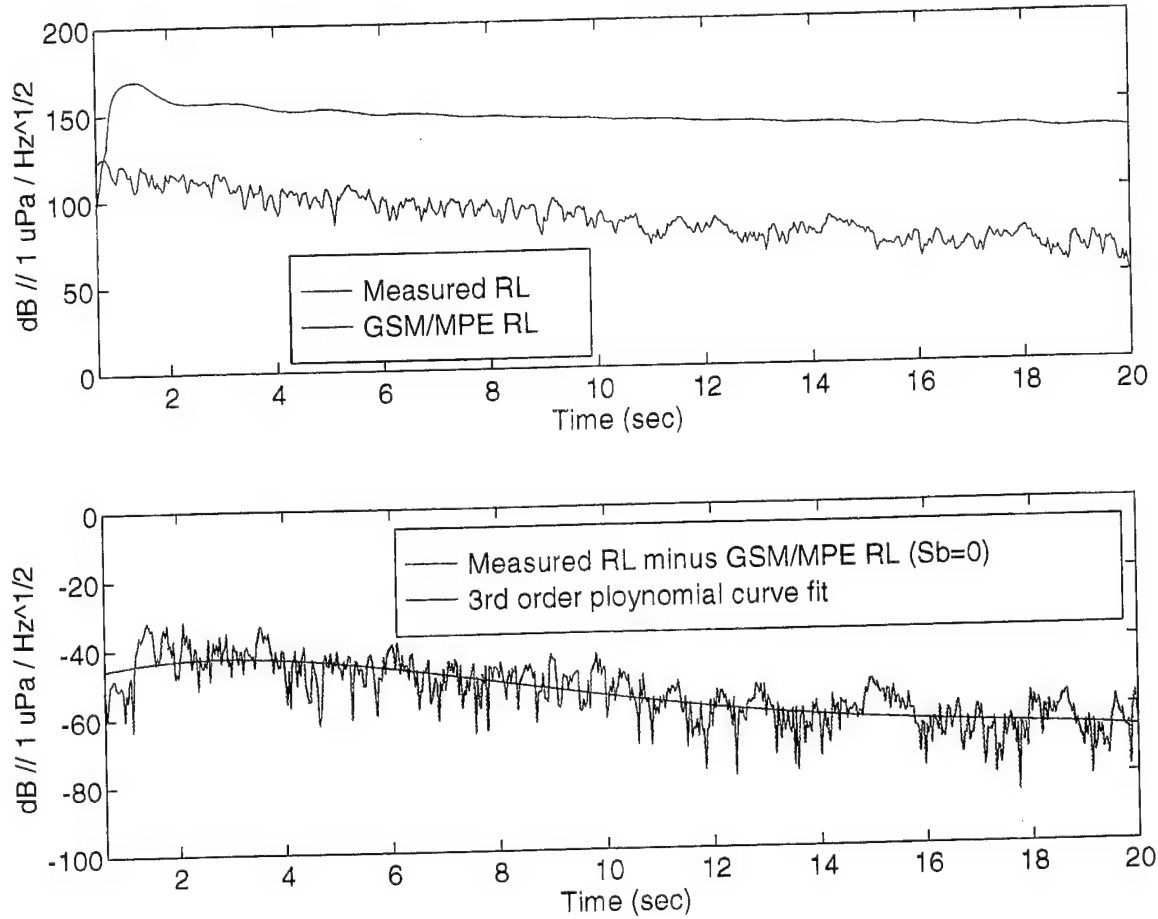


Figure 28. Measured RL and GSM/MPE RL with  $S_b$  set to zero for ping 2, beam 24 (top panel). Measured RL minus GSM/MPE RL with a 3rd-order polynomial cure fit (bottom panel).

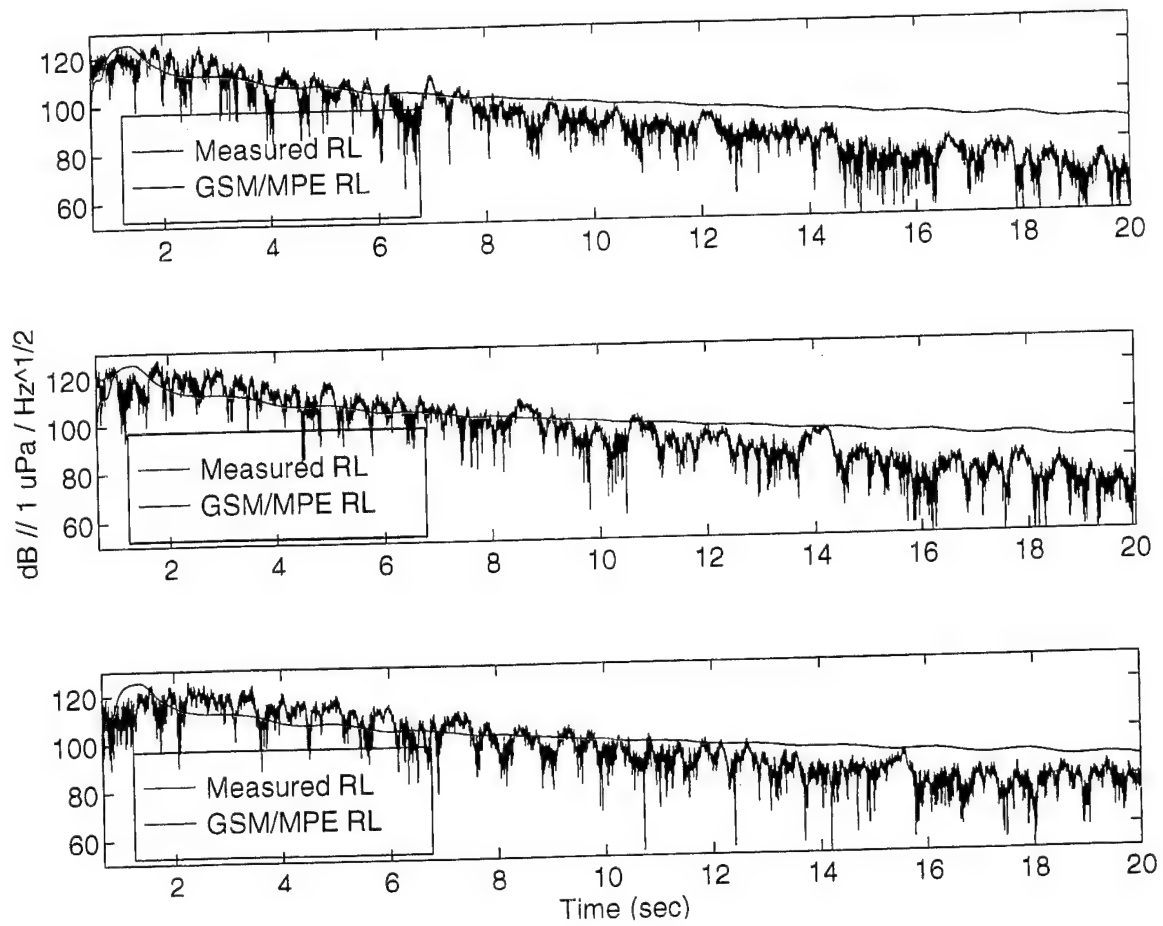


Figure 29a. Measured RL and GSM/MPE RL using the NPS model for ping 2, beam 1 (top panel), ping 2, beam 3 (center panel), and ping 2, beam 5 (bottom panel).

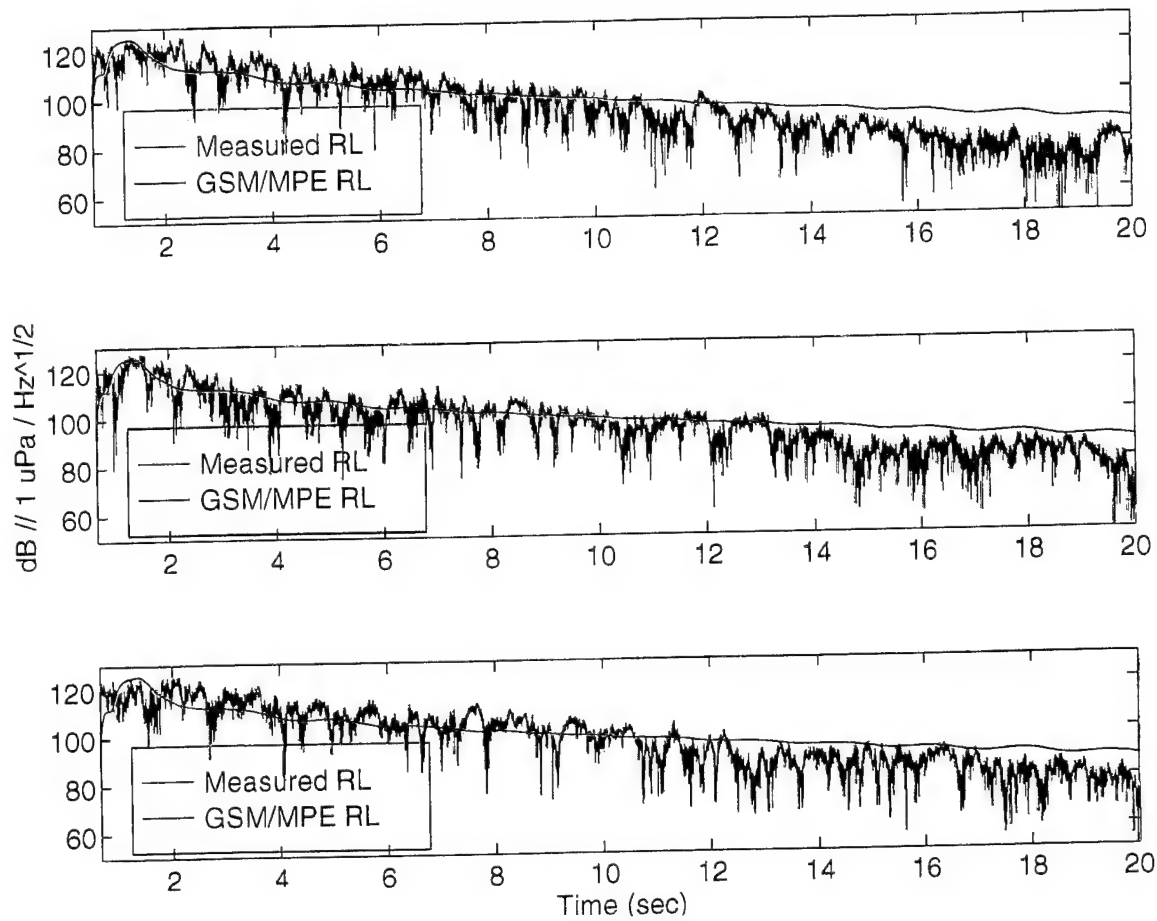


Figure 29b. Measured RL and GSM/MPE RL using the NPS model for ping 2, beam 7 (top panel), ping 2, beam 9 (center panel), and ping 2, beam 11 (bottom panel).

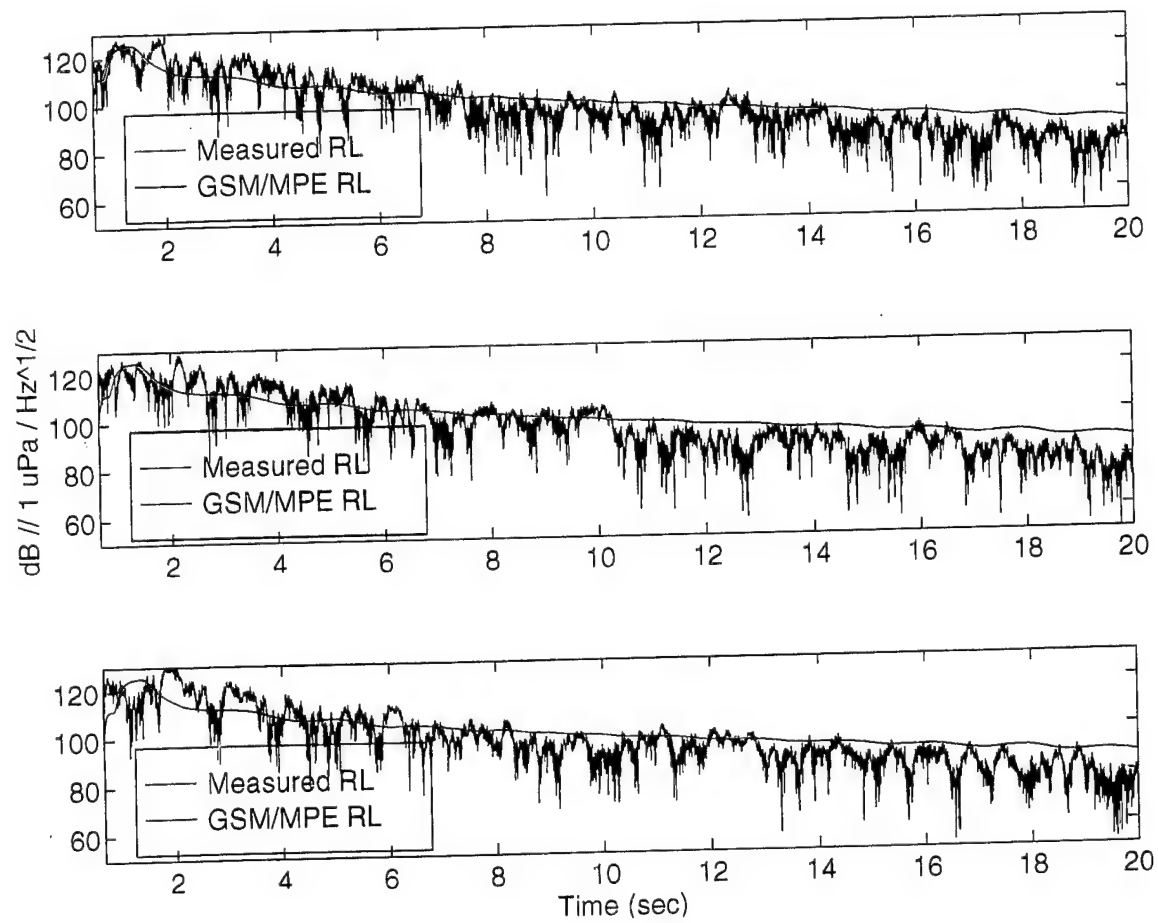


Figure 29c. Measured RL and GSM/MPE RL using the NPS model for ping 2, beam 13 (top panel), ping 2, beam 15 (center panel), and ping 2, beam 17 (bottom panel).

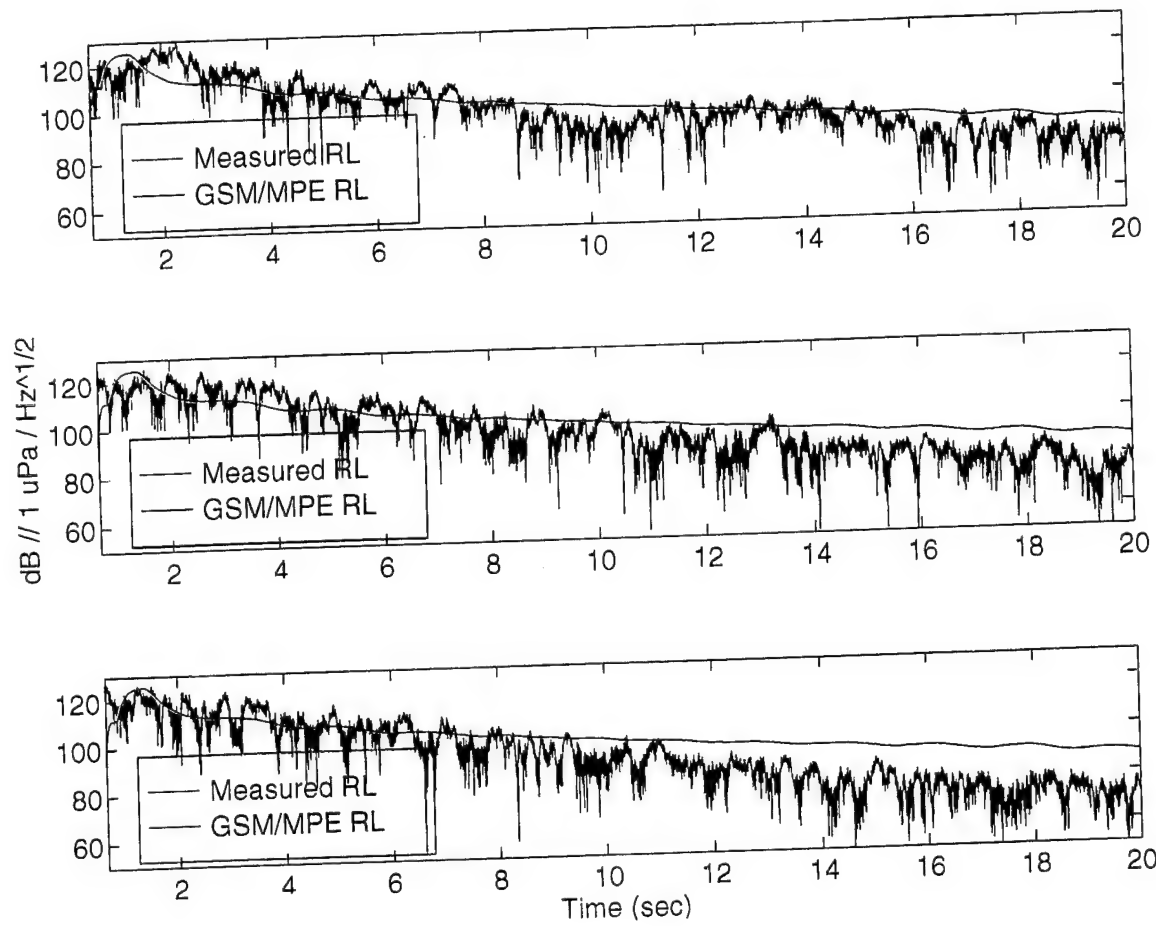


Figure 29d. Measured RL and GSM/MPE RL using the NPS model for ping 2, beam 19 (top panel), ping 2, beam 21 (center panel), and ping 2, beam 23 (bottom panel).

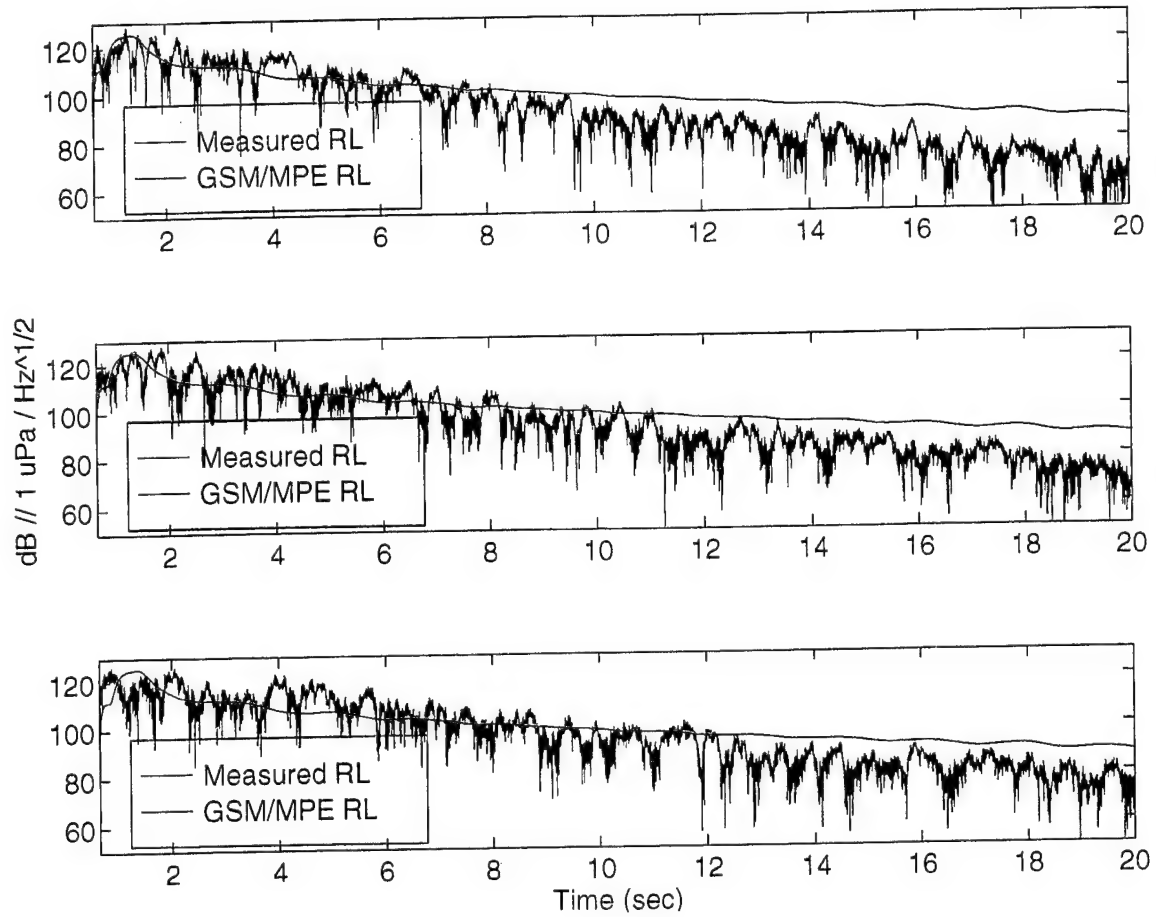


Figure 30a. Measured RL and GSM/MPE RL using the NPS model for ping 30, beam 1 (top panel), ping 30, beam 3 (center panel), and ping 30, beam 5 (bottom panel).

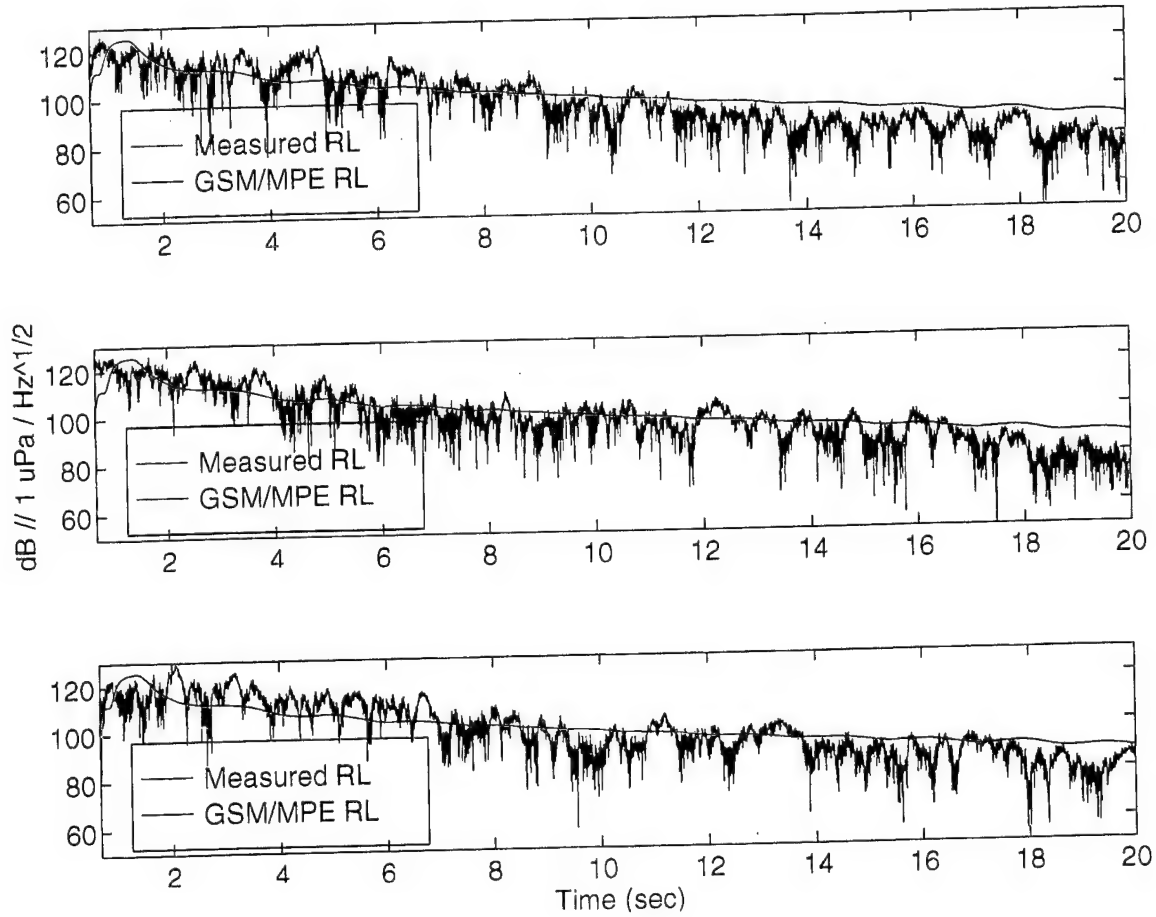


Figure 30b. Measured RL and GSM/MPE RL using the NPS model for ping 30, beam 7 (top panel), ping 30, beam 9 (center panel), and ping 30, beam 11 (bottom panel).

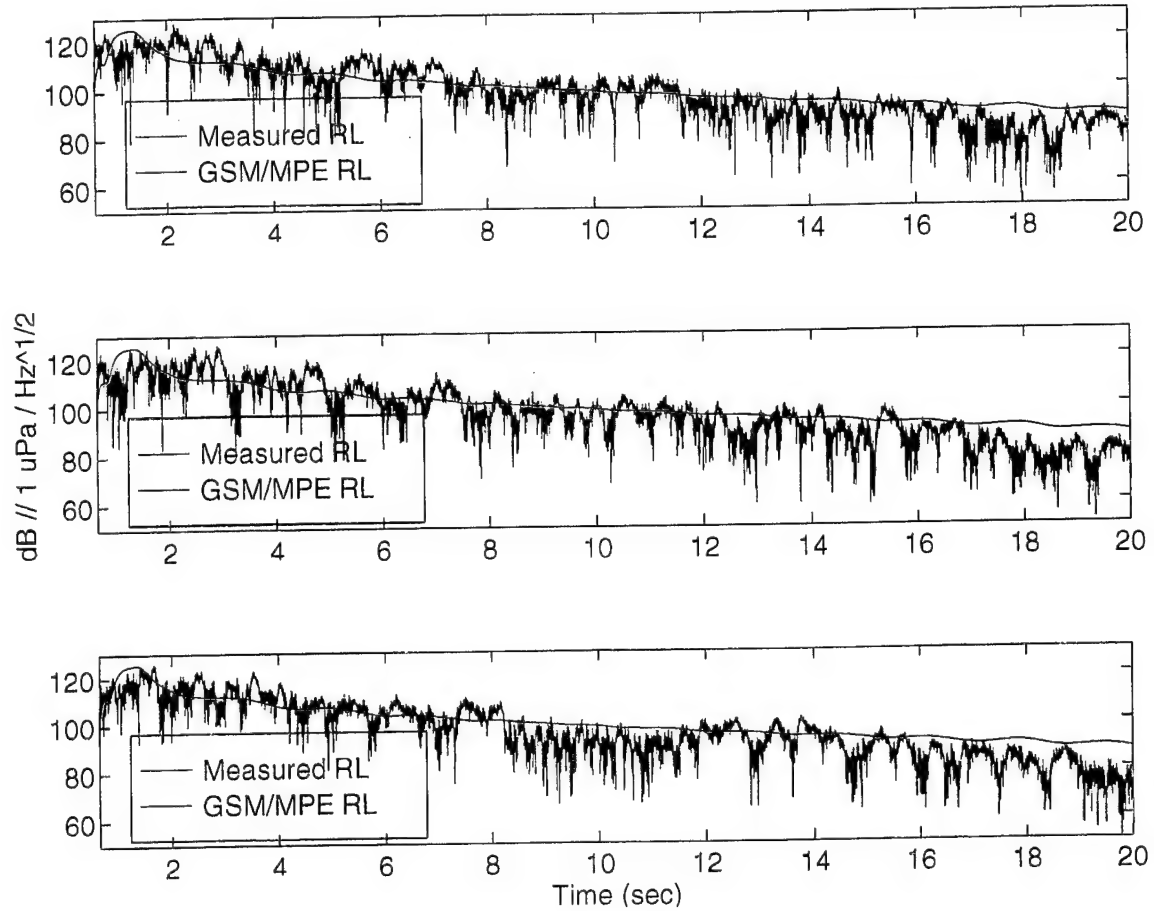


Figure 30c. Measured RL and GSM/MPE RL using the NPS model for ping 30, beam 13 (top panel), ping 30, beam 15 (center panel), and ping 30, beam 17 (bottom panel).

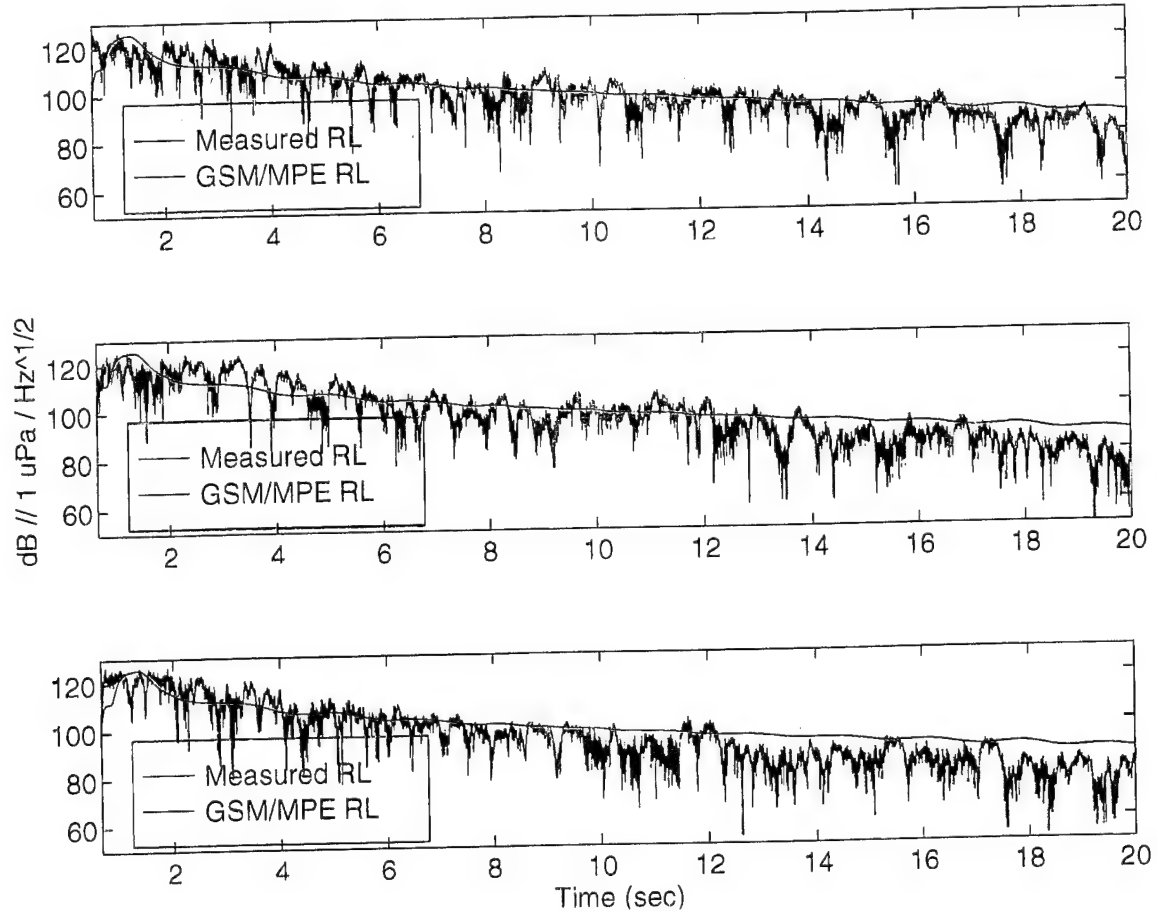


Figure 30d. Measured RL and GSM/MPE RL using the NPS model for ping 30, beam 19 (top panel), ping 30, beam 21 (center panel), and ping 30, beam 23 (bottom panel).

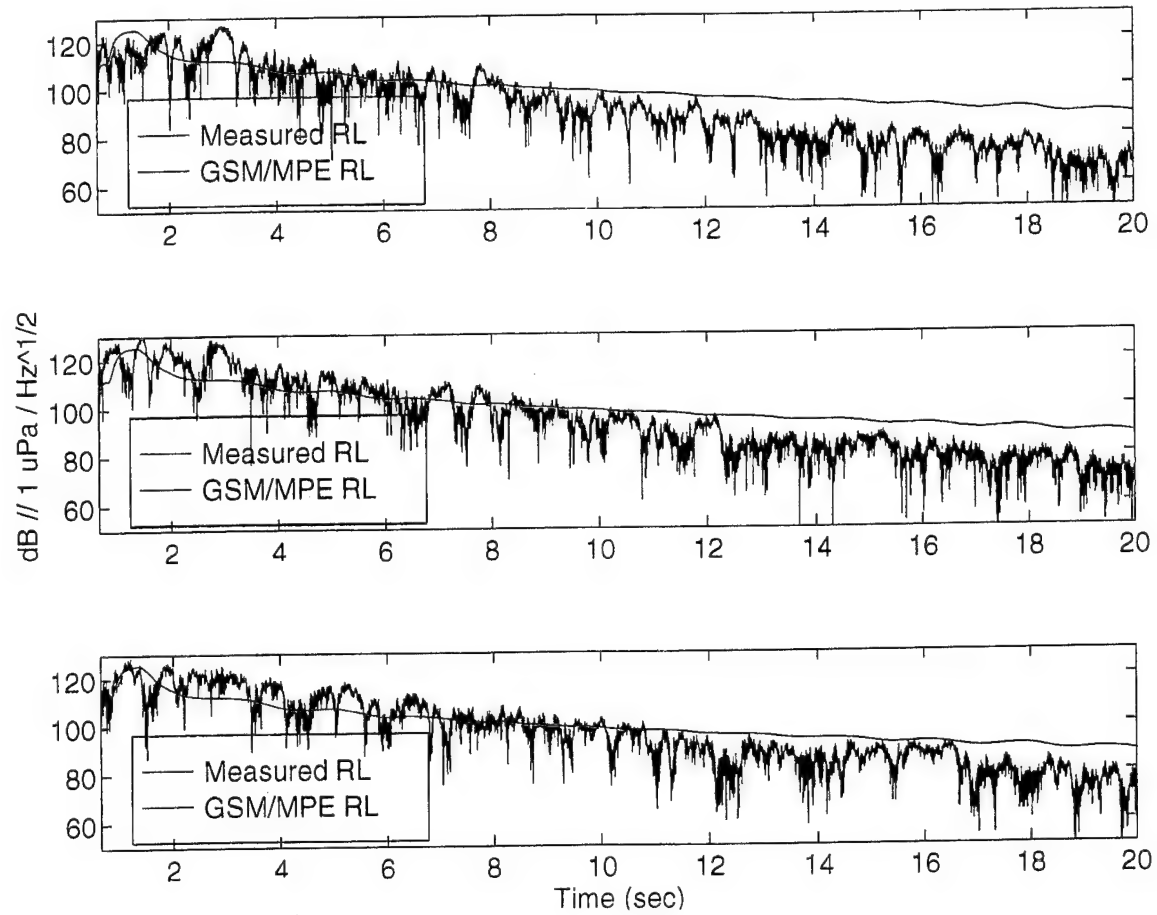


Figure 31a. Measured RL and GSM/MPE RL using the NPS model for ping 60, beam 1 (top panel), ping 60, beam 3 (center panel), and ping 60, beam 5 (bottom panel).

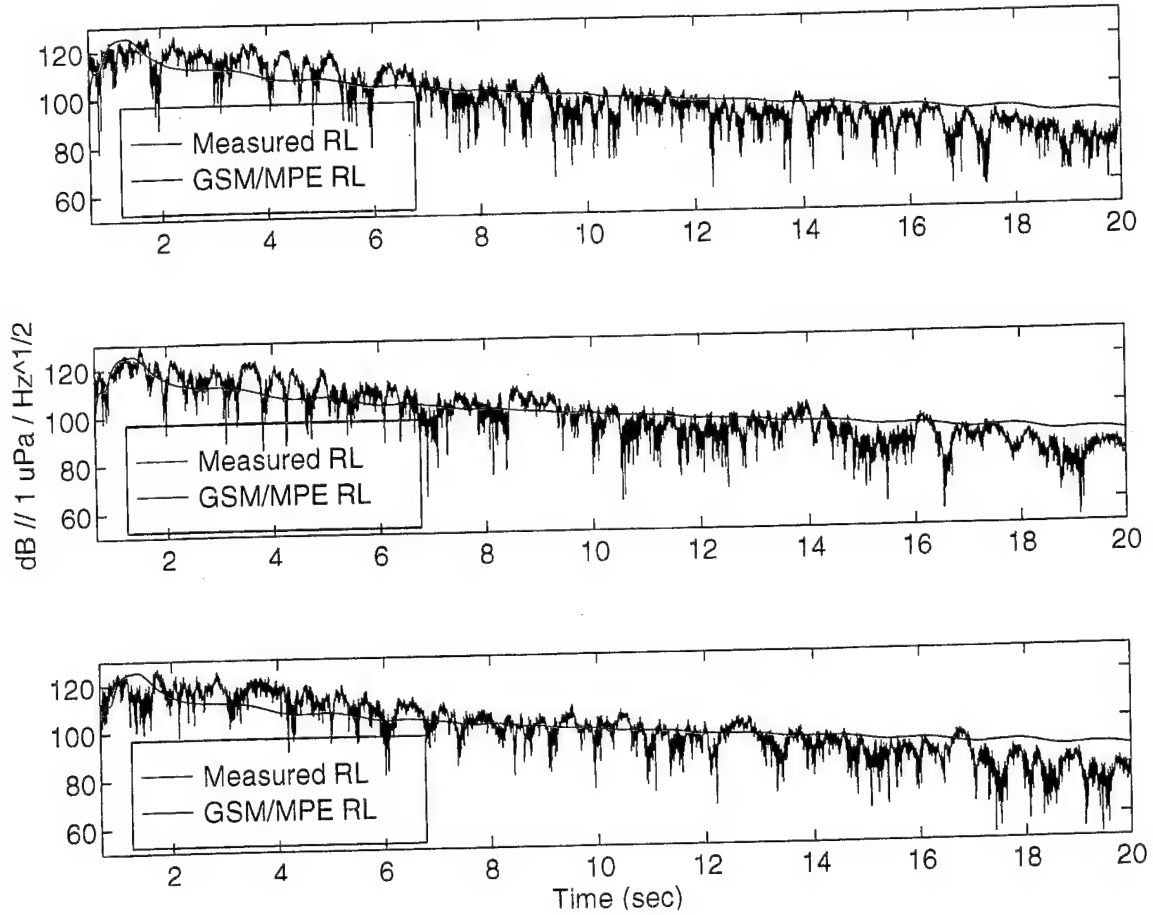


Figure 31b. Measured RL and GSM/MPE RL using the NPS model for ping 60, beam 7 (top panel), ping 60, beam 9 (center panel), and ping 60, beam 11 (bottom panel).

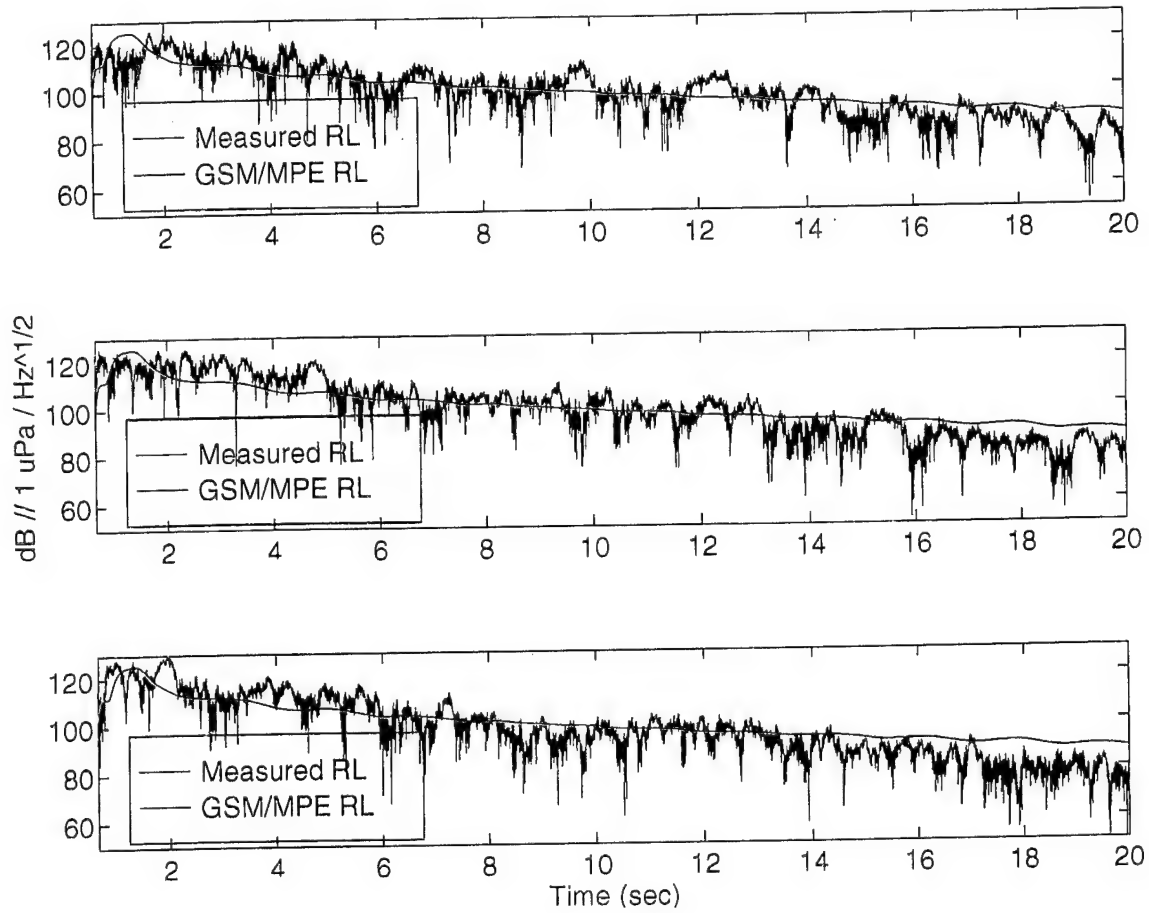


Figure 31c. Measured RL and GSM/MPE RL using the NPS model for ping 60, beam 13 (top panel), ping 60, beam 15 (center panel), and ping 60, beam 17 (bottom panel).

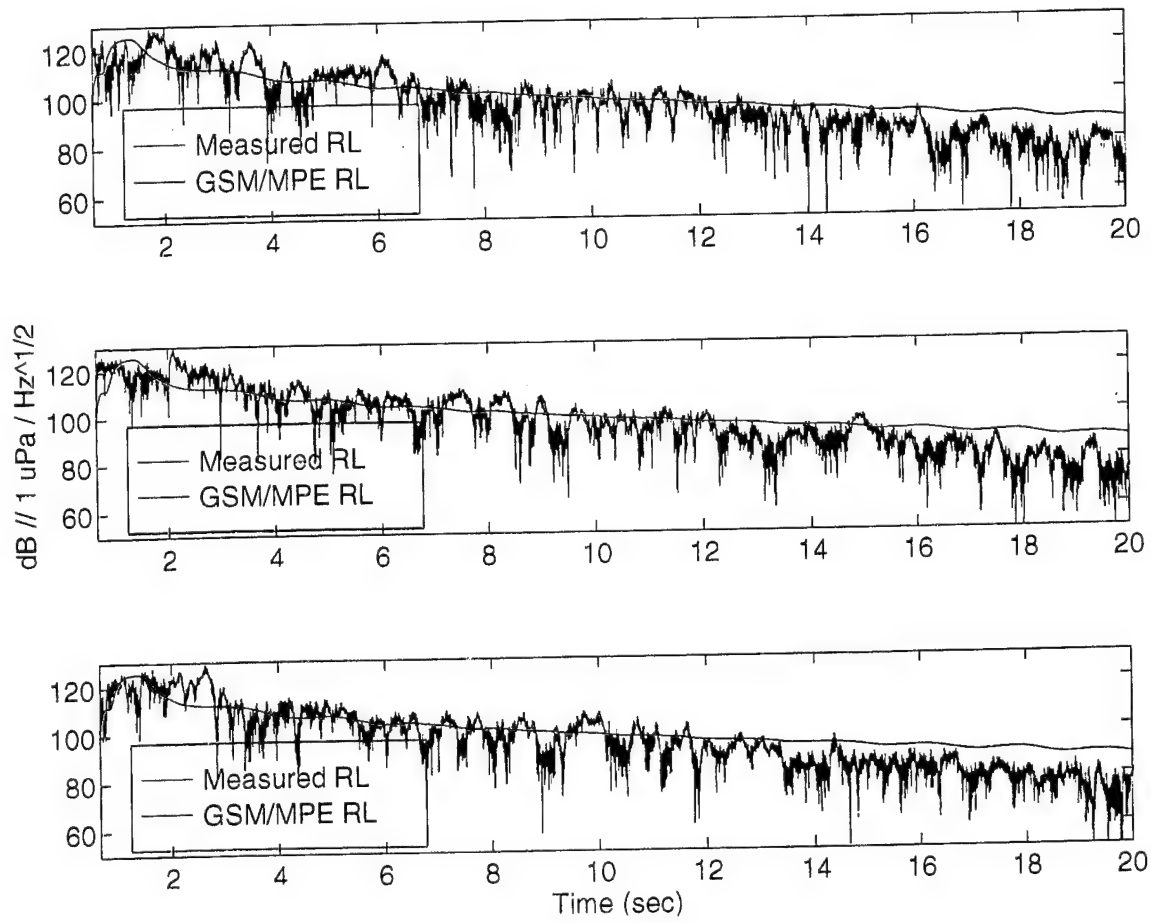


Figure 31d. Measured RL and GSM/MPE RL using the NPS model for ping 60, beam 19 (top panel), ping 60, beam 21 (center panel), and ping 60, beam 23 (bottom panel).

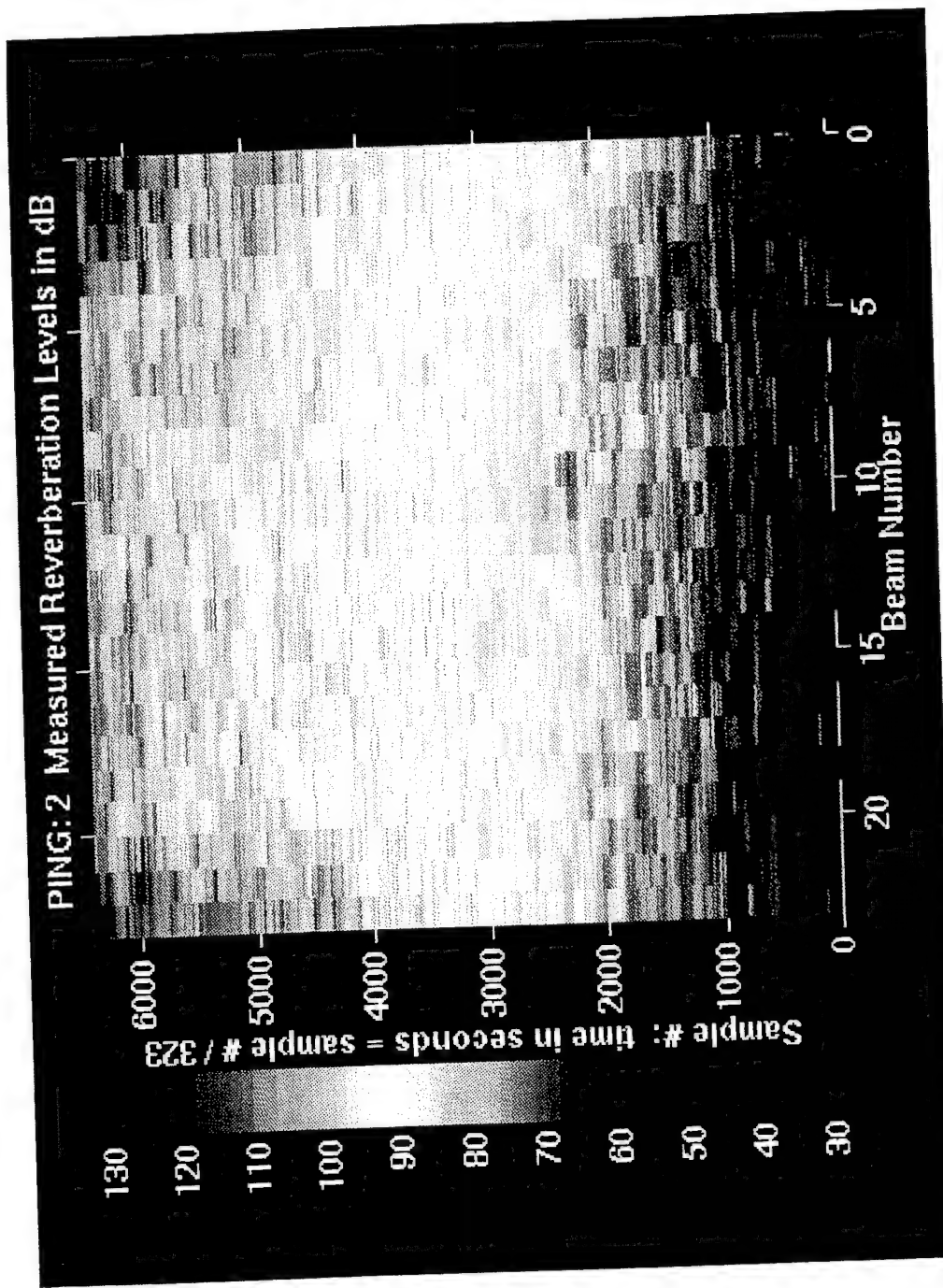


Figure 32. Measured RL for all beams of ping 2. Red represents regions of high RL, blue represents low RL. Azimuth angle dependence is not included in the plot. The y-axis is the sample number and can be converted to time (sec) by dividing by 323. Note the increase in RL for the center steered beams (10-15) compared to the off-center steered beams.

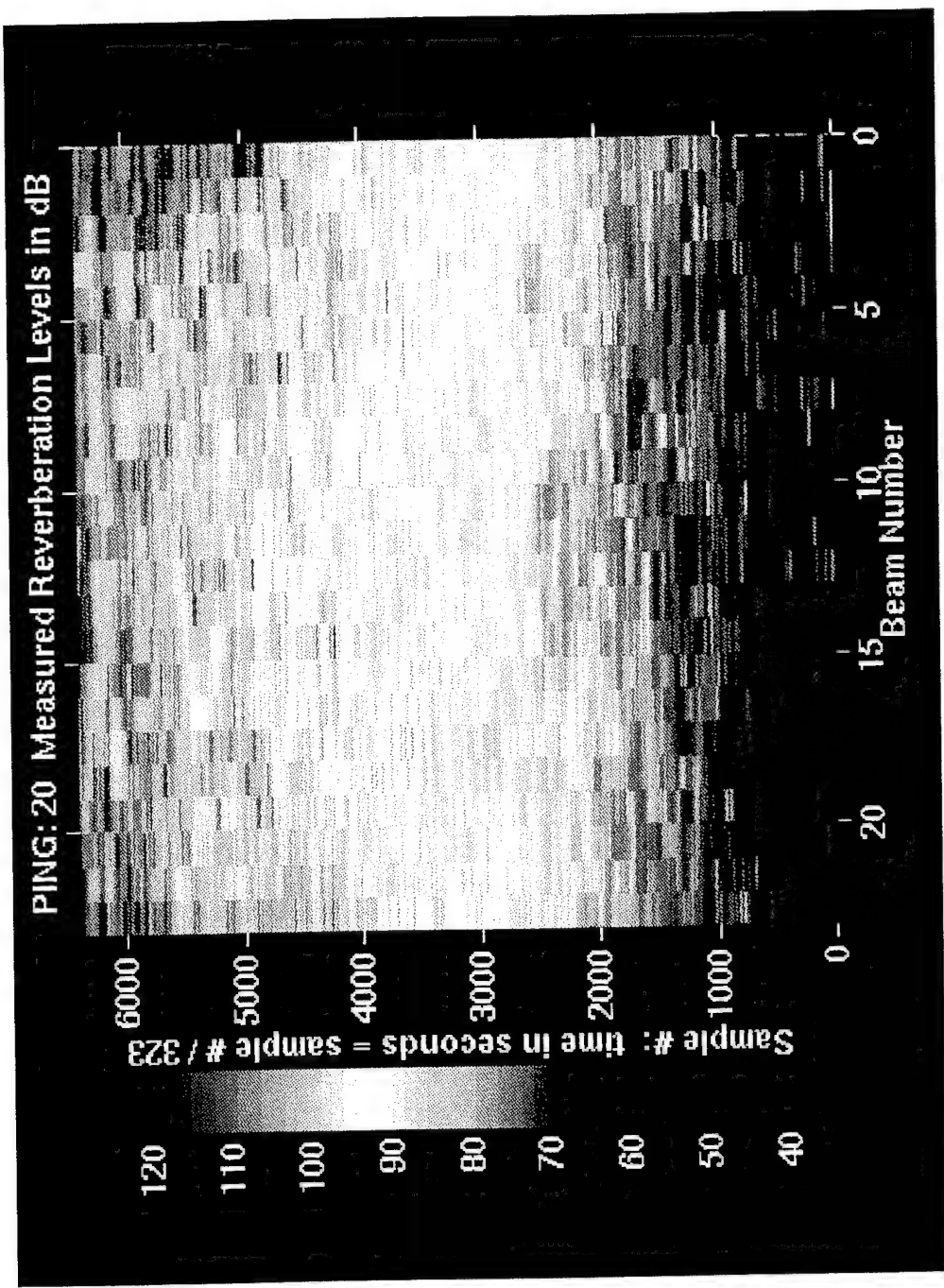


Figure 33. Same as Figure 32 except for ping 20.

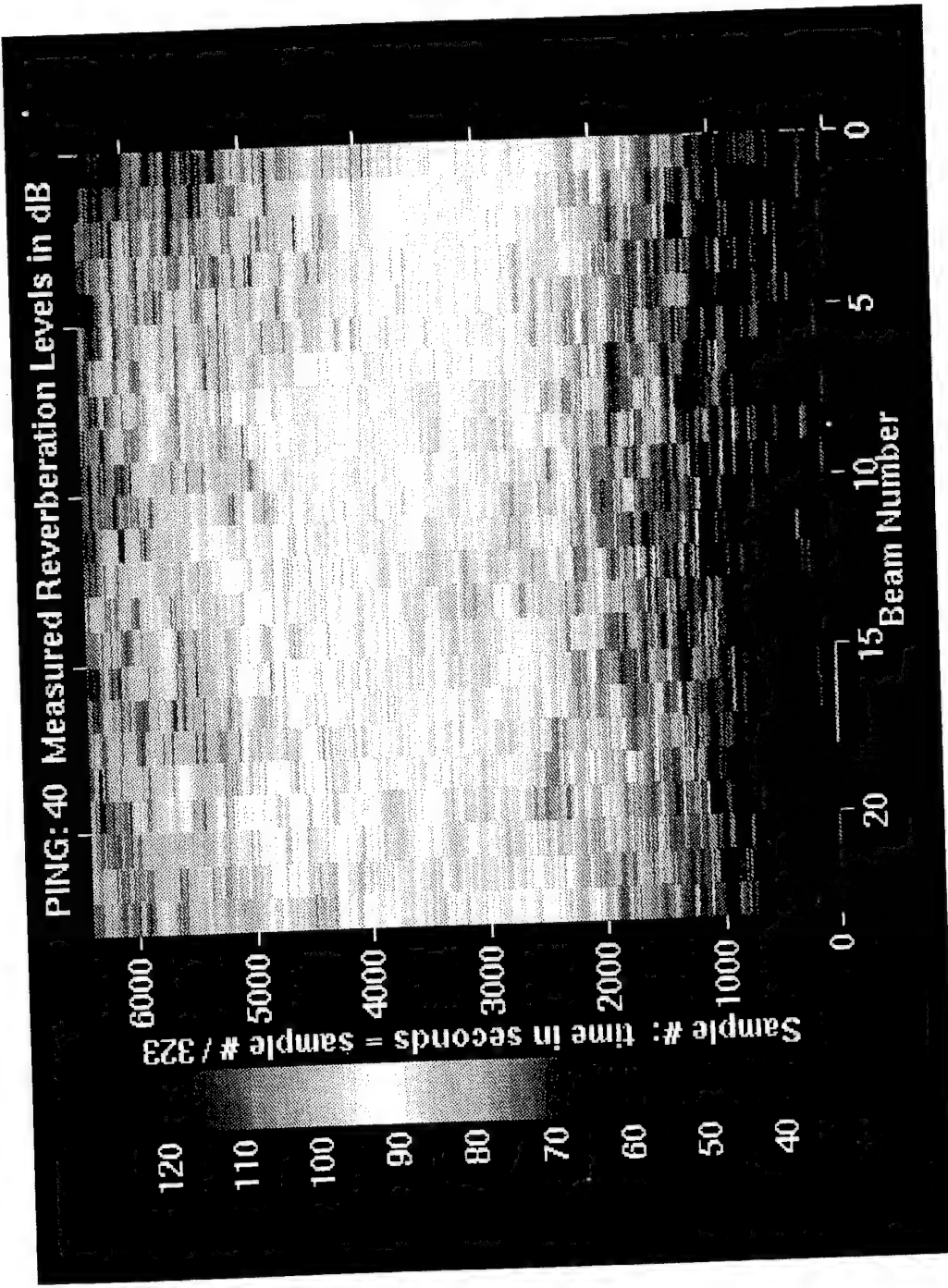


Figure 34. Same as Figure 32 except for ping 40.

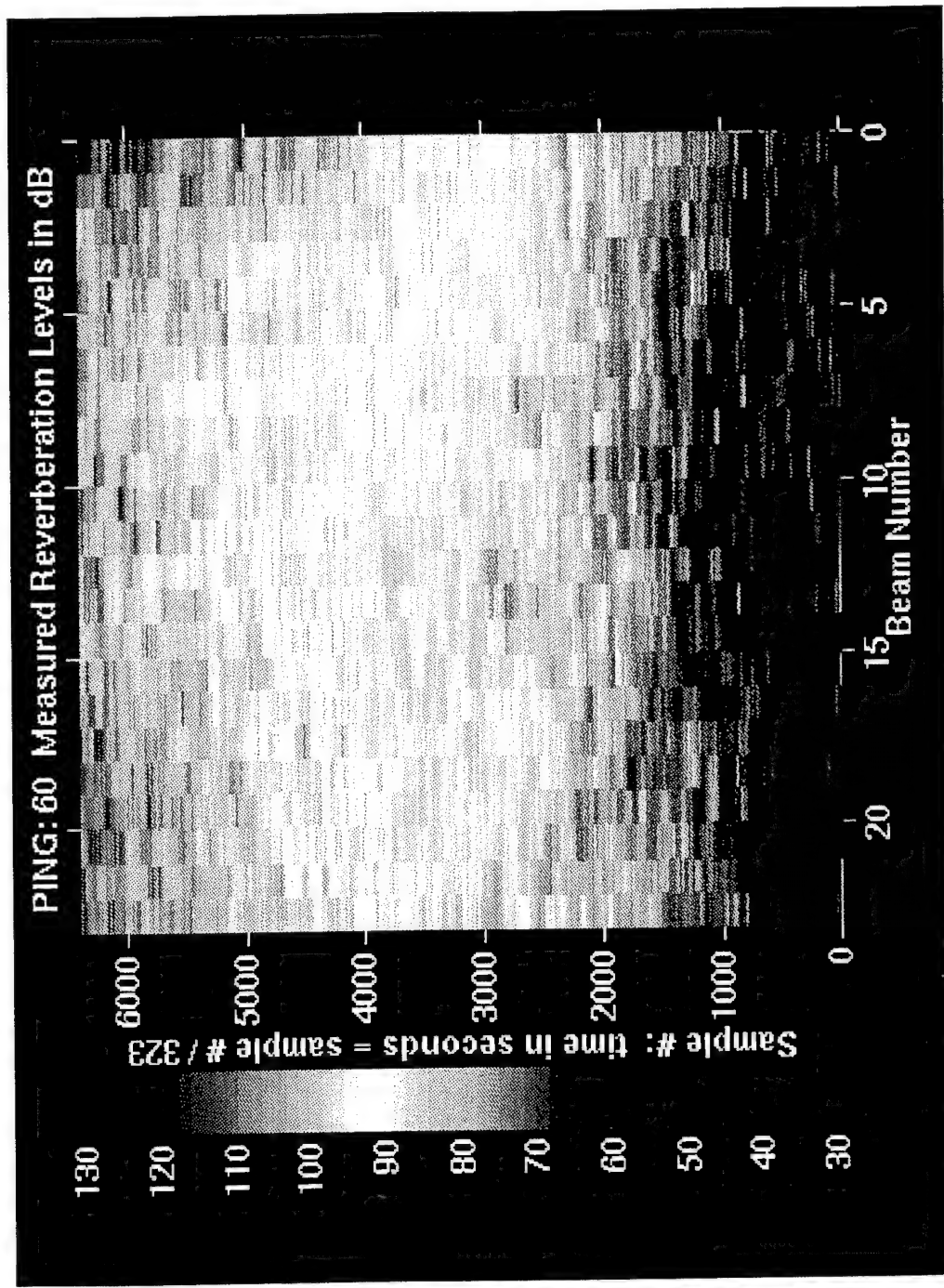


Figure 35. Same as Figure 32 except for ping 60.

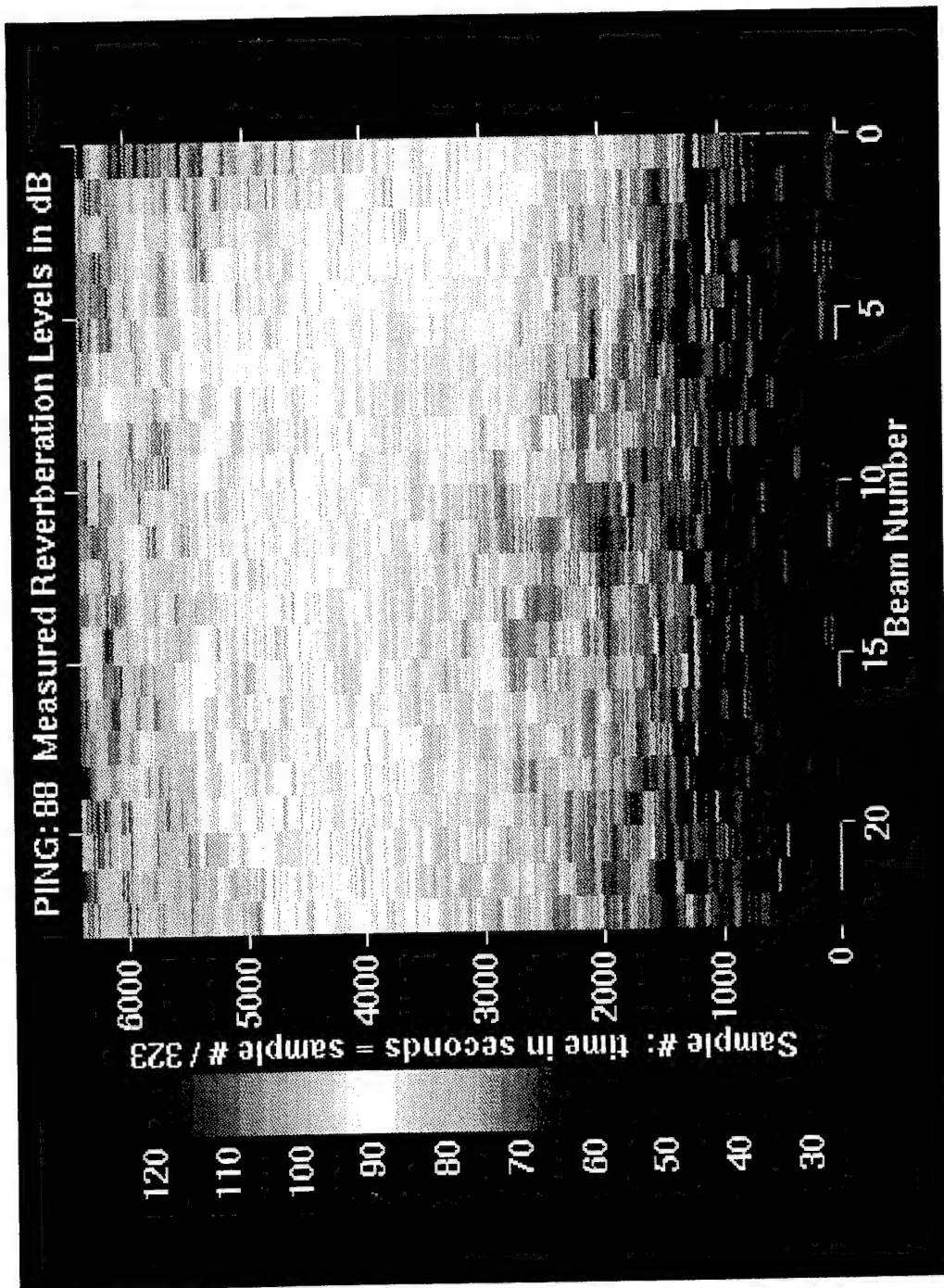
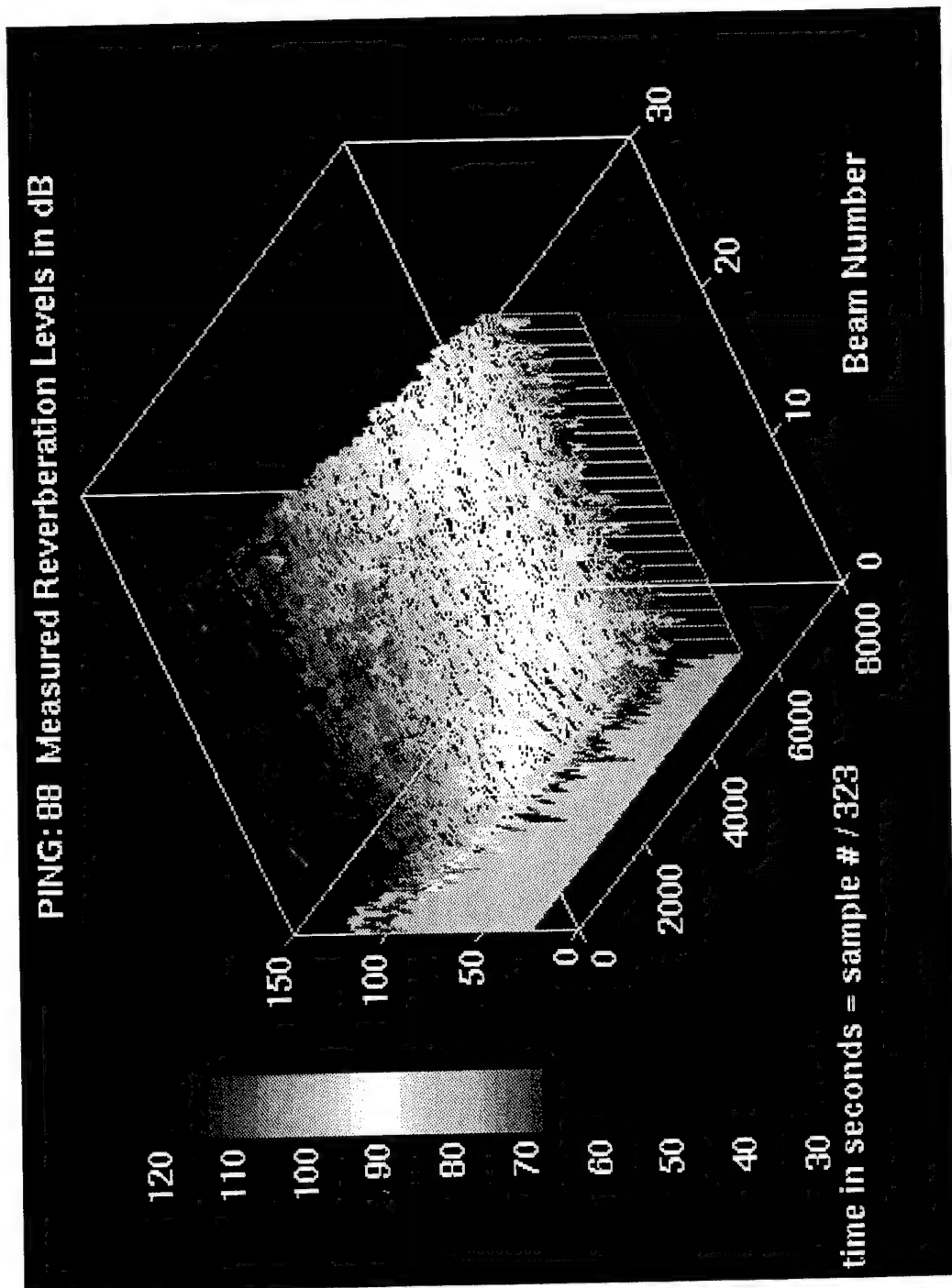


Figure 36. Same as Figure 32 except for ping 88.



148

Figure 37. Same as Figure 36 except plotted in 3-D.

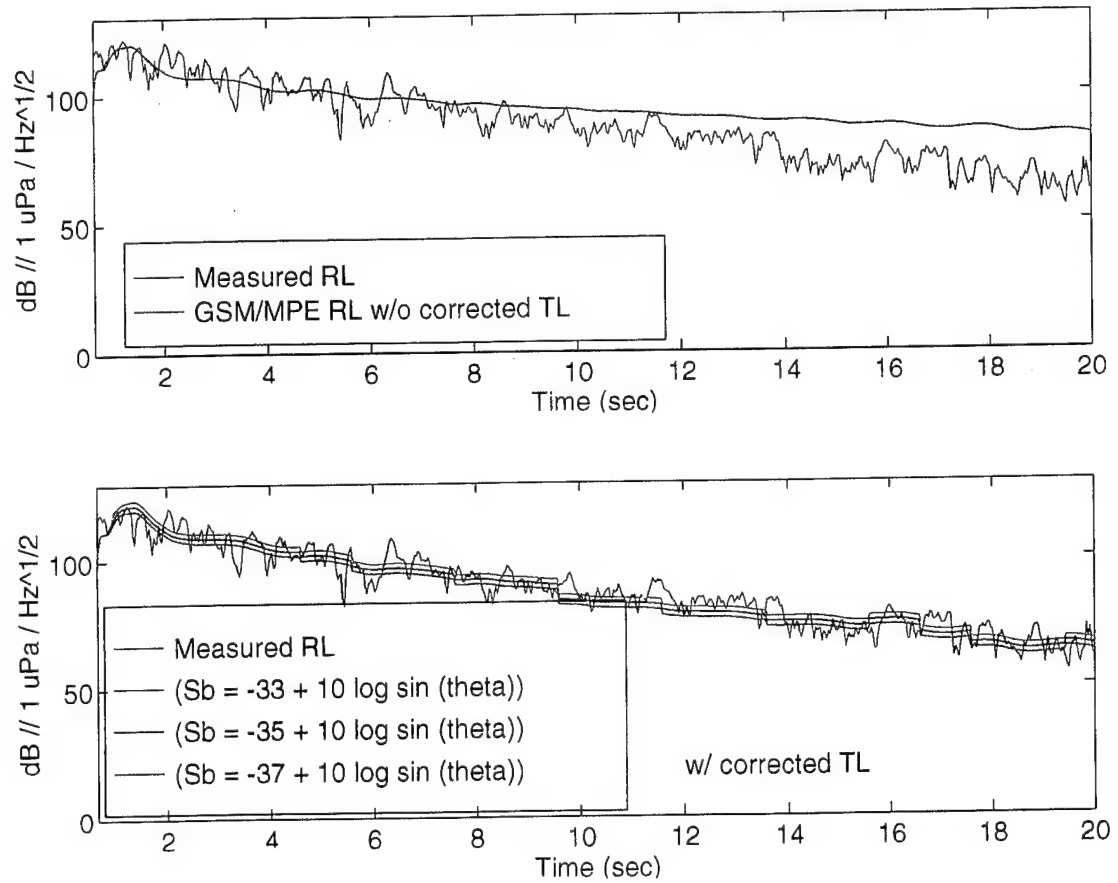


Figure 38a. Comparison between the Measured RL and GSM/MPE RL (without corrected TL) using the NPS silt-clay model as input (top panel) for ping 2, beam 1. Measured RL and GSM/MPE RL (with corrected TL) using three different values of  $10 \log \mu$  (bottom panel). The angular dependence is modeled as  $\sin(\theta)$ .

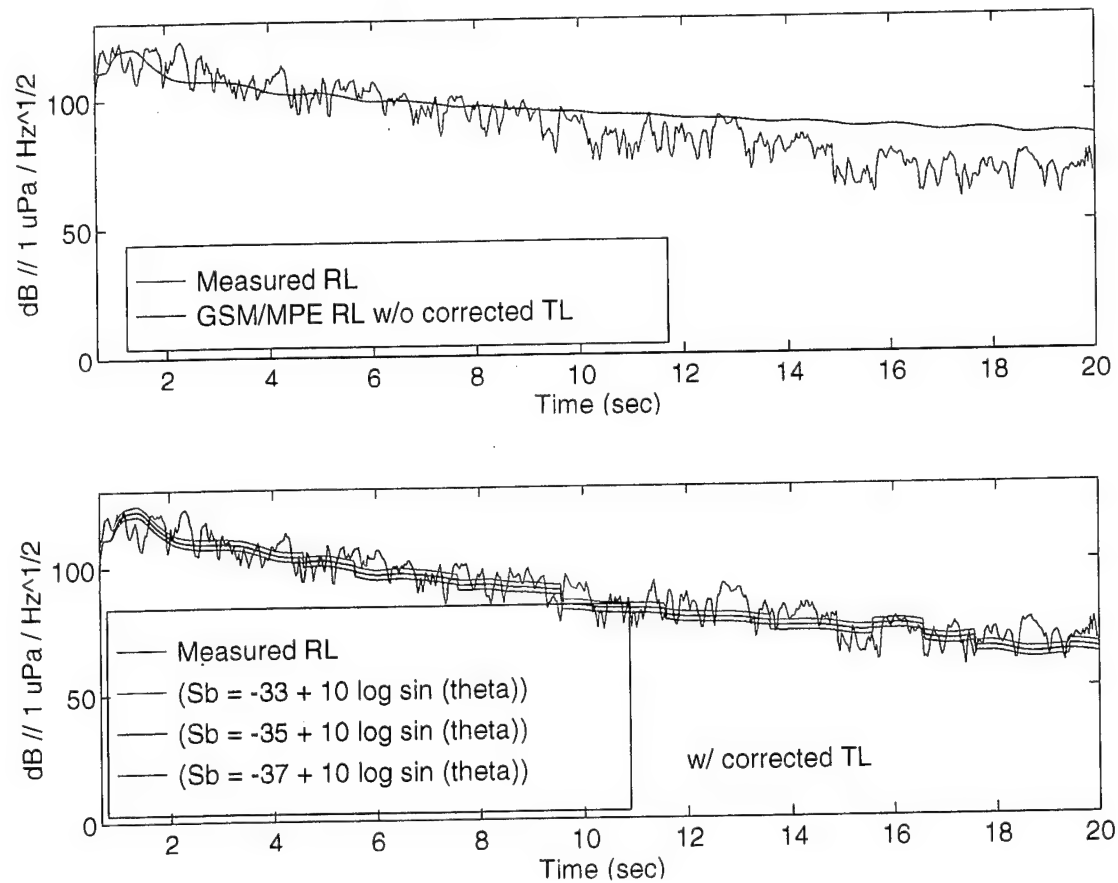


Figure 38b. Same as Figure 38a except for ping 20, beam 1.

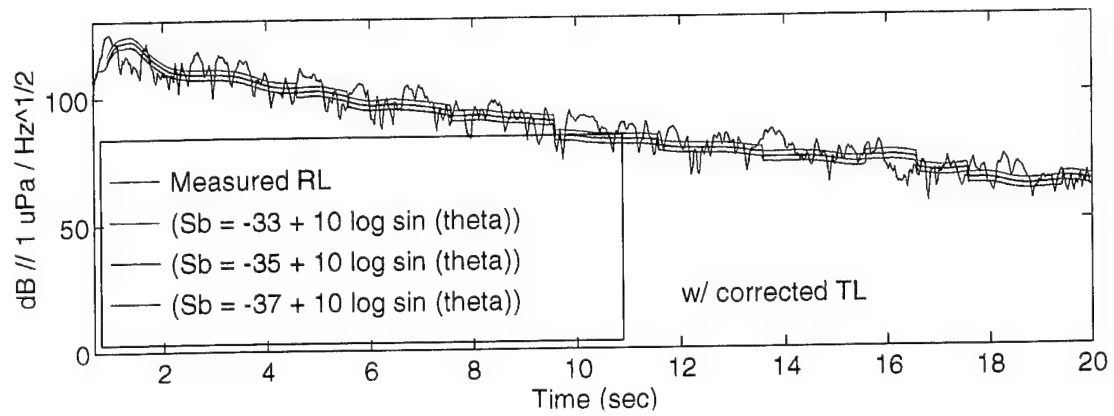
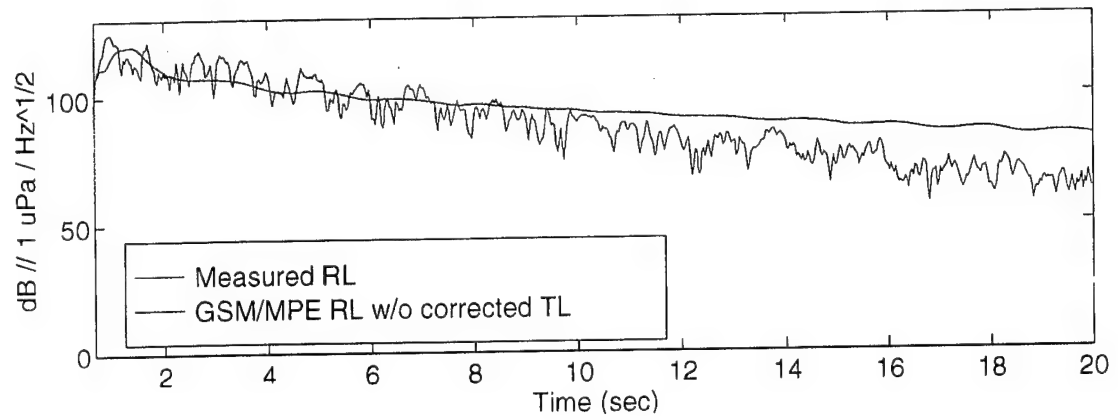


Figure 38c. Same as Figure 38a except for ping 40, beam 1.

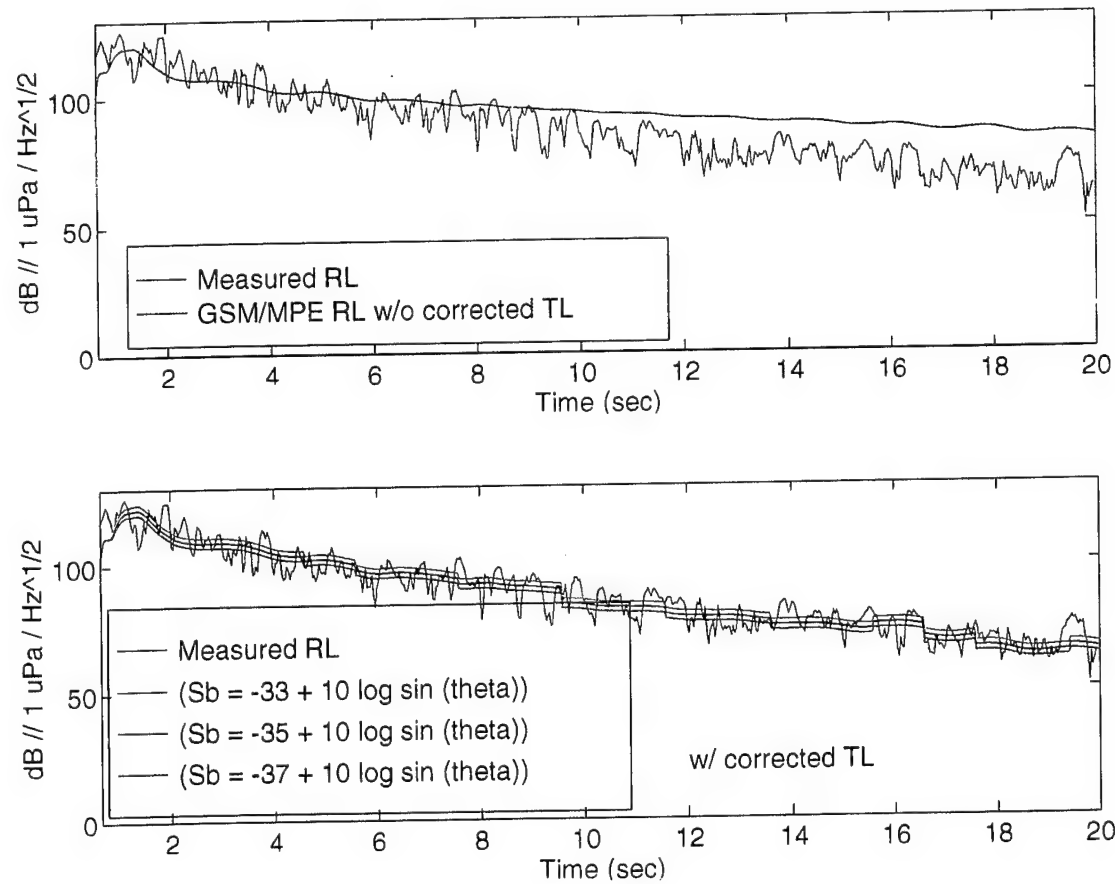


Figure 38e. Same as Figure 38a except for ping 88, beam 1.

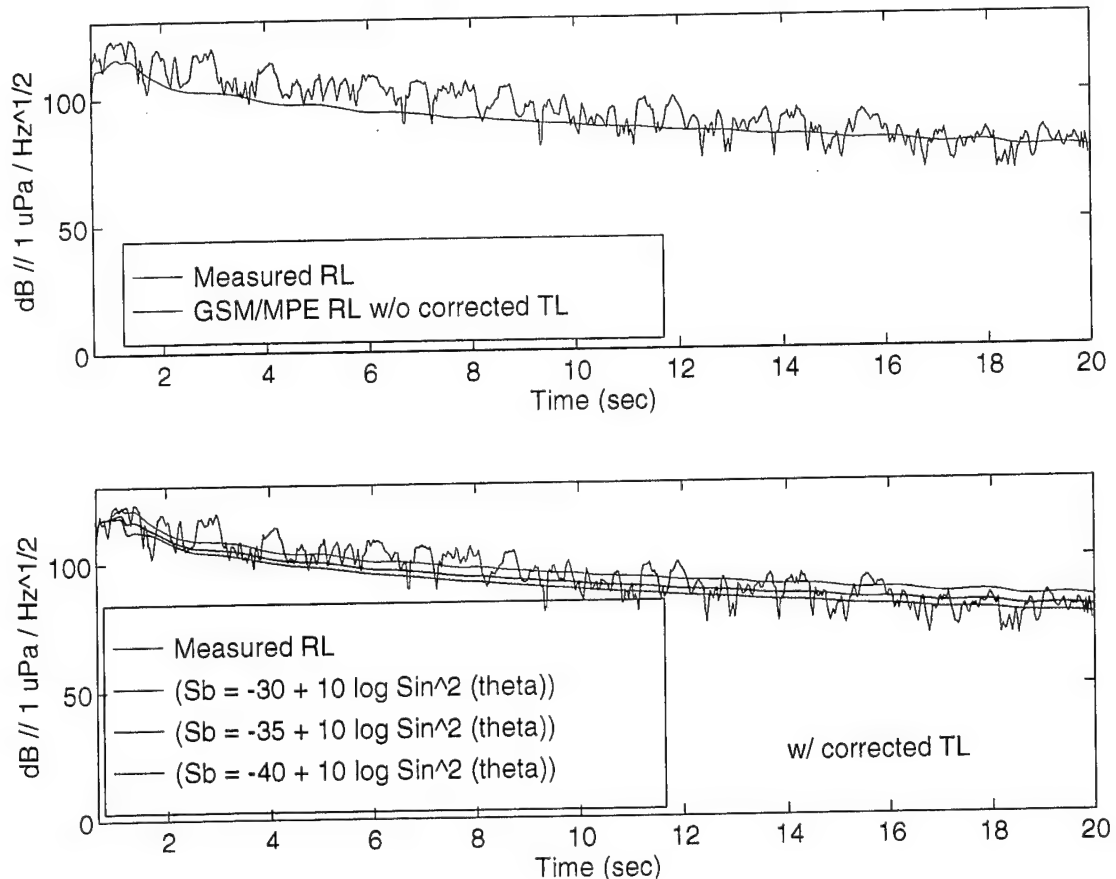


Figure 39a. Comparison between the Measured RL and GSM/MPE RL (without corrected TL) using the NPS silt-clay model as input (top panel) for ping 2, beam 12. Measured RL and GSM/MPE RL (with corrected TL) using three different values of  $10 \log \mu$  (bottom panel). The angular dependence is modeled as  $\sin(\theta)$ .

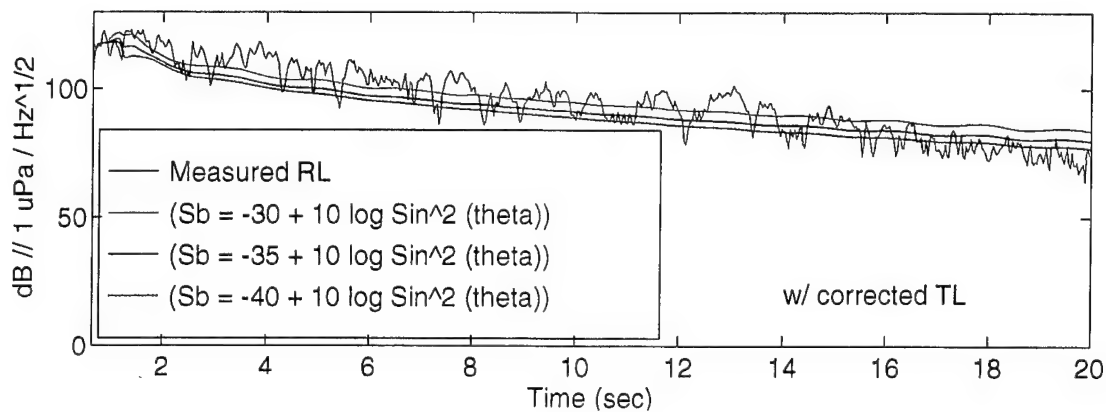
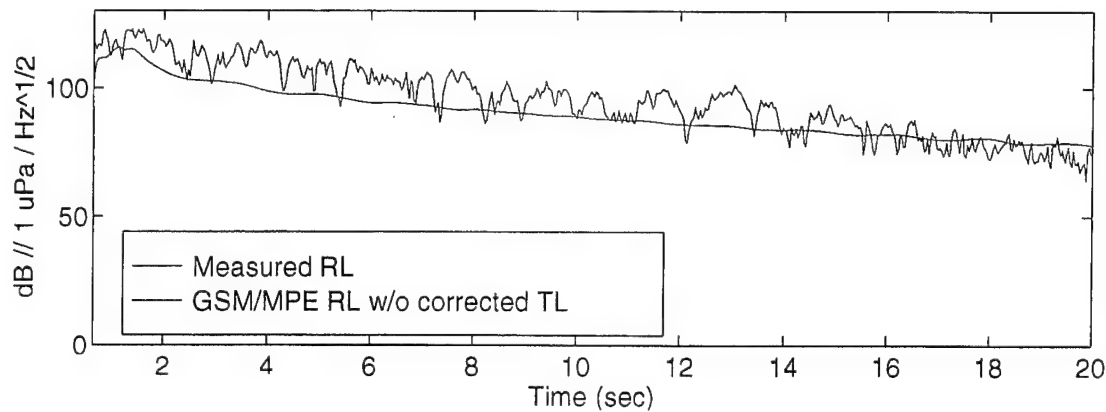


Figure 39b. Same as Figure 39a except for ping 20, beam 12.

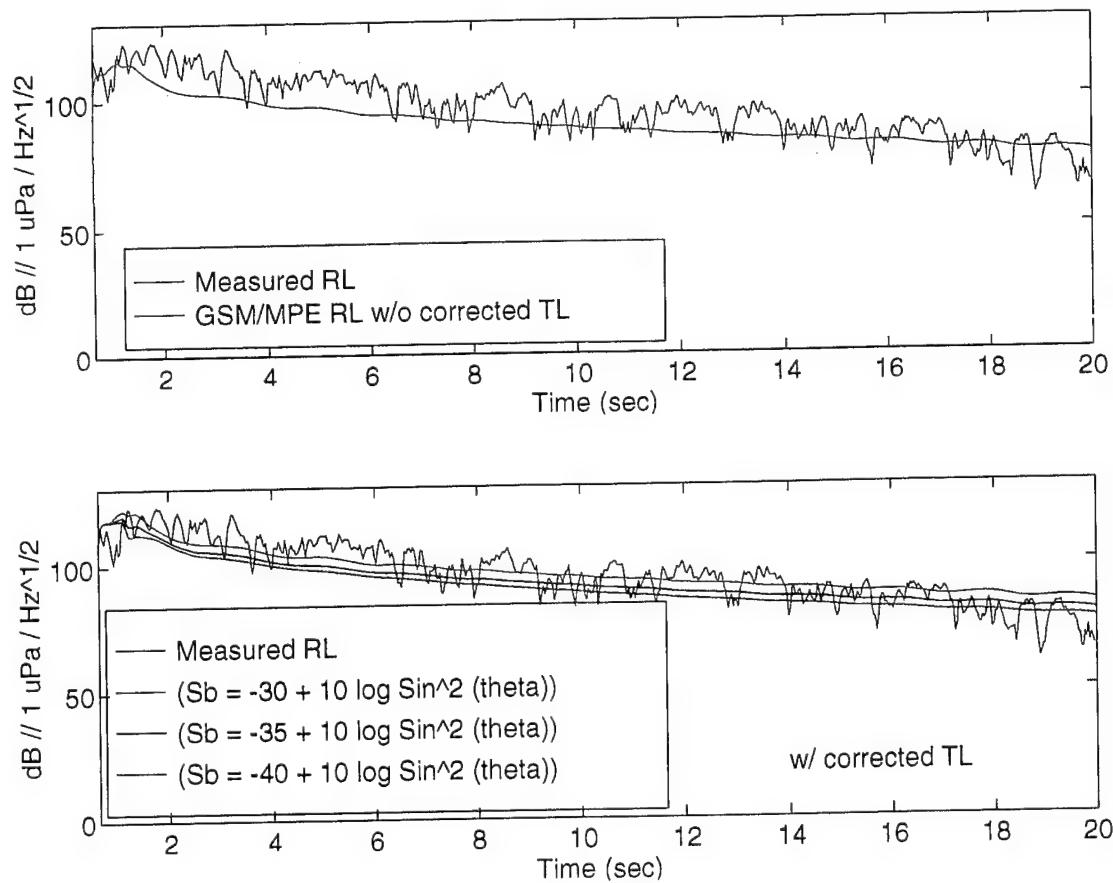


Figure 39c. Same as Figure 39a except for ping 40, beam 12.

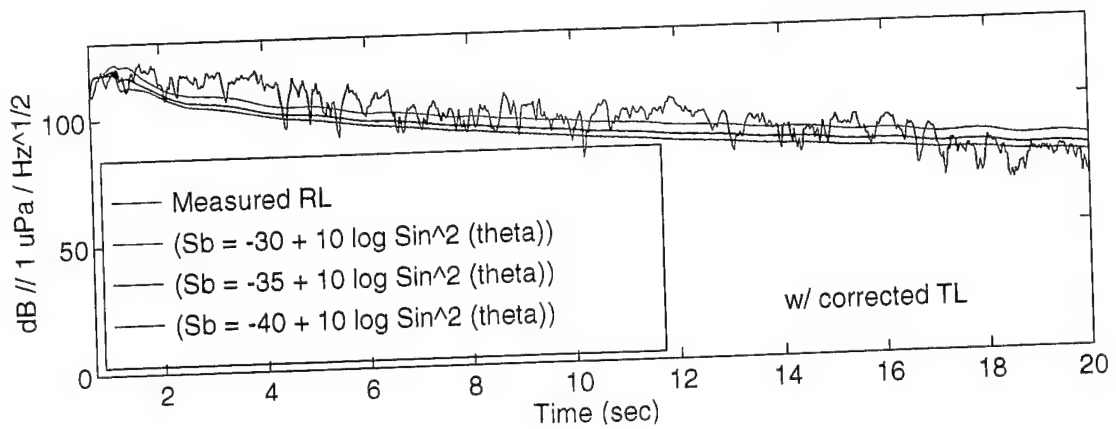
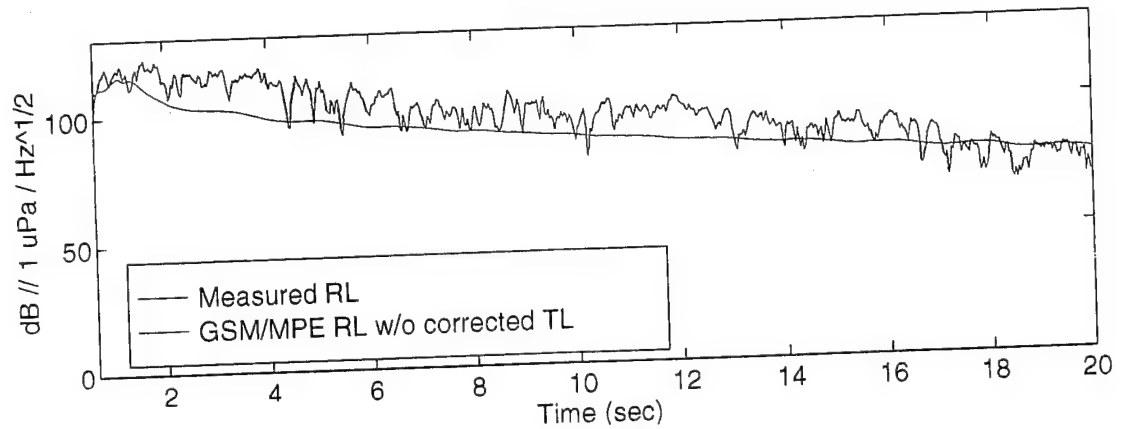


Figure 39d. Same as Figure 39a except for ping 60, beam 12.

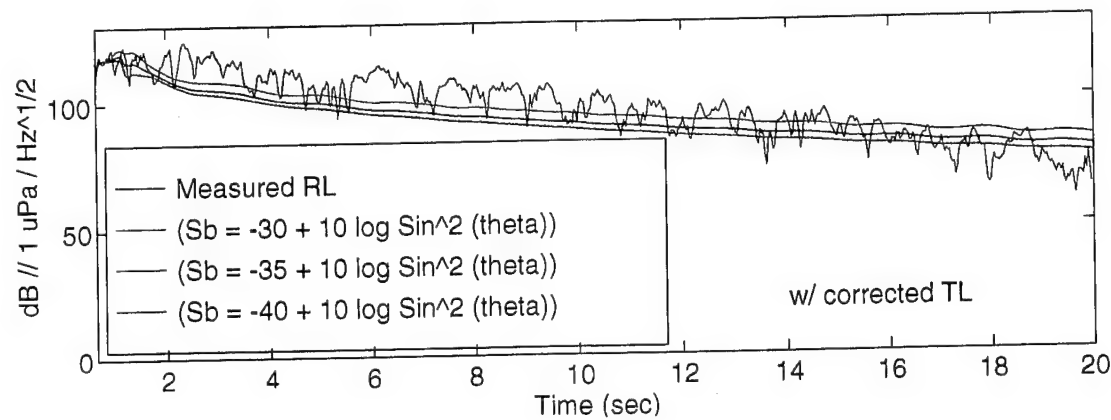
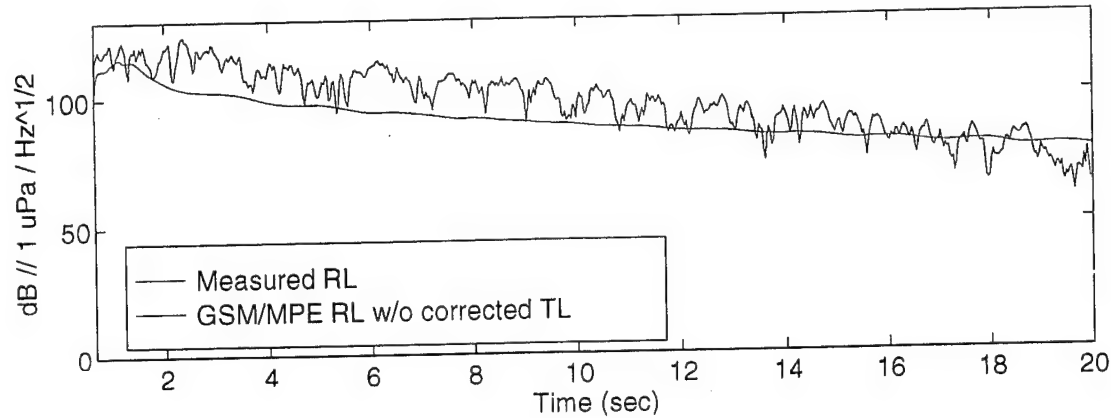


Figure 39e. Same as Figure 39a except for ping 88, beam 12.

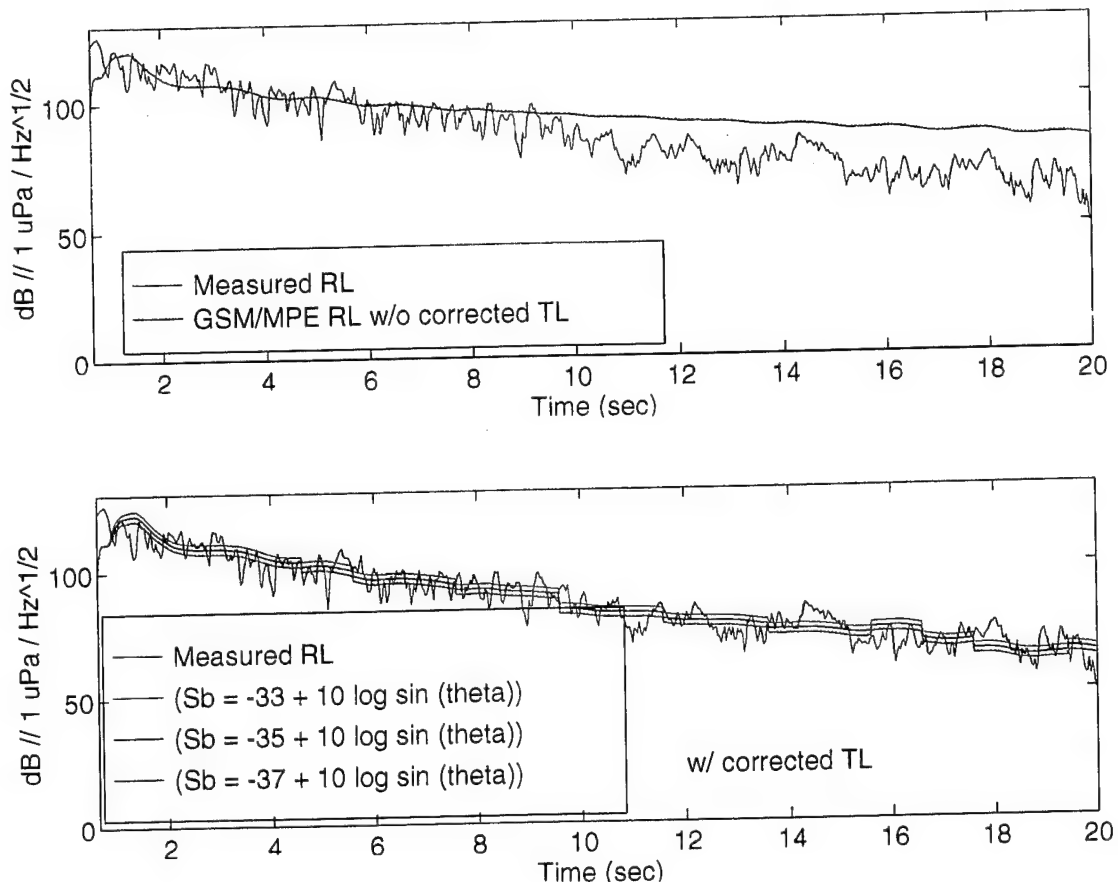


Figure 40a. Comparison between the Measured RL and GSM/MPE RL (without corrected TL) using the NPS silt-clay model as input (top panel) for ping 2, beam 24. Measured RL and GSM/MPE RL (with corrected TL) using three different values of  $10 \log \mu$  (bottom panel). The angular dependence is modeled as  $\sin(\theta)$ .

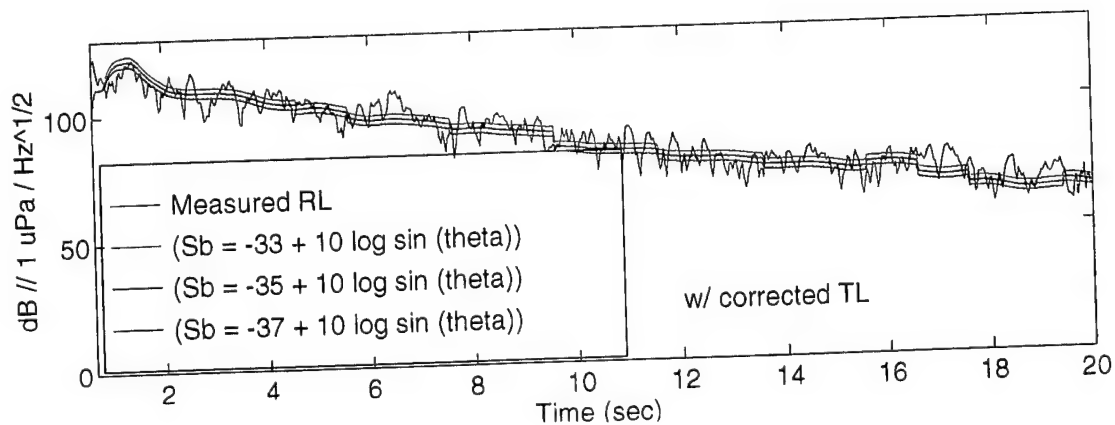
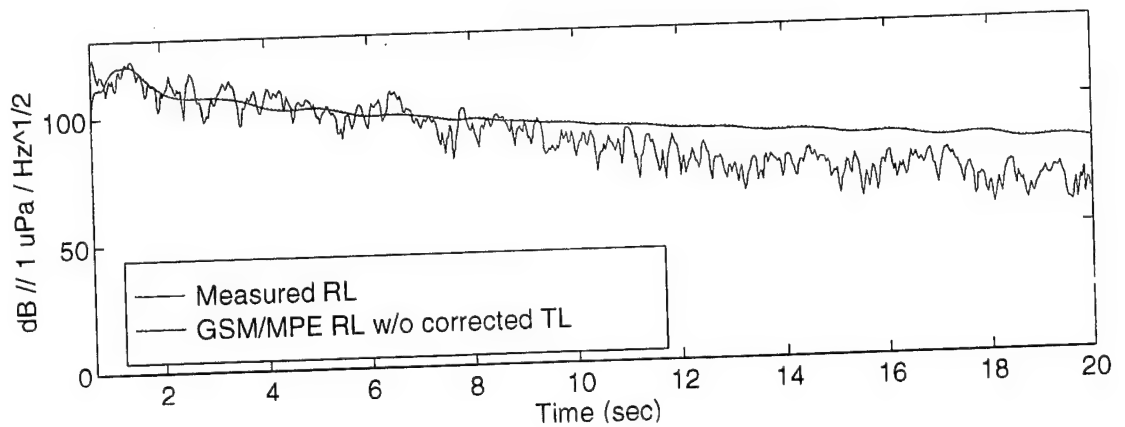


Figure 40b. Same as Figure 40a except for ping 20, beam 24.

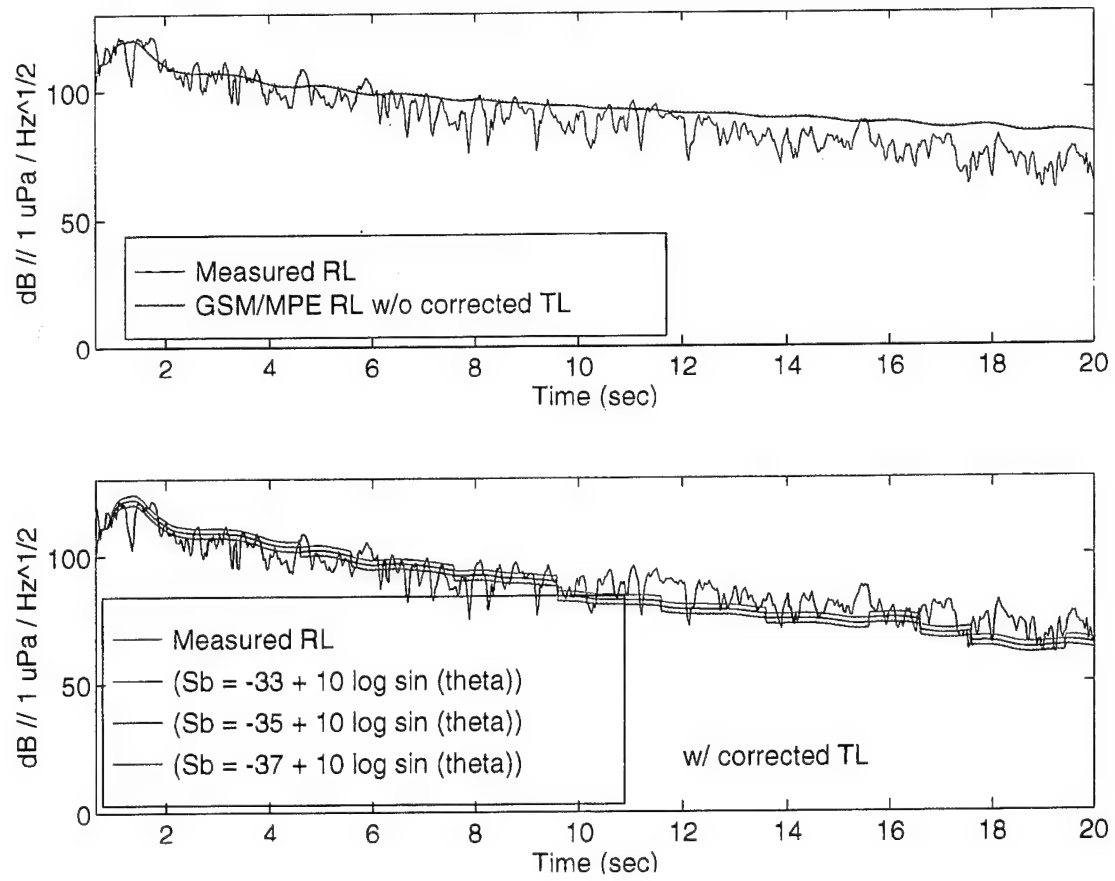


Figure 40c. Same as Figure 40a except for ping 40, beam 24.

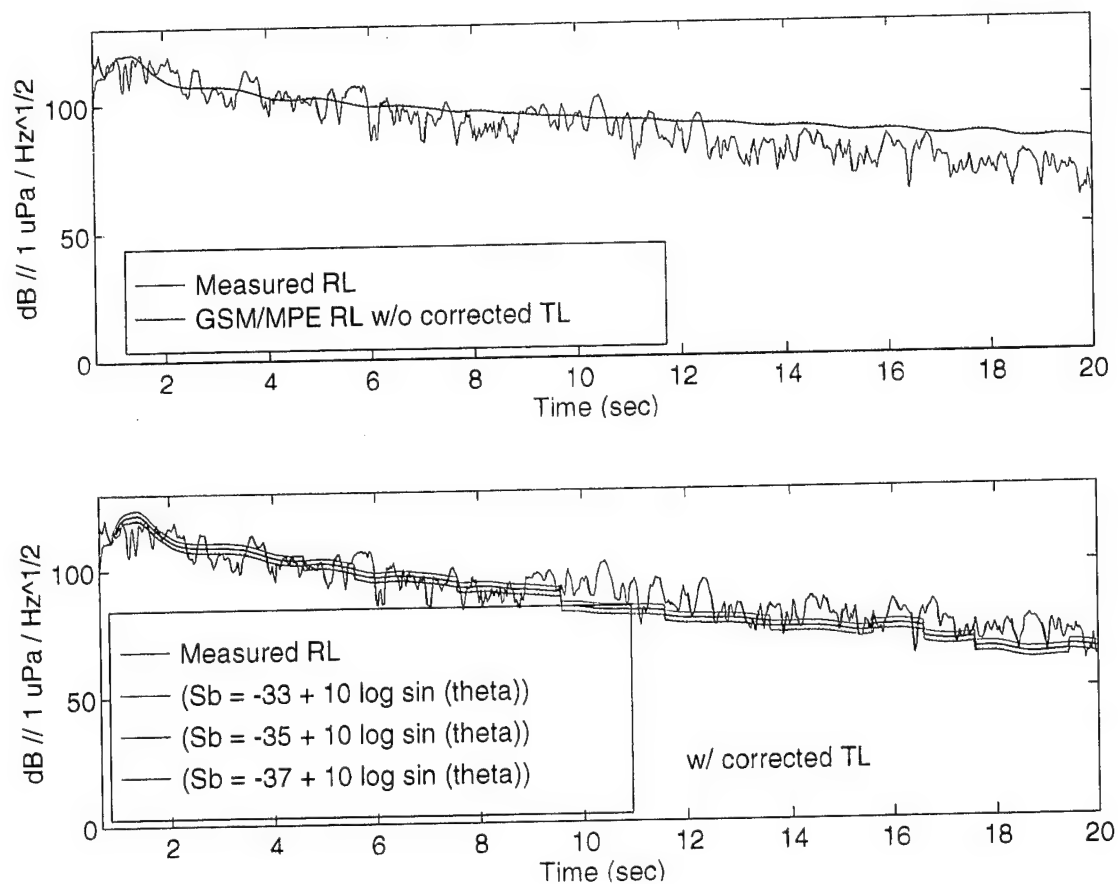


Figure 40d. Same as Figure 40a except for ping 60, beam 24.

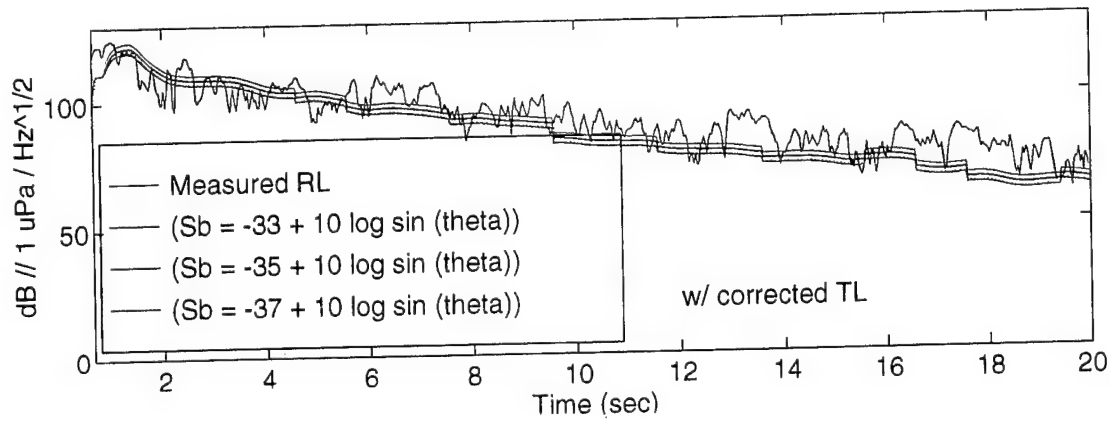
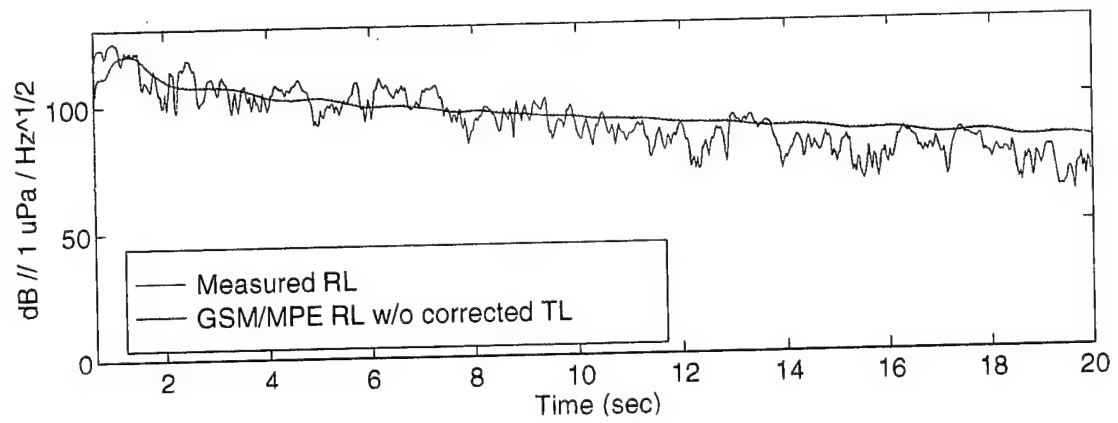


Figure 40e. Same as Figure 40a except for ping 88, beam 24.

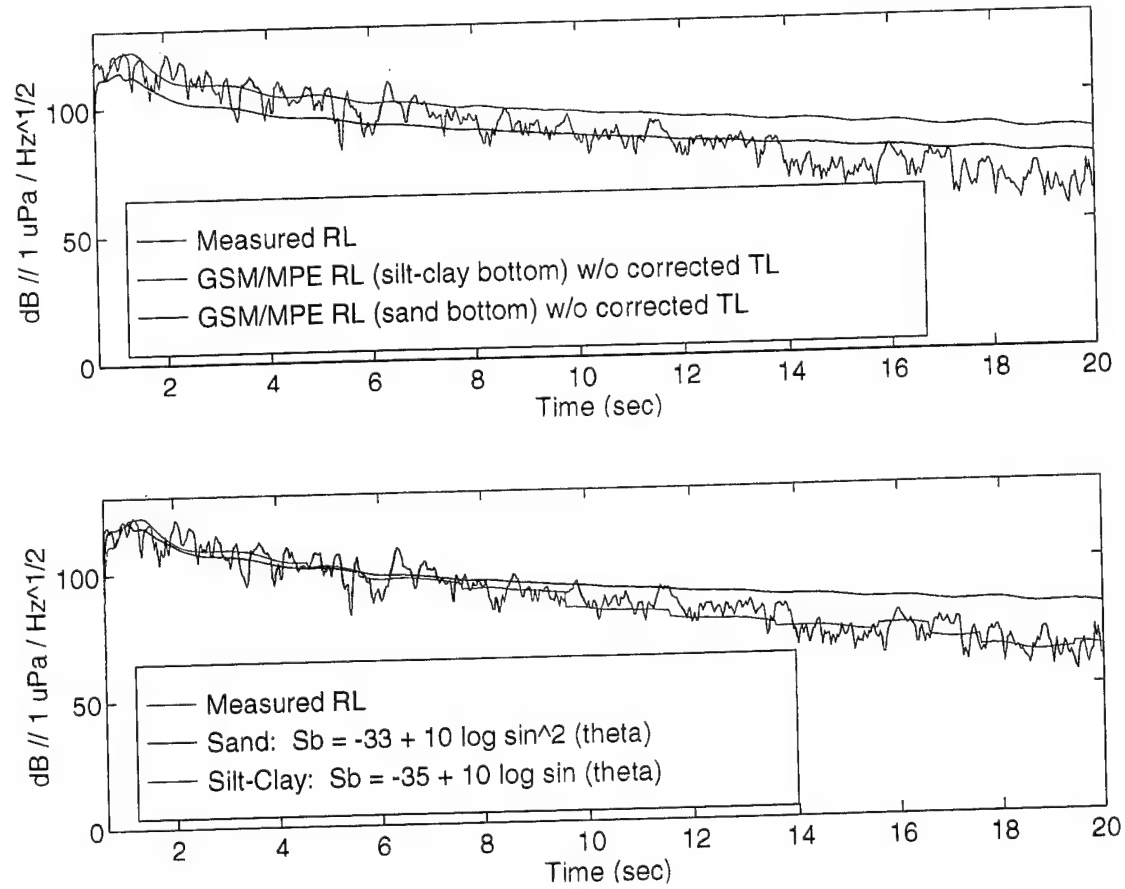


Figure 41. Comparison between the measured RL and GSM/MPE RL (without corrected TL) for ping 2, beam 1, using the NPS sand model (red curve) and NPS silt-clay model (blue curve) as input (top panel). Comparison between the measured RL and GSM/MPE RL (with corrected TL) using the NPS sand model with bottom scattering strength angular dependence of  $\sin^2(\theta)$  (red curve) and NPS silt-clay model with bottom scattering strength angular dependence of  $\sin(\theta)$  (blue curve) (bottom panel). Notice that RL for the two different bottom types with different bottom scattering angular dependencies (but similar  $10 \log \mu$ ) fit the measured RL out to about 7.5 seconds after which the curves diverge.

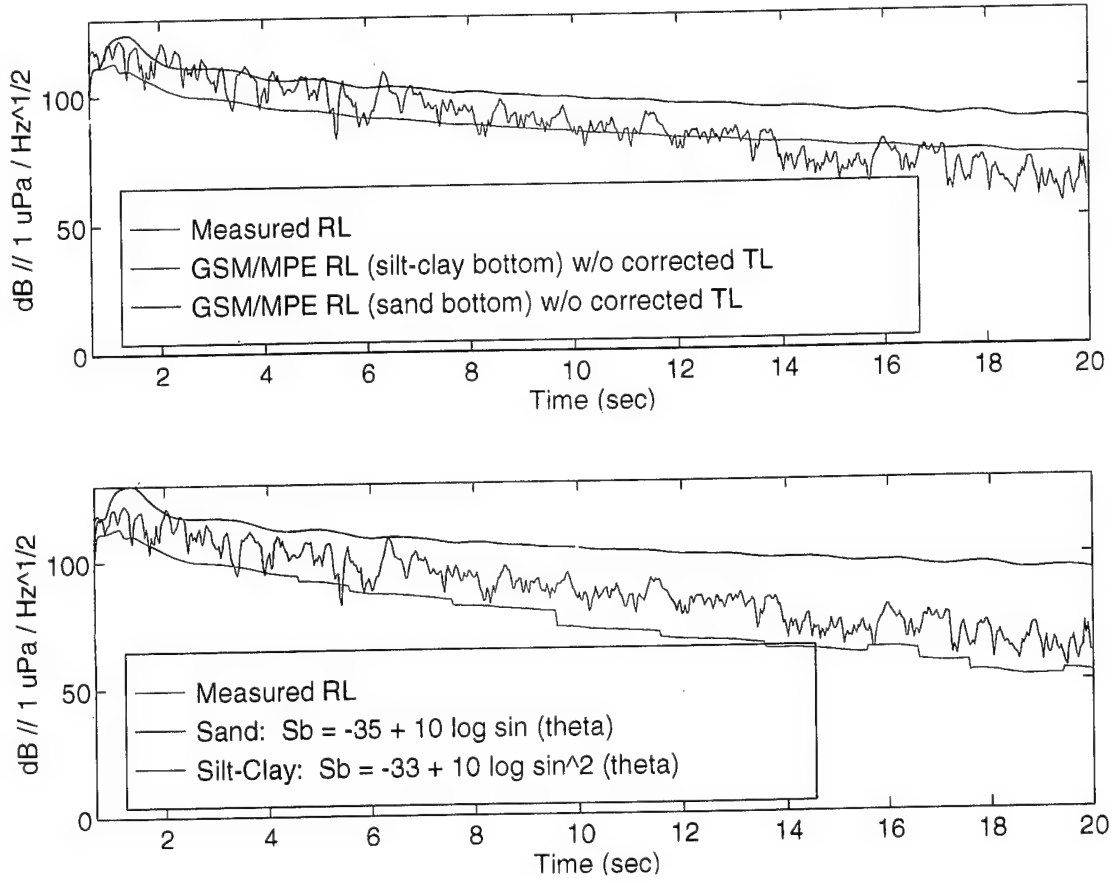


Figure 42. Same as Figure 41 except that the bottom scattering strength kernels are interchanged between the two bottom types to essentially separate the TL trend in the bottom type models from the angular dependencies. Notice now that the two modeled RLs show no similarity.

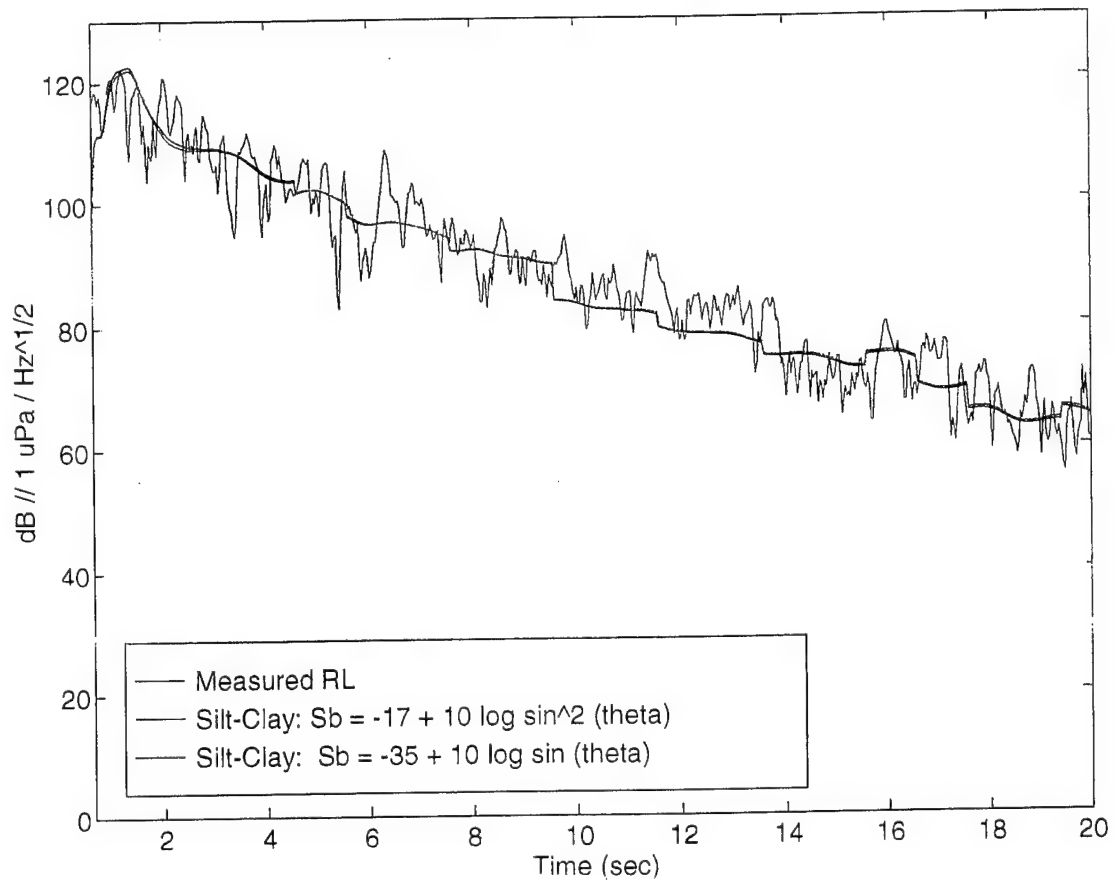


Figure 43. Measured RL (green curve) and modeled RL using the NPS silt-clay bottom as input with two different bottom scattering strength kernels;  $-17 + 10 \log \sin^2(\theta)$  (red curve) and  $-35 + \sin(\theta)$  (blue curve). Note that the two modeled RL curves are nearly coincident throughout the entire time series.

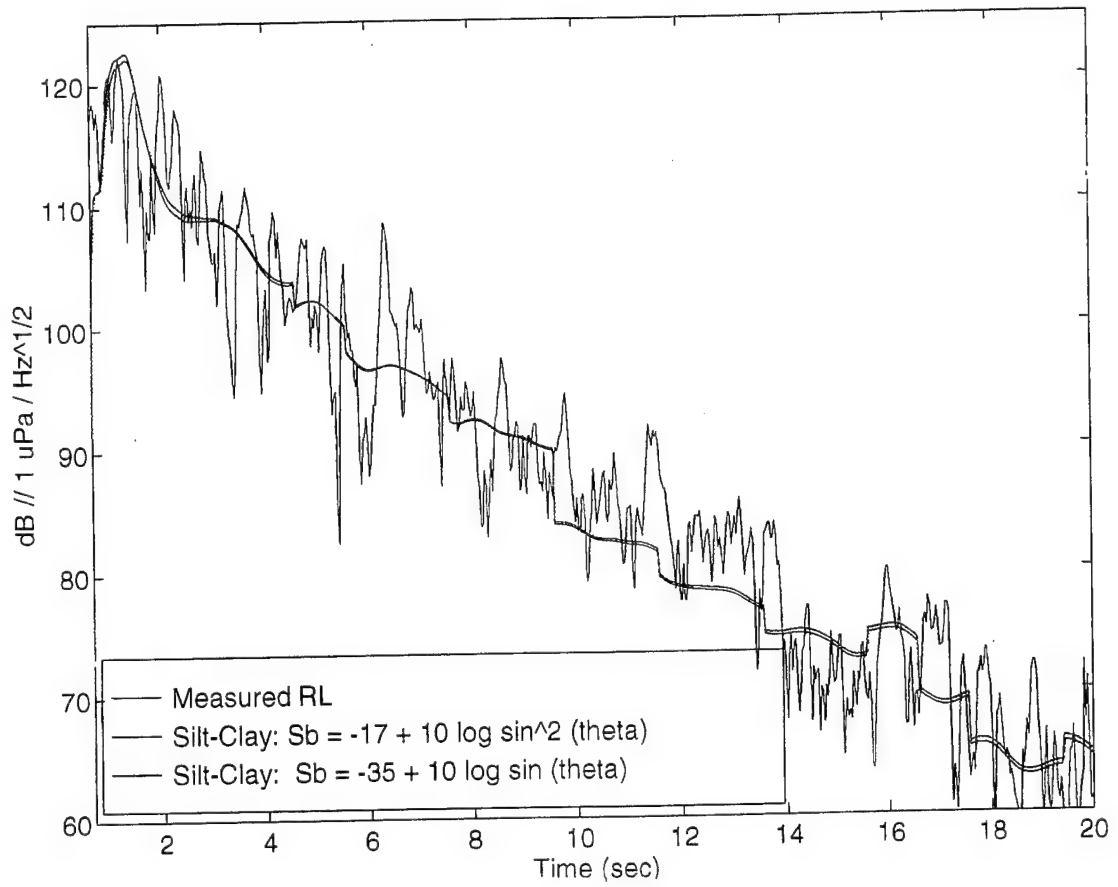


Figure 44. Expanded view of Figure 43.

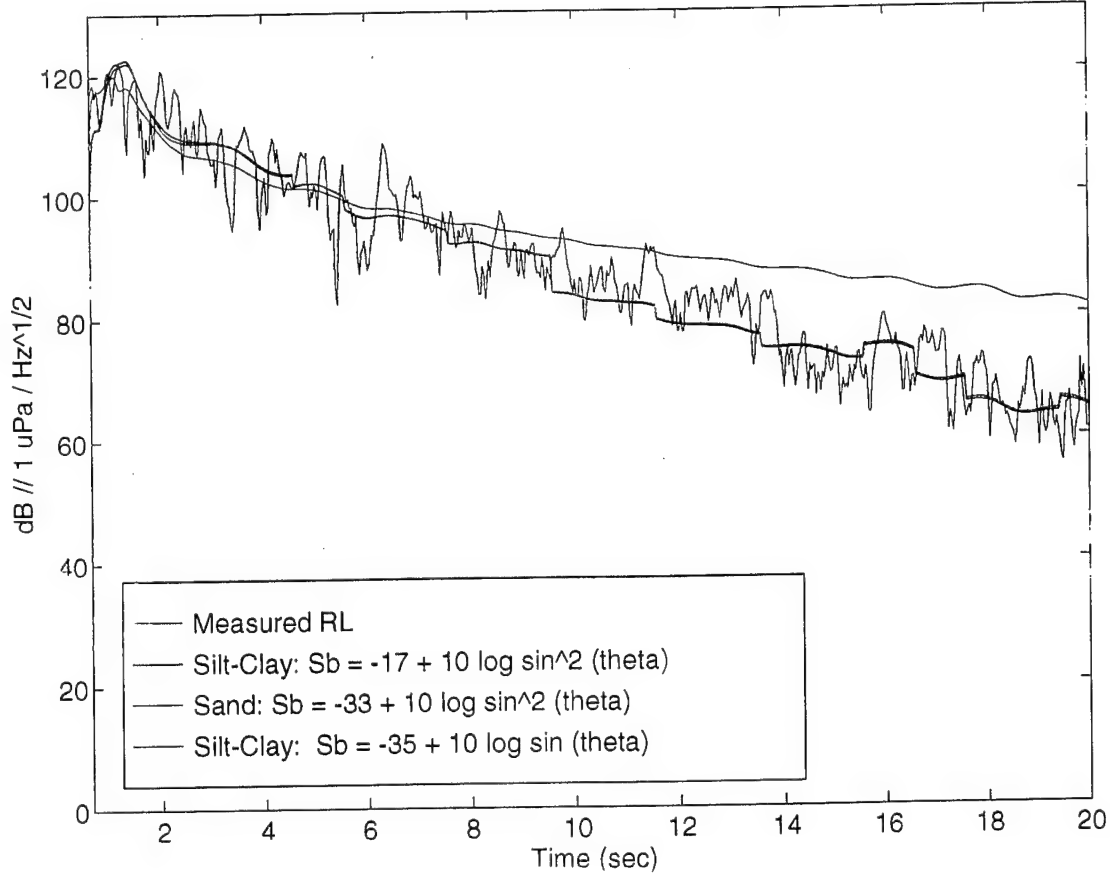


Figure 45. Same as Figure 43 except that modeled RL using the NPS sand bottom with bottom scattering kernel of  $-33 + 10 \log \sin^2(\theta)$  is included (light blue curve). This illustrates the similarity of the three modeled RLs (with different bottom scattering strength kernels) out to about 7.5 seconds.

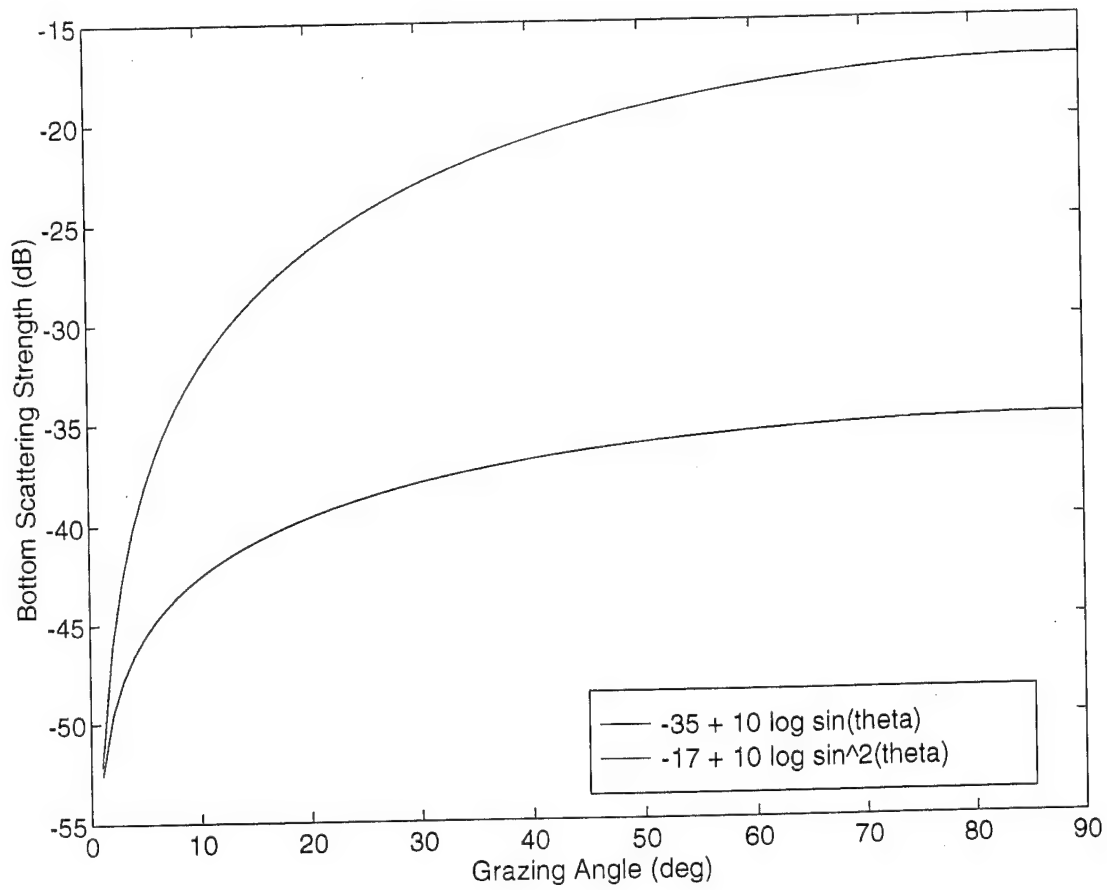


Figure 46. Bottom scattering strength as a function of grazing angle for the bottom scattering strength kernels  $-35 + 10 \log \sin(\theta)$  (red curve) and  $-17 + 10 \log \sin^2(\theta)$  (green curve). The difference between the curves is small at very low grazing angles.

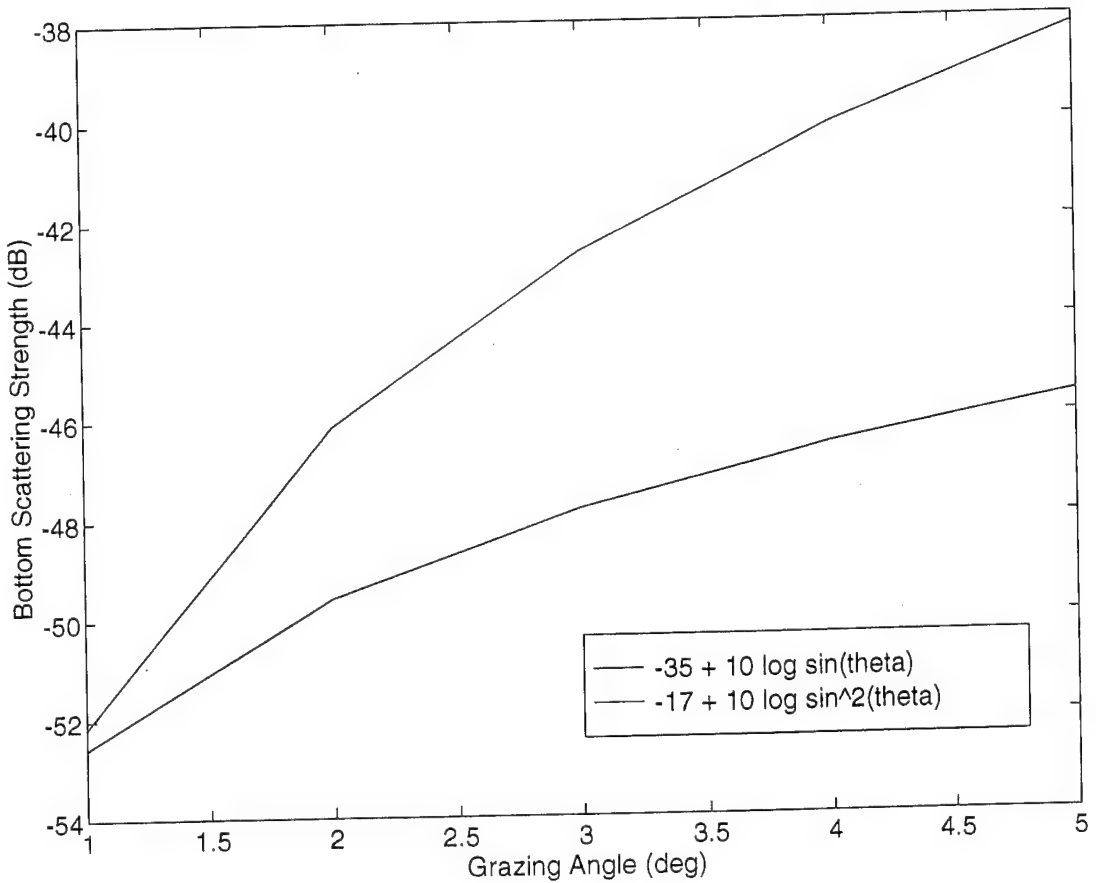


Figure 47. Same as Figure 46 but includes only grazing angles from  $1^\circ$  to  $5^\circ$ .

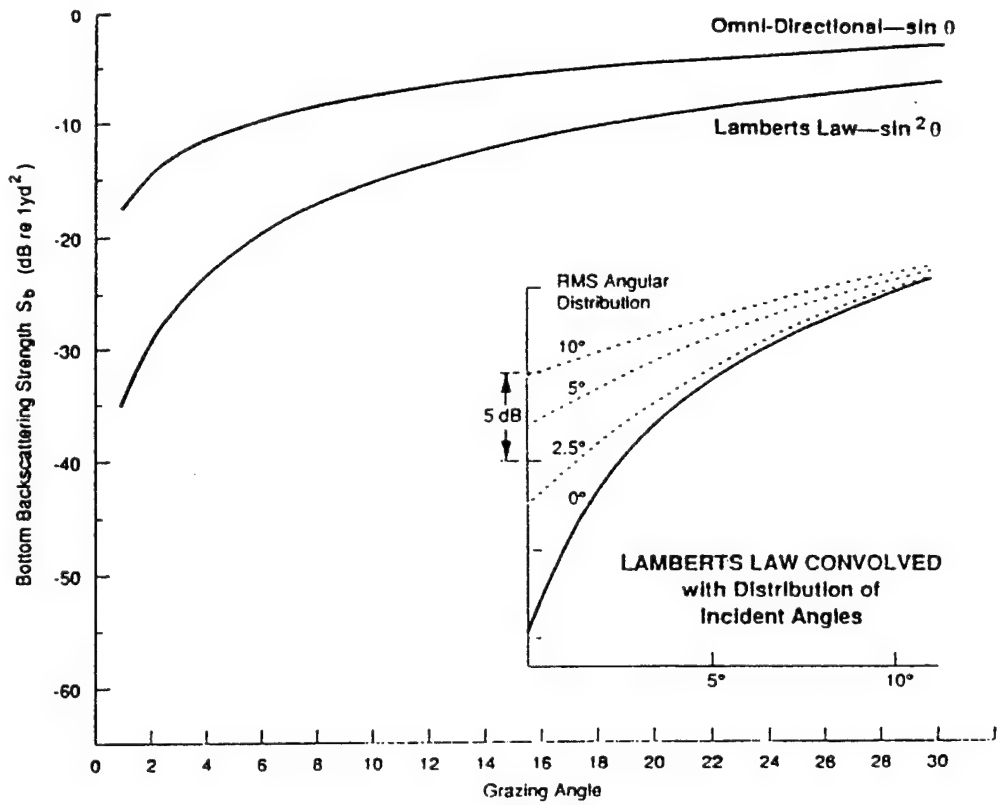


Figure 48. Bottom scattering strength as a function of grazing angle to illustrate the scattering angular dependencies,  $\sin(\theta)$  and  $\sin^2(\theta)$ . Note that the  $10 \log \mu$  term is neglected in the calculation of bottom scattering strength (from McCammon, 1993).

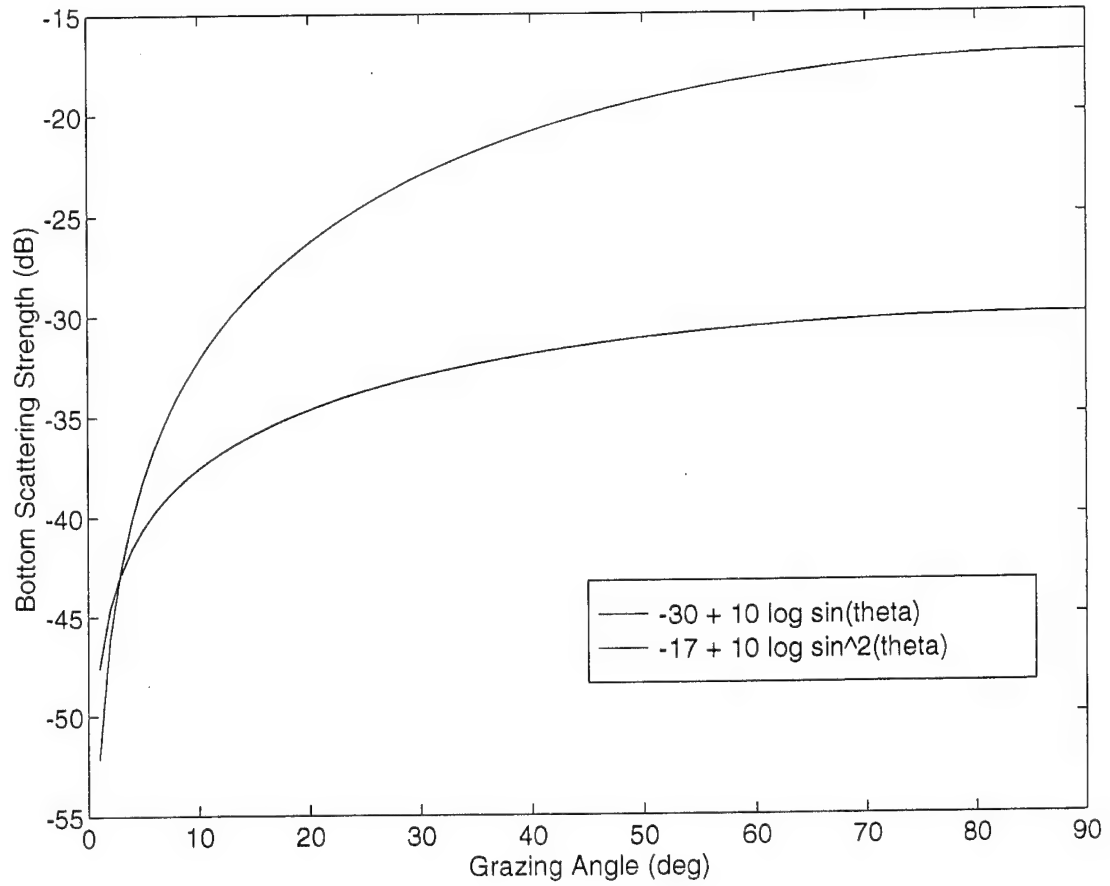


Figure 49. Bottom scattering strength as a function of grazing angle for the bottom scattering strength kernels  $-30 + 10 \log \sin(\theta)$  (red curve) and  $-17 + 10 \log \sin^2(\theta)$  (green curve). Notice that the curves show more similarity as the difference between the two  $10 \log \mu$  terms is reduced (compare to Figure 46).

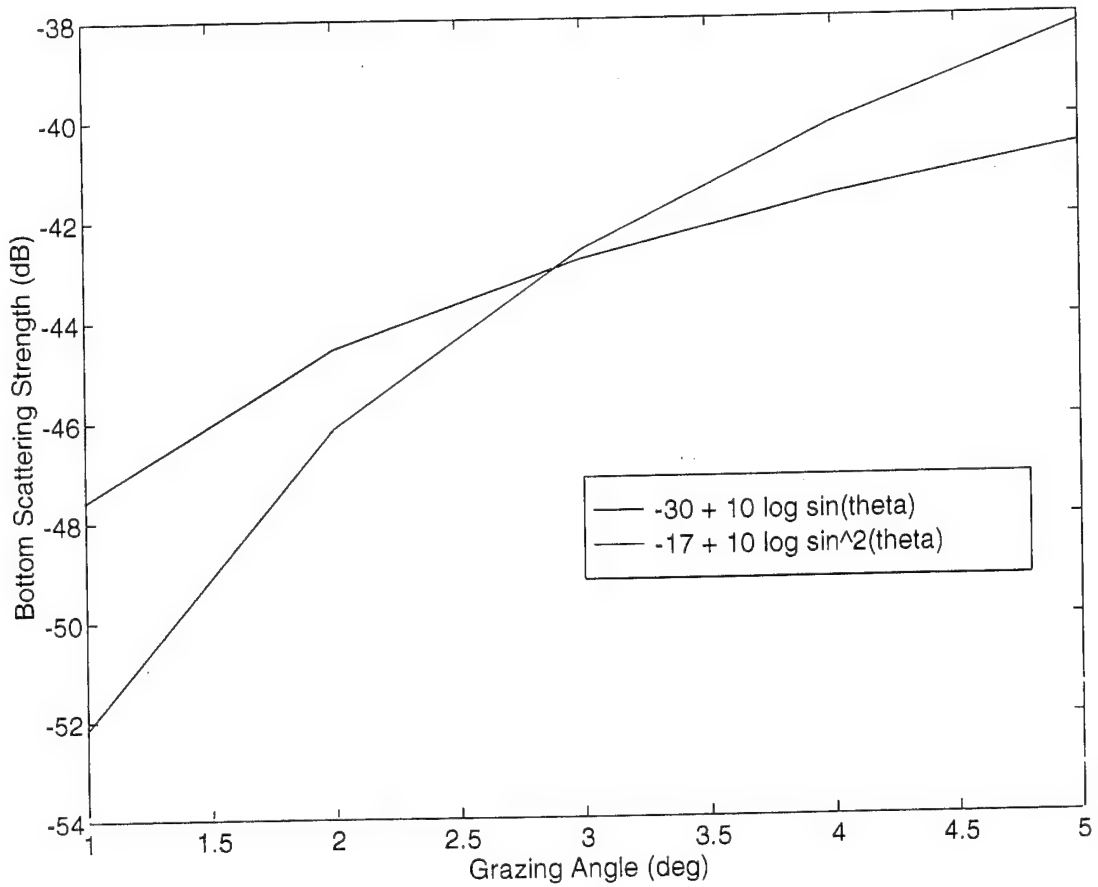


Figure 50. Same as Figure 49 but includes only grazing angles from  $1^\circ$  to  $5^\circ$ .

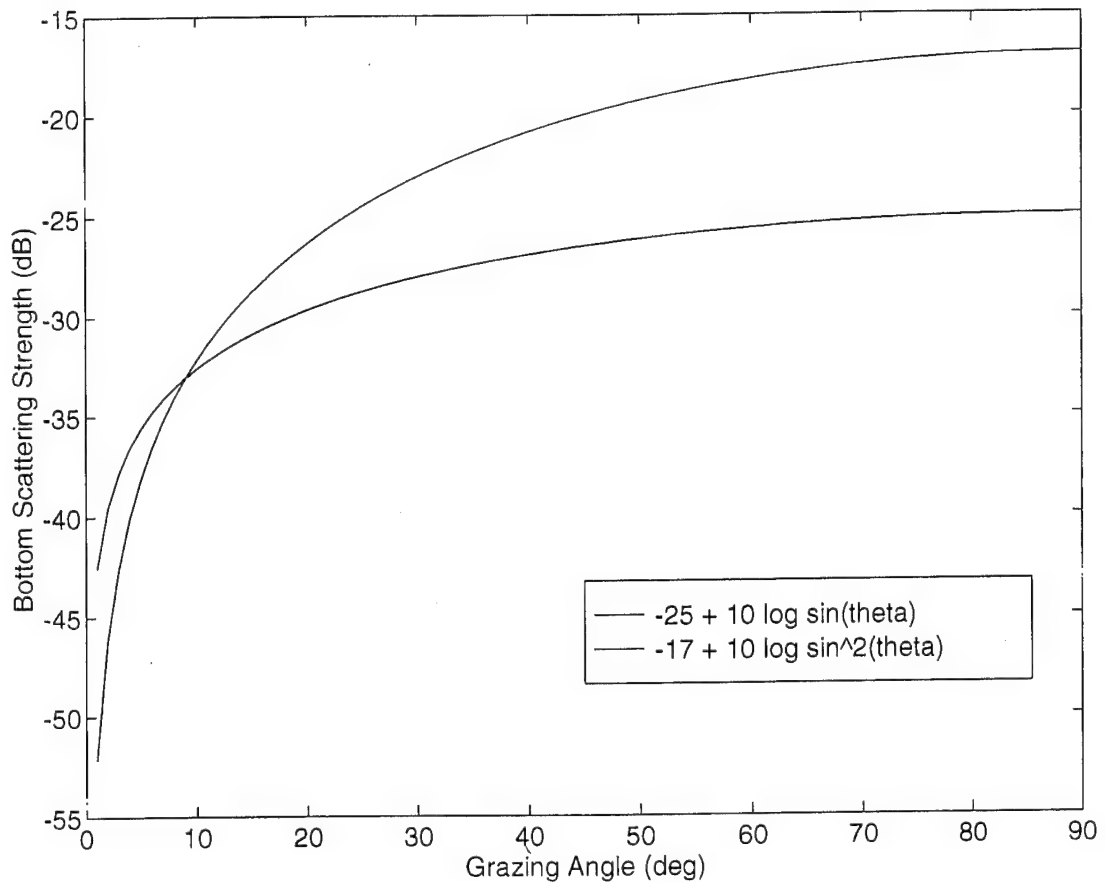


Figure 51. Bottom scattering strength as a function of grazing angle for the bottom scattering strength kernels  $-25 + 10 \log \sin(\theta)$  (red curve) and  $-17 + 10 \log \sin^2(\theta)$  (green curve). Notice that as the difference between the two  $10 \log \mu$  terms is reduced (from that in Figures 46 and 49) the bottom scattering strength curves increase in similarity and remain similar over a wider range of grazing angles.

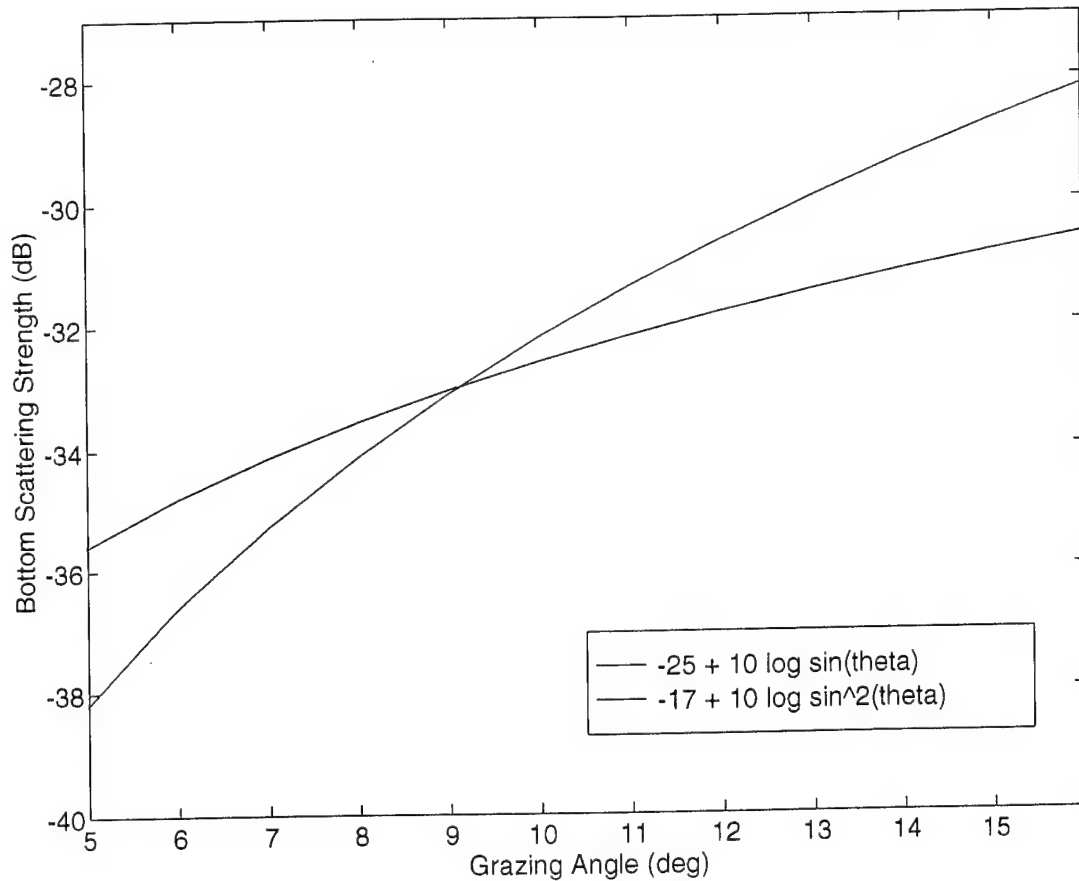


Figure 52. Same as Figure 51 but includes only grazing angles from  $5^\circ$  to  $16^\circ$ .

## REFERENCES

Bachman, R. T., Hamilton E. L., and Curray J .R. (1983). "Sediment Sound Velocities from Sonobuoys: Sunda Trench and Forearc Basins, Nicobar and Central Bengal Fans, and Andaman Sea Basins," J. Geophys. Res. **88**, 9341-9346.

Barakos, P. A. (1961). "Experimental Determination of Compressional Velocity for the Bottom Layer by Dispersion Method," J. Acoust. Soc. Am. **34**, 1919-1926.

Bishop, J. (1994). Personal Communication (Naval Undersea Warfare Center, New London, CT.).

Brocher, J., and Ewing J. (1986). "Estimation of Interval Velocities Using Seismic Refraction," J. Acoust. Soc. Am. **79**, 286-298.

Christian, R. J. and Capizzano, S. P. (1994). "Frequency and Environmental Dependence of Shallow Water Target Detections on the New England Shelf (U)," (NUWC-NWP Technical Document 10,717, New London, CT.). (**CONFIDENTIAL** Document).

Campbell, J. (1995). Personal Communication (Naval Research Laboratory, Stennis Space Center, MS.).

"PE Workshop II, Proceedings of the Second Parabolic Equation Workshop," edited by S. A. Chin-Bing, D. B. King, J. A. Davis, and R. B. Evans, NRL/BE/7181-93-0001, (Naval Research Laboratory, Stennis Space Center, MS., 1993).

Cole, B. F., Herstein P. D., and Davis, J. A. (1994). "Detection Performance Prediction of Surface Ship Tactical Sonars in Shallow Water: Area Foxtrot Baseline Study Issues and Results," (Naval Undersea Warfare Center, New London Detachment New London, CT.).

Cole, D. L. (1956). "Analysis of Bottom Sediment Data, Project Colossus," (USNUSL Technical Memorandum No. 1105-18-56, New London, CT.).

Ellis, D. D., Kampanis N. H., and Stephen, R. A. (1993). "Calculation of Ocean Bottom and Sub-Bottom Backscattering Using a Time-Domain Finite Difference Code," in *Ocean Reverberation* edited by Ellis, D. D., Preston J. R., and Urban, H. G. (Kluwer Academic Publishers, Boston, MA.), pp. 125-137.

Fisch, N. P., Bell T. G., and Hay, W. C. (1992). "Analysis of AN/SQS-53C Shallow Water Tests Conducted 3-13 September 1991 (U)," NUWC-NL Technical Report TR 10,253 (Naval Undersea Warfare Center, New London, CT.). CONFIDENTIAL.

Frisk, G. V., Doutt, J. A., and Hays, E. E. (1981). "Bottom Interaction of Low Frequency Acoustic Signals at Small Grazing Angles in the Deep Ocean," J. Acoust. Soc. Am. **69**, 84-94.

Frisk, G. V., Doutt, J. A., and Hays, E. E. (1986). "Geoacoustic Models for the Icelandic Basin," *J. Acoust. Soc. Am.* **80**, 591-600.

Gallagher, J. J. (1991). "Environmental Data Report, Shallow Water Acoustic Exercise, September 4-10, 1991," Contract No. N66604-91-D-0969, (for Naval Undersea Warfare Center, New London, CT.).

Hamilton, E. L. (1970). "Sound Velocity and Related Properties of Marine Sediments, North Pacific," *J. Geophys. Res.* **75**, 4453-4446.

Hamilton, E. L. (1971). "Elastic Properties of Marine Sediments," *J. Geophys. Res.* **76**, 579- 587.

Hamilton, E. L. (1972). "Compressional Wave Attenuation in Marine Sediments," *Geophysics*. **37**, 620-646.

Hamilton, E. L. (1976). "Sound Attenuation as a Function of Depth in the Sea Floor," *J. Acoust. Soc. Am.* **72**, 528-535.

Hamilton, E. L. (1979). "Sound Velocity Gradients in Marine Sediments," J. Acoust. Soc. Am. **65**, 909-922.

Hamilton, E. L. (1980). "Geoacoustic Modeling of the Seafloor," J. Acoust. Soc. Am. **68**, 1313-1340.

Hamilton, E. L. (1985). "Sound Velocity as a Function of Depth in Marine Sediments," J. Acoust. Soc. Am. **78**, 1348-1355.

Hamilton, E. L. (1987). "Acoustic Properties of Sediments," in *Acoustics and Ocean Bottom* edited by A. Lara-Saenz, C. Ranz-Guerra, and C. Carbo-Fite (Sociedad Espanola de Acustica Instituto de Acustica - CSIC, II F.A.S.E. Specialized Conference, Madrid, Spain), pp. 1-17.

Hamilton, E. L., Shumway, G., Menard, H. W., and Shipek, C. J. (**1956**).

"Acoustic and Other Physical Properties of Shallow Water  
Sediments off San Diego," J. Acoust. Soc. Am. **28**, 1-15.

Hamilton, E. L., Moore, D. G., Buffington, E. C., Sherrer, P. L., and  
Curry, J. R. (**1974**). "Sediment Velocities from Sonobuoys: Bay of  
Bengal, Bering Sea, Japan Sea, and North Pacific," J. Geophys Res.  
**79**, 2653-2668.

Hamilton, E. L., Bachman, R. T., Curry, J. R., and Moore, D. G. (**1977**).  
"Sediment Velocities from Sonobuoys: Bengal Fan, Sunda Trench,  
Andaman Basin, and Nicobar Fan," J. Geophys. Res. **83**, 3003-3012.

Hamilton, E. L., and Bachman, R. T. (**1982**). "Sound Velocities and  
Related Properties of Marine Sediments," J. Acoust. Soc. Am. **72**,  
1891-1904.

Hanna, J., Laney H., and Dicus, R. (1994). "System Implications of Littoral Reverberation Data," SAIC Report, Contract number N00014-92-C-0171, (for Office of Naval Research, , Washington, D.C.).

Horn, D. R., Horn, B. M., and Delach, M. N. (1968). "Correlation Between Acoustical and Other Physical Properties of Deep Sea Cores," J. Geophys. Res. 73, 1939-1957.

Houtz, R. E. (1974). "Preliminary Study of Global Sediment Sound Velocities from Sonobuoy Data," in *Physics of Sound in Marine Sediments* edited by Hampton, L. (Plenum Press, New York, NY.), pp. 519-535.

Houtz, R. E. (1977). "Sound Velocity Characteristics of Sediment from the Eastern South American Margin," Geol. Soc. Am. Bull. 88, 720-722.

Houtz, R. E. (1978). "Preliminary Sonobuoy Study of Rapidly Accumulating Shelf Sediments," J. Geophys. Res. **83**, 5397-5404.

Houtz, R. E. (1980). "Results and Methods Used to Determine the Acoustic Properties of the Southeast Asian Margins", in *Bottom-Interacting Ocean Acoustics* edited by Kuperman, W. A., and Jensen, F. B. (Plenum Press, New York, NY.) pp. 99-109.

Houtz, R. E., Ewing, J., and Le Pichon, X. (1968). "Velocity of Deep Sea Sediments from Sonobuoy Data," J. Geophys. Res. **73**, 2615-2641.

Jackson, D. R. and Briggs, K. B. (1992). "High Frequency Bottom Backscattering: Roughness versus Sediment Volume Scattering," J. Acoust. Soc. Am. **92**, 962-977.

Jacobson, R. S., Shor, G. G., Jr., and Dorman, L. M. (1981). "Linear Inversion of Body Wave Data - Part II: Attenuation Versus Depth Using Spectral Ratios," *Geophysics* **46**, 152-162.

Jacobson, R. S., Shor, G. G., Jr., and Bee, M. (1984). "A Comparison of Velocity and Attenuation Between the Nicobar and Bengal Deep Sea Fans," *J. Geophys. Res.* **89**, 6181-6196.

Jensen, E. (1995) Personal Communication (Naval Undersea Warfare Center, New London, CT.).

Mackenzie, K. V. (1961). "Bottom Reverberation for 530- and 1030-cps Sound in Deep Water," *J. Acoust. Soc. Am.* **33**, 1498-1504.

McCommon, D. F. (1993). "Low Grazing Angle Bottom Scattering Strength: Survey of Unclassified Measurements and Models and Recommendations for LFA Use," *U.S. Navy Journal of Underwater Acoustics* **43**, 33-46.

McKinney, C. M. and Anderson, C. D. (1964). "Measurements of Backscattering of Sound from the Ocean Bottom," J. Acoust. Soc. Am. **36**, 158-163.

Mitchell S. K. and Focke, K. C. (1980). "New Measurements of Compressional Wave Attenuation in Deep Ocean Sediments," J. Acoust. Soc. Am. **67**, 1582-1597.

Mitchell S. K. and Focke, K. C. (1983). "The Role of the Sea Bottom Attenuation Profile in Shallow Water Acoustic Propagation," J. Acoust. Soc. Am. **73**, 465-473.

Mourad, P. D. and Jackson, D. R. (1993). "A Model/Data Comparison for Low Frequency Bottom Backscatter," J. Acoust. Soc. Am. **94**, 344-358.

Neprochnov, Yu. P. (1971). "Seismic Studies of the Crustal Structure Beneath the Seas and Oceans," Oceanology. **11**, 709-715.

O'Keefe, S., Kelso, F. B., and Mundy, C. E. (1992). "...From the Sea," Navy and Marine Corps White Paper.

Richter, C. F. (1958). "Elementary Seismology," (W. H. Freeman and Company, San Francisco, CA.), pp. 241-245.

Scanlon, G. A. (1985). "A Study to Determine the Significance of Multiple Reflections from Embedded Thin Layers," Masters Degree Thesis, (State University of New York, Binghamton, NY.).

Schoenberger, M., and Levin, F. K. (1974). "Apparent Attenuation Due to Intra-bed Multiples," Geophysics 39, 278-291.

Schoenberger, M., and Levin, F. K. (1975). "Apparent Attenuation Due to Intra-bed Multiples II," Geophysics 43, 730-737.

Schreiber, B. C. (1968). "Sound Velocity in Deep Sea Sediments," J. Geophys Res. 73, 1259-1268.

Shoukimas, P. (1995). Personal Communication (University of Rhode Island, Providence, RI.).

Stephen, R. A. (1993). "A Numerical Scattering Chamber for Studying Reverberation in the Seafloor," in *Ocean Reverberation* edited by Ellis, D. D., Preston J. R., and Urban, H. G. (Kluwer Academic Publishers, Boston, MA.), pp. 227-232.

Stoll, R. D. (1985). "Marine Sediment Acoustics," *J. Acoust. Soc. Am.* **77**, 1785-1799.

Stoll, R. D. (1986). "Acoustic Waves in Marine Sediments," in *Ocean Seismo-Acoustics* edited by Akal, T., and Berkson, J. M. (Plenum Press, New York, NY.), pp. 417-434.

Sutton, G. H., Berckheimer, H., and Nafe, J. E. (1957). "Physical Analysis of Deep Sea Sediments," *Geophysics* **22**, 779-812.

"Test Plan for USS STUMP (DD-978) for FY-91 and FY-92," (1991).  
(NUSC Publication, New London, CT.).

"The Physics of Sound in the Sea," (1946). Part 2, *Reverberation*,  
Summary Technical Report of Div. 6, NDRC, vol. 8, (National Defense  
Research Committee, Washington, D.C.), pp. 247-342.

Urick, J. (1983). "Principles of Underwater Sound," 3rd ed., (McGraw  
Hill Inc., New York, NY.), 237-285.

Wong, H. K., and Chesterman, W. D. (1968). "Bottom Backscattering  
Near Grazing Incidence in Shallow Water," J. Acoust. Soc. Am. 44,  
1713-1718.

Weinberg, H. (1985). "Generic Sonar Model," Naval Underwater  
Systems Command Technical Document 5971D (Newport, RI.,1985).

Weinberg, H. (1995). Personal Communication (Naval Undersea Warfare Center, New London, CT.).

## **INITIAL DISTRIBUTION LIST**

	<u>No. Copies</u>
1. Defense Technical Information Center Cameron Station Alexandria, VA 22304-6145	2
2. Library, Code 52 Naval Postgraduate School Monterey, CA 93943-5101	2
3. Chairman (Code OC/BF) Department of Oceanography Naval Postgraduate School Monterey, CA 93943-5100	3
4. Naval Meteorology and Oceanographic Command 1020 Balch Boulevard Stennis Space Center, MS 39529-5005 Attn: RADM P. G. Gaffney C. Wilcox	2
5. Commanding Officer Naval Oceanographic Office Stennis Space Center, MS 39529-5001 Attn: Dr. Landry Bernard Dr. Martha Head Library	3

6.	Commanding Officer Naval Research Laboratory Code 5100/5123 Washington, D. C. 20375-5000 Attn: Dr. T. C. Yang	4
7.	Officer in Charge Naval Research Laboratory Stennis Space Center, MS 39529-5004 Attn: Dr. P. Bucca Dr. S. Chin-Bing Dr. D. King Mr. J. McDermid	4
8.	Commanding Officer NCCOSC RDTE DIV 53560 Hull St. San Diego, CA 92152-5100 Attn: Capt. K. E. Evans Dr. J. Roesel Dr. H. Bucker Dr. F. Ryan Dr. R. Bachman	5
9.	Dr. James H. Wilson Neptune Sciences, Inc. 3834 Vista Azul San Clemente, CA 92674	6

10. Mr. Barry Blumenthal 1  
Code C124A  
Advanced Environmental Acoustic Support Program  
Office of Naval Research  
800 N. Quincy St.  
Arlington, VA 22217-5660

11. ARPA/MSTO 2  
3701 N. Fairfax Dr.  
Arlington, VA 22203-1714  
Attn: Capt. Lowell  
Dr. T. Kodij

12. Mr. Ed Chaika / Mr. Dave Small 2  
Advanced Environmental Acoustic Support Program  
Code ONR - DET  
Building 1020 - Rm. 184  
Stennis Space Center, MS 39529-5000

13. Mr. John G. Schuster 1  
Technical Director  
Submarine and SSBN Security Programs  
N87/OP-02T  
Office of the Chief of Naval Operations  
Washington, D. C. 20530

14. Cdr. Mark Klett 1  
Code N30A  
Surface Warfare Development Group  
Little Creek Amphibious Base  
Norfolk, VA 23521

15. Mr. Ed. Jensen / Mr. Al Goodman Naval Undersea Warfare Center Det., New London 39 Smith Street New London, CT. 06320-5594	2
16. Capt. G. Nifontoff / Cdr. S. Scrobo Program Executive Office Surface Ship ASW Systems Washington, D. C. 20362-5104	2
17. LT. Gary A. Scanlon PSC 821 Box 84 FPO AE 09421	2